UNIVERSITY OF TRENTO

Smart Energy Systems: using IoT Embedded Architectures for Implementing a Computationally Efficient Synchrophasor Estimator

---

Author:
Pietro TOSATO

Advisors:
Dr. Davide BRUNELLI
Dr. David MACII

A thesis submitted in fulfillment of the requirements for the PhD degree

at the

Doctoral School in Materials, Mechatronics and Systems Engineering
Department of Industrial Engineering

April 12, 2019

Acknowledgements

Few but sincere words to whom help and support me during this journey of (more than) three years. My heartfelt gratitude and esteem to Davide Brunelli and David Macii, two great advisors and teachers during this period: thanks for the huge support during this adventure!
Thanks to my friends and colleagues in Trento, the ones in laboratory and all whom I had the chance to talk with and learn something new, in particular to Maurizio and Matteo.
A special mention goes to the friendly colleagues I met during my stay in Belfast, starting from David, John, Paul and Judith.

Thanks to the dear Valentina, Elena, Andrea, Stefano, Luca and Sofia for distracting me from this cruel world.

Thanks to Giulia who supports my period abroad from the distance, and keep supporting me, ironically still from some hundreds kilometers: I feel very lucky to have someone like you trusting, supporting and bearing me, I love you.

Last, but not least, a sincere thank to my parents and my family for incessantly bearing me.

I'm forgetful, please don't mind if I didn't mention you.

Contents

List of Figures

List of Tables

List of Abbreviations

ADC	**A**nalog to **D**igital **C**onverter
BBB	**B**eagle**B**one **Black**
DER	**D**istributed **E**nergy **R**esource
DFT	**D**iscrete **F**ourier **T**ransform
DSP	**D**igital **S**ignal **P**rocessor
DSO	**D**istribution **S**ystem **O**perator
FE	**F**requency **E**rror
FIR	**F**inite **I**mpulse **R**esponse
GPS	**G**lobal **P**ositioning **S**ystem
IoT	**I**nternet **o**f **T**hings
IRIG-B	**I**nter-**R**ange **I**nstrumentation **G**roup - format **B**
PDC	**P**hasor **D**ata **C**oncentrator
PMU	**P**hasor **M**easurement **U**nit
PPS	**P**ulse **p**er **S**econd
PRU	**P**rogrammable **R**eal-time **U**nit
PSD	**P**ower **S**pectral **D**ensity
ROCOF	**R**ate **O**f **C**hange **O**f **F**requency
RFE	**R**ate of change of **F**requency **E**rror
RMS	**R**oot **M**ean **S**quared
SC	**S**ervo **C**lock
SFDR	**S**purious-**F**ree **D**ynamic **R**ange
SINAD	**S**ignal-to-**N**oise **a**nd **D**istortion
SNR	**S**ignal-to-**N**oise **R**atio
THD	**T**otal **H**armonic **D**istortion
TVE	**T**otal **V**ector **E**rror
UTC	**C**oordinated **U**niversal **T**ime
WAMS	**W**ide-**A**rea **M**anagement **S**ystem
WLS	**W**eighted **L**east **S**quares
XO	Crystal **O**scillator

Introduction

Motivations of the thesis

Energy efficiency is a key challenge to build a sustainable society. It can be declined in variety of ways: for instance, from the reduction of the environmental impact of appliances manufacturing, to the implementation of low-energy communication networks, or the management of the existing infrastructures in a smarter way. The actual direction is the integration of different energy systems with a common management scheme with the aim of harmonizing and integrating different energy systems.
In this context, smart cities already envision the use of information communication technologies (ICT) to smartify objects and services, connecting people and machines. An important enabling technology for smart cities is certainly the Internet of Things (IoT).
Both smart cities and IoT have been extensively investigated over the last few years, under the influence of European funded projects as well. Smart cities apply communication and networking technologies, very often using the paradigm of IoT, to address relevant issues like traffic congestion, population growth, crowding, and others, besides implementing innovative services, modernizing existing infrastructures, e.g. smart mobility. IoT greatly helps in monitoring and better managing energy consumption as well, realizing smart homes, smart buildings and smart grids. For what concern the power grid, in fact, the direction is to harness IoT technologies to improve flexibility, easiness of use and, ultimately, energy efficiency while preserving stability and safety. Today the electrical grid is facing deep changes, mostly caused by the intensive deployment of Distributed Energy Resources (DER) based on renewable sources such as photovoltaic plants or wind farms. Managing such heterogeneous active distribution networks (ADNs), represent one of the most important challenges to be faced in the future of energy systems. The integration of active elements into the grid is challenging because of both the great potential they

bring in energy production and the hazard they may represent if not properly managed (e.g. violation of operational constraints). ADN implementation relies on the deployment of high-performance real-time monitoring and control systems.

It is well accepted that the phasor measurement units (PMU) are one of the most promising instruments to overcome many problems in ADN management, as they support a number of applications, such as grid state estimation, topology detection, volt-var optimization and reverse power flow management. However, classic PMUs are conceived to measure synchrophasor in transmission systems, while the distribution ones have very different characteristics and, in general, different needs. Therefore, tailoring the characteristics of the new-generation PMUs to the needs of the ADNs is currently very important. This new kind of PMU must address few important design challenges:

1. improved angle measurement capabilities, to cope with the smaller angle differences that distribution grids exhibit;
2. low cost, to promote an extensive deployment in the grid.

These two requirements are clearly in opposition.

In this dissertation, a low-cost PMU design approach, partially influenced by IoT ideas, is presented.
In particular, this thesis is organized as follow.

Organization of the thesis

In Chapter 1, an overview of some projects that focus on IoT are reported as examples of the way to improve energy efficiency in smart city applications. This chapter is dedicated to the presentation of some research outputs achieved in the first year of the PhD course. This chapter is not strictly related with smart grid measurements, but deals with energy systems from a broader perspective. After an introduction to smart cities, the discussion is focused on low-power electronics. The concept of IoT is presented along with the many enabling technologies and benefits. A couple of design examples are then proposed. Both of them deal with energy harvesting and low-energy management, resulting in successful implementations of a pollution monitoring system and a proof-of-concept wake-up radio for smart sensor nodes. The purpose of such systems is proving the benefits that an energy aware approach can yield to apparently simple monitoring applications. Another example in this chapter deals with a prototype of wake-up receiver operating with power line communication technology and designed for street lighting

network application. A section on the power grid needs and the future smart grid concludes the chapter.

In Chapter 2, the basics of synchrophasor measurement are introduced. The definition, nomenclature and models for synchrophasor measurements are given. Then, the standards for PMU compliance testing are presented.

To better understand how a PMU works and what the main uncertainties contributions affecting the synchrophasor measurement are, a PMU testbed is described in Chapter 3. The characterization of such a system based on a noise propagation model helps the developer to understand the impact of different uncertainty contributions.

Chapter 4 deals with a novel algorithm conceived for a low-cost PMU based on performance-constrained embedded platforms. The analysis of the performance of the algorithm is split between Chapter 4, where the metrological performance are analyzed, and Chapter 5, where the trade-offs needed to ensure real-time performances are discussed.

In particular, after a description of a low-cost PMU implementation, the evaluation of timing performance of the proposed algorithm is presented in Chapter 5, along with relevant details on synchronization and syntonization for data acquisition. A servo clock for PMU synchronization is implemented and characterized for this purpose.

Chapter 6 concludes the thesis with a summary, some final remarks and future work.

Contributions of the thesis

This dissertation contributes to the implementation of modern smart energy system, inspired by state of the art IoT solutions to reduce power consumption while improving services and operations. This is declined in a couple of different ways: energy efficient IoT solutions and a low-cost yet effective implementation of PMU to modernize ADNs.

A smart IoT enabling energy efficiency Energy efficiency is needed for IoT applications and, in turn, smart IoT applications enable energy savings. Some ideas from the world of IoT can be applied to smart grids as well. For instance, a smart lighting solution based on a prototype of a wake-up receiver to turn on different nodes of the system only when needed is presented. This approach enables to save standby power consumption, while keeping the same functionality of the network. The

idea comes from the wireless counterpart, i.e. wake-up radios, which are presented in this dissertation as well.

A low-cost PMU implementation A PMU running on a low-cost platform is envisioned. To this goal, an algorithm for synchrophasor, fundamental frequency, and rate of change of frequency estimation is developed for processing platforms with limited computational resources .
The proposed solution harnesses the main advantages of two state-of-the-art algorithms, namely the Interpolated Discrete Fourier Transform (IpDFT) and the Taylor Fourier Transform (TFT). A new algorithm is proposed and implemented in a computationally efficient manner to reduce processing time as much as possible. To this aim, the number of harmonics accounted in the model is changed adaptively to minimize the computational burden while meeting the main requirements specified in the IEEE standards C37.118.1 and the Amendment C37.118.1a. The resulting processing time of the algorithm is compliant with the mandatory reporting periods of M class or P class PMU. Estimation accuracy has been evaluated not only through simulations but also experimentally.

A servo-clock (SC) for PMUs is also proposed. The SC relies on a classic proportional integral controller, which has been properly tuned to minimize the steady-state short-term time synchronization uncertainty. The SC has been implemented and tested on a PMU prototype developed within the OpenPMU project. The distinctive feature of the proposed solution is its ability to track an input Pulse-Per-Second reference with good stability and with no need for specific on-board synchronization circuitry. Indeed, the SC implementation relies only on only one co-processor of the chosen platform.

A testbed for PMU algorithms While algorithms for synchrophasor estimation are usually benchmarked by simulations, the overall PMU accuracy depends on measurement hardware as well (e.g., transducers, data converters, and synchronization circuitry). However, the impact of the related uncertainty contributions on PMU metrological parameters is very difficult to predict or to simulate, resulting in possible mismatches between simulation and experimental results. A testbed was specifically developed in cooperation with the University of Campania *"L. Vanvitelli"* to evaluate and compare algorithms accuracy under the same experimental conditions. A thorough metrological characterization of the testbed, properly supported by a noise propagation model, is performed in order to quantify uncertainty contributions of the different hardware and software components and how much they impact on the estimates of synchrophasor magnitude, phase, frequency and rate of change of frequency returned by different algorithms under test.

CHAPTER 1

Energy Efficiency in Smart Cities

In this chapter, a broad vision of energy efficiency enablers for smart cities is given. The various and rather heterogeneous sections deal with different examples of low-power technologies. The discussion, however, follows a specific plot, describing technology and relative applications in different fields. In particular, the following sections present IoT technologies with few design examples, including smart lighting. Finally, the power system research trends are introduced.

1.1 Introduction

While the world population breaches the 7 billions threshold, mostly agglomerated in metropolitan areas, several problems still require smart solutions, for instance in transportation, environment and quality of life, among others.
European Union, is active and sensitive in this context, promoting plans and action to reduce energy consumption and all the wastes which, in general, cause high pollution levels. *Horizon 2020* is one of the biggest research funding program ever, which *"help to achieve smart, sustainable and inclusive growth"*. Till 2020, European Union agenda is clear in fixing three targets regarding energy: *(i)* $-20\,\%$ greenhouse gas (GHG) emission (with respect to 1990), *(ii)* $20\,\%$ share of energy coming from renewable sources and *(iii)* $+20\,\%$ in energy efficiency [1]. These goals, even if seem ambitious, are likely to be achieved. For 2030, EU has reinforced this message with new targets, like the $27\,\%$ share of energy that comes from renewable sources [2].

Energy efficiency is the key binomial to overcome most of the technological problems of the century. Starting from buildings to microelectronic, from production

processes to networking, energy efficiency is always a need, as energy is becoming more and more valuable, even if people tend to forget it. After a long period of wastes, in the era of smart cities, the energy systems also have to become smarter, to solve, at least partially, some environmental problems.

The smart city buzzword is around from few years now, and many definitions were formulated, all of them relying on the same concept of making better use of resources increasing quality of services by exploiting Information Communication Technologies (ICT) [3]. Because of its broad scope, smart city embrace many research fields, not only ICT-related. This synergy often permits to obtain valuable results from many perspectives. In fact, the concept of smart energy systems, also relies on the joint effort coming from different domains (e.g. thermal, electrical and gas grids combined) to create a sustainable and affordable energy future [4].
Both academia and industry are now focusing on developing strategies for implementing the smart city. For instance, IEEE has promoted the Smart City Community, to raise awareness around topics like smart living, sustainable energy management and smart mobility, and the Smart Cities Initiative to facilitate and boost collaborative work between different societies like Communication Society, Power & Energy Society, and others. Large companies like IBM, CISCO and Intel are involved in various projects for smart city creation.
Some smart cities around the world are already recognized, and already have implemented smart systems to handle *(i)* power grid, *(ii)* buildings and *(iii)* lighting [5], [6]. On these three domains in particular, the aim is not only the improvement of the quality of the system, making it smarter, but also facing major problems like environmental pollution, the scarcity of natural resources or climate changes. The reduction of greenhouse gases is also a great challenge for the XXI century, addressable only with enhanced smart energy systems.

Energizing the city Including the current concept of smart grid into the big smart city container is not fully rightful. However, electricity transmission and distribution have a clear impact on everyday life, which is expected to be even more important in the future due to the penetration of electrical mobility. More in general, smart city solutions must be energy efficient and tackle the associated challenges. It would be shortsighted to exclude the grid energy efficiency from the broad vision of a smart city. Currently, citizens have also become more aware about energy use and waste, especially as far as electricity is concerned. The border sometimes is also not clearly visible even in literature contributions: the term *smart energy system* in fact is used as a synonym of *smart grid* by some authors [4].
With respect to smart grid, it is undoubted the importance of integrating renewable energy resources. Distributed generation and management are under the lens

of many researchers and are currently envisioned as a key for future electricity systems (in addition to energy storage and demand response) [7].

Of course, energy efficiency should be primarily achieved by reducing the power consumptions of buildings. In fact, they consume the biggest share of primary energy, more than any other sector (for instance, approximately 40 % in heating, air conditioning and lighting) [8].

To cope with this and many other energy challenges, ICT can provide a great help.

Networking the city Internet offers sophisticated and ubiquitous networking for smart city services. The buzzword today is *Internet of Things*, the communication paradigm that envision objects of everyday life equipped with connectivity and the possibility to communicate to each other and to the user, becoming part of the Internet [9]. In turn, Internet will become even more pervasive than it is today. This is a key to *"smartify"* the existent smart city component systems or building the new generation ones, especially buildings, energy grids and lighting systems. As previously stated, energy efficiency is the challenge to address in order to implement successful services without impact on the environment. Of course, IoT devices also have to be efficient and consume as less power as possible, avoiding energy overheads and achieving a seamless integration of the ICT infrastructure [10].

1.2 The role of IoT

Human being is building an intricate and huge network, pervading all the aspects of his society and every angle of a city. Internet of Things (IoT) is an important and growing part of this complicate network and represents the new paradigm in networking smart things, connecting thousands of objects and devices to the biggest network ever created by humanity. IoT offers advanced connectivity to implement smart services on objects and applications in various fields, such as Smart Cities, buildings, logistics, Smart Grid, domotic and industrial applications, agriculture, air quality monitoring and many others.
The idea of interconnecting things and object providing Internet connectivity is not brand new. In fact, the IoT buzzword has been used since the early 2000s [11]. However, only nowadays we are facing a rapid growth of this market, because of the many technological advances that enable the rise of IoT and a common feeling that IoT itself represents a big opportunity to improve products and implement services.

As many IoT nodes are battery powered, the key requirement for a successful implementation of IoT devices is the availability of low-power electronics which provide sensing and sometimes actuation. Speaking of energy management in IoT, two are the keys to increment the battery life of a device: energy efficiency and energy harvesting [10]. The first includes techniques to improve the energetic behavior of the system, for instance with lightweight protocols or scheduling optimization, while the latter refers to the possibility of collecting energy from the environment. Hence, it is possible to exploit very low energy amounts with a careful and energy efficient design.

The way an IoT device connects to the Internet is quite important. Very often this is achieved by means of wireless communication technologies, that perhaps put IoT near Wireless Sensor Network (WSN) solutions. The two terms obviously refer to different concept: IoT has a broader scope, sometimes including actuation. However, they share common challenges. As in WSNs, IoT nodes can be deployed in a large number and then dispersed in the environment they have to sense, therefore the low-cost and long-life characteristics of the node are important. The lifetime of the resulting node is usually bounded by the energy demand characteristics of the electronics and, in turn, by the wireless communication subsystems, which (very often) is a requirement for IoT also. Broadly speaking, WSN can be seen as a part of IoT [12].

Some of the enabling technologies for IoT includes Bluetooth Low energy (BLE), near-field communication (NFC) and quick response codes (QR) [11], but the number of acronyms identifying different technologies, protocols and devices is huge.

1.2.1 Enabling technologies

The wireless subsystem optimization, is one of the key for IoT development, and one of the most promising trend nowadays is the adoption of low-power and long-range wireless technologies to implement low-power wide area (LPWA) networks. Some technologies were already investigated in literature, as LoRa and NB-IoT. Both have the peculiarity of a very high link budget, over 150 dB, and quite low data rates which are compatible with the low bandwidth required by a typical IoT application. The size of a packet is also low, with a quite high latency, making it unsuitable for strict real-time monitoring requirements. On the other side, their great advantage (of LoRa in particular) is power efficiency [13], [14]. Other relevant parameters include the low development costs of a LoRa network (compared with

other LPWA network technologies), the good coverage (i.e. high sensitivity) and good scalability of the network [15].

Although the use of efficient long-range communication technologies helps (exploiting their usually high link budgets), this is not the only way to reduce power consumption of an IoT application [16]. For instance, low power operation can be supported by duty-cycling, e.g. turning off power hungry components when not used, and more in general, by a smart scheduling optimization. The radio transceiver is the first component to shut down. Modern microcontrollers have low-power states which allow to greatly reduce power consumption and eventually implement a transiently powered device [17].
In the current Low-Energy Internet of Things (LE-IoT), the nodes are simple, they often only sense environment and complex processes are actually deployed out of the node, e.g. on the gateway or *in the cloud*. This paradigm is actually changing towards a more distributed approach, where each node participate in active way to process data and even to put *intelligence on the edge*, meaning that each node can be equipped with its own processing module, even for machine learning or other complex operations [18], [19].

Of course a key requirement to successfully implement IoT is low-cost of device components. Thus, excessive hardware complexity should be avoided and the network infrastructure should be simple as well. This can be accomplished in various ways, but good networking choices greatly help. For instance, LoRa (and most of the wireless techniques usually employed) operates in unlicensed bands so that it does not introduce costs for wireless communication. Moreover, its topology allows avoiding the complexity of mesh networks, connecting directly to the base station, reducing both complexity and costs.

Finally, the network should be scalable, allowing densification of the nodes while maintaining a high quality of service, as the number of intelligent devices connected LPWA networks still expect a massive growth in the future. By the way, this is also a good reason for adopting lightweight medium access control (MAC) protocols.

It is not easy to develop intelligent techniques enabling a new generation of IoT devices, but the effort in developing new energy-aware devices is paid back by the number of advantages that the IoT paradigm ultimately brings.

In the rest of this section, a couple of examples of IoT devices are reported, with some common characteristics but slightly different implementations. The first is a pollution monitoring system, designed to be self-sustainable and compact.

1.2.2 Design example: Energy neutral pollution monitoring

The first reason for being interested in air pollution is its consequence on human health: World Health Organization (WHO) has identified in air pollutants the cause of many respiration diseases [20], [21].
In the framework of a smart city, health and wellbeing of all the citizens are enhanced by a proper air quality plan [22].

Currently, the measurement of pollutants concentration in air is performed by means of weather and pollution monitoring stations located in fixed locations within a city or a geographical area. These are expensive and just a few are deployed around a city.
In the literature there is a number of pollution monitoring examples, sharing (more or less) a common IoT vision, in which data sensed remotely are used and processed in the cloud, eventually using big data analytics and producing valuable results [23], [24]. Nowadays, it is possible to use commercial sensors, implementing low-cost, low-size sensors exploiting, for instance, MEMS sensors [25]–[27]. However, one of the main issues in sensing gas and particulate matter is the relatively high power consumption of the sensors. Energy harvesting techniques have gained an increasing interests in the last decade to extend lifetime of embedded monitoring systems as enabling technology for the *"deploy and forget"* paradigm.

In the following, the system design and evaluation of a compact pollution monitoring equipment is presented. It is powered by a mini photovoltaic cells array, embedding particulate matter, carbon monoxide (CO) and volatile organic compounds (VOCs) sensors for air quality estimation. Energy budget analysis shows that energy neutral operations can be achieved enabling sustainable IoT.
The building blocks composing the prototype are shown in Figure 1.1 where it can be noticed the distinction between energy harvesting blocks and energy management parts. The pollution monitoring application is developed on a Nucleo board, running a STM32F401 microcontroller which manage the sensors and a LoRa radio for transmitting the sensors readings. The sensors employed are also commercially available, as the rest of the components, and they are the PPD42NS dust sensor [28] for particulate matter assessment and the MiCS-5121 MOX gas sesnsor [29] targeted to CO/VOCs volatile chemicals. These are quite common and their characteristics were already investigated [30], [31].

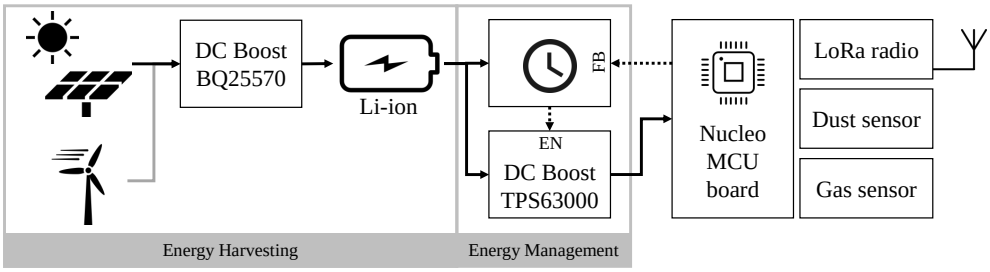

FIGURE 1.1: Overall architecture of the prototype. Dashed arrows indicate enable and feedback signals (EN and FB) while continued line arrows are power flows.

Energy harvesting

Solar modules Harvesting energy from solar radiation is often a good idea to extend the battery life of an electronic device, especially for outdoor applications. If solar radiation is sufficient it is possible to easily achieve energy neutrality for a number of sensing applications, even if in indoor environments this is still challenging. However, the high variability of this power source practically imposes to use large energy buffers, like batteries to ensure proper operations of the node. The photovoltaic modules (PV) evaluated for this prototype are quite small, in order to build a compact system, and they are *(i)* a commercial off the shelf (COTS) mini-PV module (1 W nominal, 100x80 mm system from Seeed Studio[1]), *(ii)* a custom assembled module with 50 cells from Ixys[2] arranged in a 5s by 10p matrix and *(iii)* a custom assembled module built with 12 paralleled cells from Sanyo[3]. A 2450 Sourcemeter from Keithley was used to characterize the solutions in 500 lux and 1 klux diffused irradiance conditions [32]. The results are shown in Figure 1.2. These kind of curves are well known yet useful to assess the performance of an energy source and make it work at its best. The resulting choice was the COTS solution, which outperforms the others.

DC boost converter The BQ25570[4] by Texas Instruments is an IC for energy harvesting. It features an ultra-low power boost converter with maximum power point tracking (MPPT), it is able to charge small batteries (e.g. lithium ion ones) or super capacitors and it has a regulated output for powering electronics. The MPPT working point was set at 80 % of the open-circuit voltage, as result from the characterization of Figure 1.2 and customary for PV panels. Its efficiency is very high, reaching

[1] Datasheet at https://www.seeedstudio.com/1W-Solar-Panel-80X100-p-633.html
[2] Datasheet at http://ixapps.ixys.com/DataSheet/20110302-KXOB22-12X1-DATA-SHEET.pdf
[3] Datasheet at http://docs-asia.electrocomponents.com/webdocs/0d10/0900766b80d10cee.pdf
[4] Datasheet at http://www.ti.com/product/BQ25505

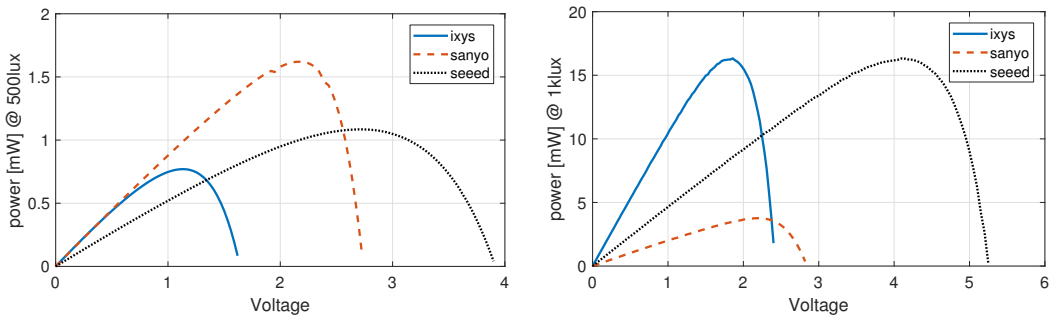

(a) (b)

FIGURE 1.2: P-V characteristics of considered mini PV arrays at 500 lux (a) and 1 klux (b)

more than 90 %. However, the output regulator is able to handle only small currents and is not enough for the (generally high) power hungry gas sensors.

Energy management

DC Boost converter Because of the need of an external DC converter for powering the electronics and sensors, a second boost converter is needed, and the TPS63000[5] by Texas Instruments was chosen. This IC can handle currents up to 1 A and, despite showing a slightly lower efficiency with respect to the BQ25570 (around 82 %), it has a convenient shutdown state (controlled by the EN port in the schematic of Figure 1.1) featuring only a low leakage of about 30 µW.
It is directly connected between the battery and the sensor node, but its operation is timed by a nano-power timer (the clock block in Figure 1.1), which is set to trigger the operation of the node at specific time intervals by means of the enable signal (EN) issued to the TPS63000.

Nano-power timer The TPL5110[6] by Texas Instruments consumes a very little power, providing a convenient timing source for duty-cycled systems. It directly commands the state of the TPS63000, turning on the main microcontroller (MCU). A feedback signal (FB) is then issued by the microcontroller to the timer to reset its state, in the very same way as a SR latch works. The consequence is that the enable signal is driven low, shutting down the TPS63000 and in turn the entire system.
The very same behavior could be achieved using the RTC peripheral of the microcontroller, putting it in low power mode and wake it up at specific time interval. The use of the TPL5110 timer is driven by its low-power footprint, featuring

[5] Datasheet at http://www.ti.com/product/TPS63000
[6] Datasheet at http://www.ti.com/product/TPL5110

a standby power (i.e. timer mode state, that is most of the time) of just 0.3 µW. Just for comparison, the standby power of the STM32F401 microcontroller used in this prototype is about 60 µW. The solution of this external timer is clearly advantageous, leading to a near-zero standby power condition. The result is an intermittent operated system, whose period is set through the TPL5110 timer using a variable resistor. The accuracy of time intervals provided by the TPL5110 is not extremely high (around 1 %), but it does not represent a problem as strict timing is not a requirement, since the environmental parameters change slowly.

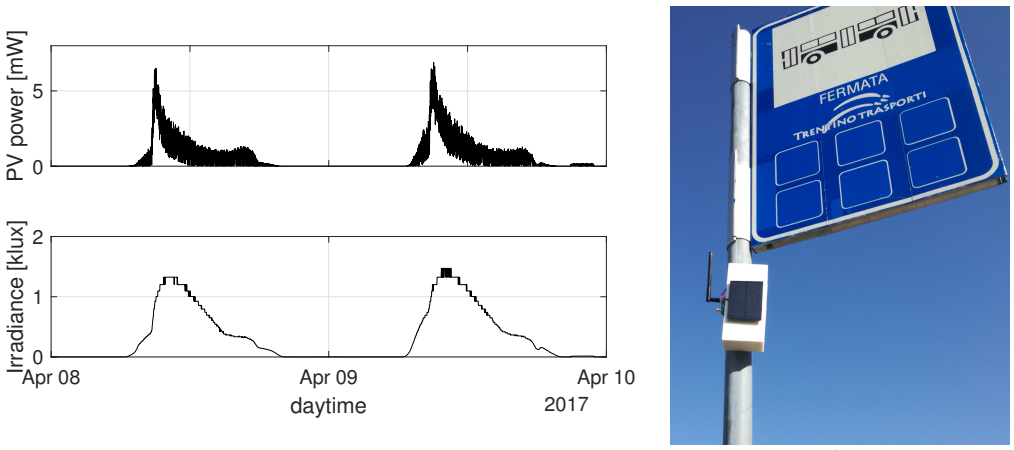

FIGURE 1.3: In (a) the data collected from the laboratory prototype as indoor irradiance near window and relative power havested by the system, while in (b) the on-the-field prototype location.
(from [32] with permissions)

Results

The power consumptions of the pollution monitoring node in all its parts are listed in Table 1.1. The prototype used to run for several days in the proximity of a partially shaded window in a laboratory environment, thus enabling to adjust the timer interval to obtain an energy neutral behavior. The solar irradiance and respective power collected by the PV module are measured and shown in Figure 1.3 (a), while in (b) a picture of the prototype deployed on the field is shown. While the indoor irradiance values are always lower than 2 klux, the outdoor ones can easily exceed 3 klux.

With these data, it is possible to balance the energy extracted by the energy harvester during a typical day with the energy used by the application and estimate the interval between sensing operations that allow a proper balance. For instance, if we assume six hours per day with 1 klux irradiance (≈16 mW production) and

TABLE 1.1: Laboratory measurement of power consumptions and efficiency of the components of the pollution monitoring node.

Energy harvesting	PV output - Ixys @ 500 lux	0.7 mW
	PV output - Ixys @ 1 klux	16.3 mW
	PV output - Sanyo @ 500 lux	1.6 mW
	PV output - Sanyo @ 1 klux	3.7 mW
	PV output - Seeed COTS @ 500 lux	1.1 mW
	PV output - Seeed COTS @ 1 klux	16.3 mW
	BQ25570 efficiency	≈92 %
Energy management	TPS63000 - Leakage	33 µW
	TPL5110 - switch ON	135 µW
	TPL5110 - timer mode	<1 µW
Application	MCU+Radio+Sensors - ON	524 mW
	MCU+Radio+Sensors - OFF	<1 µW

considering a total 73 % double conversion efficiency, we can expect 70 mW h of available energy delivered to the load. This energy is enough to sustain the node for one day if environmental monitoring is performed every 45 minutes. A similar computation can be done considering different periods for irradiance and sampling frequencies. The summary of this evaluation is reported in Figure 1.4 whose bars show the number of energy neutral operations achieved as a function of irradiance hours per day and the sampling frequency. When energy neutrality is not achieved, no bar is shown in Figure 1.4.

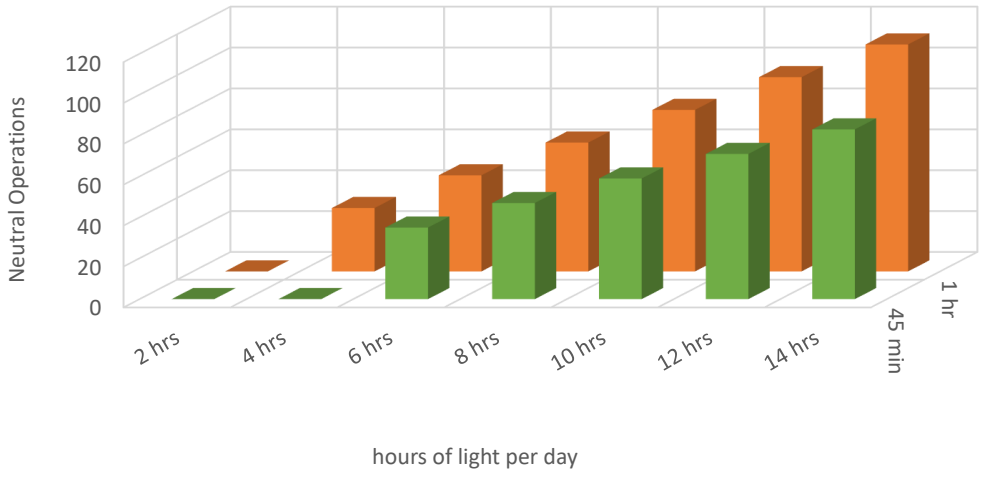

FIGURE 1.4: Prediction of the feasible energy neutral operations, based on the measurements on the prototype, with respect to the fixed sensing periods (45 minutes or 1 hour) and the hours of light per day.

Conclusion remarks Laboratory results demonstrate that the monitoring system can be completely self-sustainable sampling the environmental parameters every 45 minutes. This power-hungry system was made energy autonomous by duty-cycling the operations of the whole sensor node electronics without losing functionality. However, in the case of addressable wireless sensor nodes, this approach actually reduces functionality, being the system completely off for long periods. A solution is represented by wake-up radios, which are conceived to reduce the power overhead of the wireless communication subsystem.

1.2.3 Wake-up radios

from a hardware perspective, what is really power demanding in a wireless sensor node is the radio subsystem. On the other hand, it is not possible to remove it: wireless communication is one pillar of IoT systems, permitting the ubiquity of information. One of the most important challenges therefore is reducing power when radio is in idle, i.e. the so called *idle-listening cost*. A wake-up circuitry is capable of detecting an incoming transmission, optionally discriminating the packet destination using addressing, then switching the main radio on only when needed [33]. Such circuitry is called wake-up receiver (WuRx) and together with the corresponding network and MAC layer protocol (that have to be implemented jointly with the WuRx), a wake-up radio (WuR) system can be built.

A wake-up receiver is characterized by some key design considerations:

1. **Power consumption** is the main specification, imposing that the WuR power consumption must be well below that of the main radio.
2. **Time to wake-up** is the latency between the reception of the wake-up signal and the actual starting of operation.
3. **Interferences** which may introduce false wake-ups. In fact, due to the low-power budget, the modulation techniques used in WuR are simple, e.g. on-off keying (OOK), pulse width modulation (PWM) or amplitude shift keying (ASK).
4. **Sensitivity** that, in general, is proportional to the power consumption of the WuR and its operational range. Because of that this is a very important design parameter, often resulting from a trade-off with power consumption. In modern implementations of WuRs the range is in the order of tens of meter.

5. **Data rate** also influence the overall power consumption, but also the sensitivity to interference and latency. So high data rate can be seen as a way to improve the overall energy efficiency of the system.
6. **Cost and size** depend on the complexity of the design, and, to enable the integration in existing IoT nodes, it should not exceed 10 % of the total cost [33].

Wake-up radios can be classified. The main distinctions identified are on the power source, addressing capability, channel usage and communication medium.

Power The WuRx can be *passive* if it does not require continuous power and it is able to harvest energy for its own operation. This energy comes from the ambient or, in particularly efficient designs, from the wake-up signal itself.
Although energy efficient, these receivers usually have shorter operating ranges due to limited sensitivity with respect to the *active* counterpart. This second kind of WuRx are externally powered, but have limited capabilities with respect to a typical, full-featured, higher-power radio transceiver. Therefore, the objective of these designs is the reduction of the standby power consumption by means of a dedicated radio able to receive the wake-up beacon.

Addressing The wake-up signal can optionally include an identification code (ID). Thus ID-based WuRx can be addressed in the network, reducing the probability of false wake-up. However, the design is more complicated as a decoder and a longer wake-up signal are needed. On the contrary, broadcasting the wake-up message to all the network nodes results in a two-step addressing, but a simpler WuRx design. This approach can be detrimental in terms of total system power consumption. However, with a proper MAC technique, broadcast-based WuRxs have comparable characteristics w.r.t. the ID-based systems.

Channel Depending on the relative channel difference between the wake-up and the main radios, it is possible to design the system with separate signal paths. An *in-band* WuRx uses the same channel as the main node, making it possible to to use a single antenna, while *out-of-band* WuRx operates on a dedicated frequency, different from the main radio. The latter have usually improved strength with respect to interferences but higher system complexity.

Medium In a broader vision, a WuRx may include also non-radio implementations. In the scientific literature several examples of acoustic wake-up receivers and optical ones are reported. In the following section, a passive wake-up receiver operating on power line is presented as well.

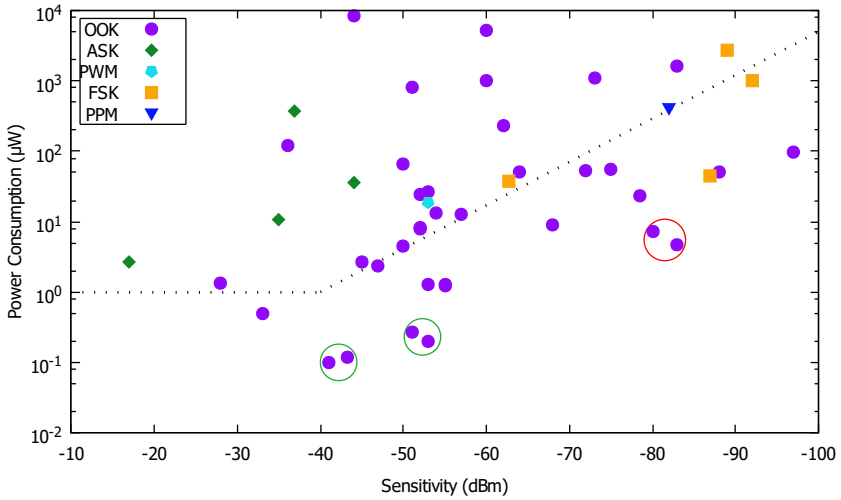

FIGURE 1.5: Sensitivity of low power RF based wake-up receivers vs. power consumption. Different symbols refers to different modulation schemes, as in the legend.
(from [33] with permissions)

State of the art

When comparing different WuRx designs, it can be noted that most of them use simple modulation schemes like On-Off Keying (OOK) or non-coherent Frequency Shift Keying (FSK). This is driven by the easiness of decoding, for instance with a simple diodes-capacitor envelope detector. Most of the WuRx with power consumption below 10 µW rely on OOK modulation [34]. In contrast this is sensitive to noise, while FSK, for instance, is more resilient. Another simple approach that can be found in the literature is the use of pulse-width modulation (PWM) and an integrator as demodulator [35].

Figure 1.5 briefly depicts the result of the literature survey on sensitivity performance versus power consumption.
Among the 75 prototypes surveyed in [33], only 23 reported a power consumption below 10 µW. Some WuRx designs are particularly energy-efficient and are highlighted with circles in the figure. For instance, the green circles highlight some prototypes for short-range applications (as body area network) exhibiting power consumptions below 0.27 µW and sensitivity around −40 dBm to −56 dBm, while the red circles refer to mid-ranges applications devices achieving better than −80 dBm sensitivity. The lowest power consumption achieved is 98 nW [36]. Empirically it was found with a slope-fitting that a 20 dBm gain in sensitivity leads to an increment in power consumption by a factor 10.

The wake-up radio technology is ready to impact devices power consumption positively. Many application fields can be identified. Among them, wearable devices (as enabler for wireless body area network), smart city applications and smart metering are the most promising.

1.2.4 Design example: Wake-up radio deployment

An interesting application of a wake-up radio has been developed using a plant-microbial fuel cell (PMFC) as power source. The application is built on top of a popular radio node, i.e. a Tmote Sky [37]. As further complication, such node is quite old and not oriented to low-power applications. The use of a wake-up receiver enables to couple the small amount of power that the PMFC outputs to the target application, using a receiver initiated MAC-level communication protocol. As result, a self sustainable system is realized, showing reasonable data rates (one transmission every 30 s).

The building blocks are described in the following and shown in Figure 1.6 (a), where, as in the previous example, the division between energy harvesting blocks and energy management blocks is clearly visible. The picture of the prototype is shown in Figure 1.6 (b) as well.

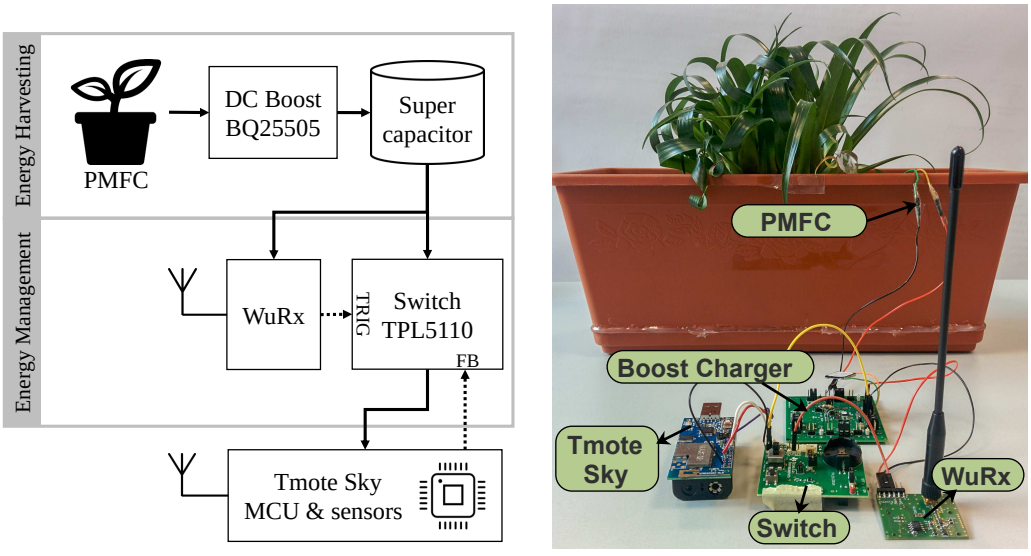

(a) (b)

FIGURE 1.6: Overall architecture and picture of the prototype. Dashed arrows indicate trigger (TRIG) and signaling (FB) while continued line arrows are power flows.
(from [38] with permissions)

Energy harvesting

MFC Microbial fuel cells (MFCs) are biological reactors, where the so-called *electrogenic* bacteria produce a small current as result of their own metabolism [39], [40]. These microbes are curiously easy to find, being commonly present in many soils and sediments on the planet. The special kind of MFC built with such bacteria are called Sediment-MFC [41], while, if a vegetable take part in the electro-chemical reactions inside the cell, a Plant-MFC (PMFC) is realized [42]. The typical continuous power that these systems can deliver ranges between 50 and 100 µW at 0.3 to 0.6 V.
The PMFC built in laboratory for this prototype is made of very common elements: soil from the university courtyard, a standard houseplant and a couple of graphite fiber felt electrodes. After some days to let the bacteria colony grows, a stable output power of 70 µW can be reached. Extensive characterization of a PMFC power output has already been done in literature [43]. Figure 1.7 shows the maximum power output of a PMFC prototype cell as function of voltage [44]. However, in order to fully exploit the potential of PMFCs, some care is needed, developing a specifically tailored energy management technique. For instance, it was observed a reduction of performance of the cell during long intensive loads, further increasing the need of intermittent operations to let microbes recover [38], [45].

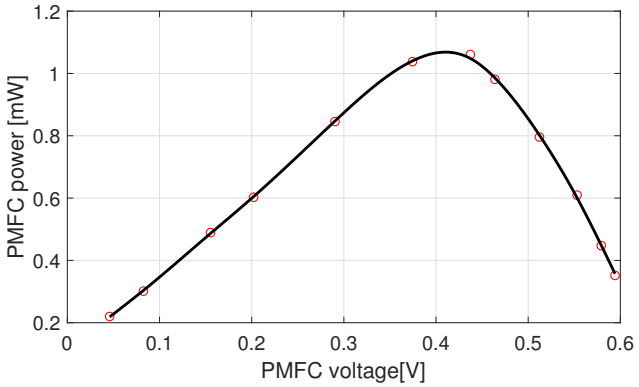

FIGURE 1.7: Static Power-Voltage diagram of a PMFC
(from [44] with permissions)

DC boost converter The energy harvesting module is based on a Texas Instruments BQ25505 boost charger [7] (which is very similar to the BQ25570 previously introduced). This specialized IC is capable to start its operation at a voltage as low as 0.33 V and with a minimum input power of only 15 µW, which are compatible with the PMFC output characteristics. Moreover, it embeds a maximum

[7] Datasheet at http://www.ti.com/product/BQ25505

power point tracking (MPPT) feature. Through experiments, the efficiency of the converter was found to be around 90 %.

Energy buffer A super-capacitor is used to store the energy collected by the DC converter. This is a key element, as the power demand of the application is higher than the output power that the PMFC is able to supply. Thus a continuous operation is obviously not possible. The size of the capacitor is 22 mF, i.e. large enough to store 33 mJ of energy usable by the main node when triggered by the wake-up radio. The size of the capacitor was chosen to conservatively provide energy at a sufficient voltage level for the Tmote board to work.

Energy management

Wake-up receiver A number of wake-up radios have been presented over the last few years [33]. The design advantages are firstly related to the low power consumption, at the expense of a little higher latency. The difference is huge: the CC2420 radio of the Tmote Sky requires 18.8 mA in listening mode, while the wake-up receiver used in this work requires only 0.56 µA [46]. This WuRx operates in the ISM 868 MHz band and has a sensitivity of −55 dBm. The maximum operating range is 50 m. Consuming only 1.68 µW, the wake-up radio is able to address a node in 16 ms (using the 16-bit addressing mode).
Because of the intrinsic structure of the WuR, the power consumption in listening mode is very small. After the receiving the wake-up signal, the decoding operations increase the power consumption up to roughly 1 mW. This is not an issue though.

Nano-power switch While the WuRx is constantly powered by the energy harvester, the main node drains energy from the capacitor by means of a timed switch, operated by the WuR. This is needed to turn off completely the Tmote Sky, therefore setting its standby power consumption to almost zero. The switch chosen is the TPL5110[8] which incorporate a MOSFET driver and a low-power timer as well. Unlike the previous example reported in Section 1.2.2, the TPL5110 is now operated only as a switch, triggered by the WuRx (TRIG signal) and reset by the main node (FB signal) when the operations are concluded. The overall consumption of this module (always connected to the energy harvester) is 35 nA.

[8] Datasheet at http://www.ti.com/product/TPL5110

Results

The stand-by power consumption was reduced from 130 µW (Tmote Sky in sleep) to 1.8 µW with the advantage of having the remote addressing feature introduced by the WuR. Figure 1.8 shows the final power consumption of the prototype during the wake-up, sensing and transmitting operations.

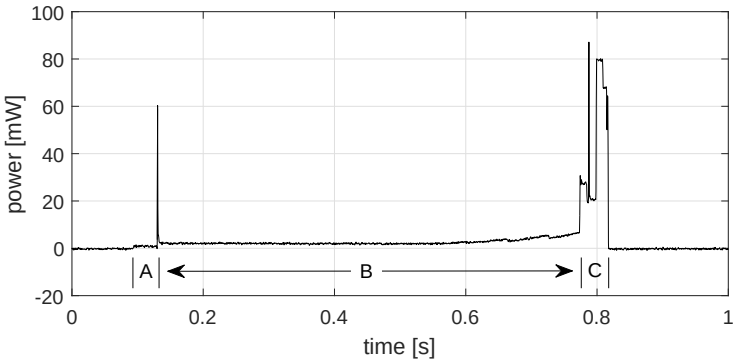

FIGURE 1.8: Power consumption measurement of the remote sensor node with radio-trigger. The measurement starts at the trigger (A), then the node boot (B) and finally transmit the measure (C). (from [38] with permissions)

During each sensing operation, triggered by the wake-up receiver, three phases can be identified. Firstly, the WuRx decodes the incoming signal, causing the first step in power consumption (from 1.8 µW to 1.02 mW). This phase lasts for about 16 ms and is labeled as *A* in Figure 1.8. Then, in region *B*, the main node boots and enter in sleep mode which requires 43 µA. This period lasts at most 640 ms and is required by the board to stabilize the crystal oscillator and boot. Finally in *C* the sampling operation is performed and the resulting value is transmitted by the main CC2420 radio on board. After that, the feedback signal to the timer is issued, thus switching the node off. Summing up all these contributions, the total energy absorbed is about 3.6 mJ.
Table 1.2 lists the current consumptions measured on the Wake-up receiver, switch module and Tmote board.

In the example described, a wake-up receiver was employed, enabling to use a power hungry sensor node. Actually, some simplifications can be done in the case of newer radio transceivers. For instance, the CC1310 power consumption in sleep mode is less than 1 µW and was used in conjunction with wake-up radios and PMFC with no need of turn it off [47]. As key for a successful implementation of IoT devices using an extremely low power source, an in depth characterization of such power source is always needed. This allows designers to properly tune

TABLE 1.2: Laboratory measurement of power and current consumptions of the components of the node.

Energy harvesting	PMFC output - average	70 µW
	PMFC output - peak	300 µW
	BQ25505 efficiency	≥90 %
Energy management	WuR - listening	0.56 µA
	WuR - decoding	340 µA
	Switch - idle	35 nA
Application	Tmote - TX mode	19.5 mA
	Tmote - RX mode	21.8 mA
	Tmote - deep sleep	43 µA
Total operation energy		3.6 mJ
Baseline power consumption (WuR listening + BQ25505 + TPL5110)		1.8 µW

the power consumptions of the sensing application, and eventually make suitable trade-offs. The deployment of a wake-up radio system permits to further decrease the power consumption thus enabling new possibilities for a pervasive IoT growth.

1.3 Smart Lighting

In 2006 the total energy demand for lighting covered the 19 % of the total electricity consumption, globally [48]. This is an extremely high share, impacting on the city finance by about 20 % on the budget for the outdoor lighting and up to 40 % for indoor appliances. Moreover, lighting is a also a great source of greenhouse gas emissions (accounting for up to 70 % w.r.t. the emissions due to road traffic). Luckily, in the last decades, LED technology has become widespread and used in many field, including outdoor lighting. Therefore, the power consumption was greatly reduced, as reported by International Energy Agency for buildings [49].
For street lighting the scenario is similar, allowing municipalities to both save money and enhance the infrastructure employing the lighting grid for different purposes. The role of ICT for outdoor lighting can be relevant indeed, helping to reduce energy waste, light pollution and greenhouse gas emissions [50]–[52], but also developing services as CCTV or smart parking on the lampposts.

The geographical extension of the street lighting networks poses serious problem when it is needed to update it. Light bulbs are already being replaced in many places, under the stimulus of regional funds aiming to increasing energy efficiency.

However, innovative services need connectivity also. Among others technologies, Power Line Communication (PLC) is more convenient to implement a smart lighting system. Eliminating the costs of dedicate wiring and antennas installation, PLC enables to communicate over the same grid used to power the lamp posts, thus exploiting an already-in-place, secure and huge network.

1.3.1 Power Line Communication

PLC can be divided in two categories with respect to the frequencies used:

- **BroadBand-PLC** is the higher frequency, higher bandwidth type, with typical frequency in the 1.8 MHz to 250 MHz interval. It has been developed mainly for Local Area Networks and last-mile networking applications [53]. Because of the high frequencies used, this is not the best choice when the distances to be covered are longer than hundreds of meters.
- **Narrowband-PLC** is its slower counterpart. It works mainly in the frequency bands regulated by the European regulation CENELEC EN 50065-1 [54], which specify four low-frequency bands between 3 and 148.5 kHz. This technology is more interesting for implementing wide area networks because of its versatility, especially for smart grid applications.

NB-PLC solutions have received increasing attention for smart grid applications thanks to the relatively low implementation cost and the ability of NB-PLC signals to propagate over long distances (up to several km), even through transformer [55]. PLC technology is therefore used for a wide set of applications [56]–[58]. It is already used in many countries to implement automated meter reading (AMR) infrastructures for remote smart metering applications [59], [60]. PLC has the potential for being the key for the implementation of grid automation. In fact, unlike wireless communications, PLC is intrinsically more secure and the communication lines are already in place. The implementation perhaps is not straightforward, depending on the specific peculiarity of the grid, its topology, the interconnections and the devices connected to it [61]–[64].
In the case of smart lighting systems, the scenario is slightly simpler to approach: all the appliance connected to the grid are lights and the structure of the grid is quite uniform. Pushed by the possibility to automatize the lighting control, many protocols and standard were introduced to address the specific needs of lighting systems. Just to cite some of them, PRIME-PLC [65] and G3-PLC [66] guarantee high communication ranges and good data rates to implement lighting systems [67].

1.3.2 Design example: A wake-up receiver for PLC

The simplest solution to remove any power consumption of an appliance is to unplug it, physically disconnect it from the mains. The technology often permits to achieve the same power performance (i.e. zero power) preserving the stand-by operating mode, and this is often regarded as zero-power stand-by.

Similarly to the previously introduced wake-up radios, the system described in this section provides the wake-up functionality to a power line modem (PLM) for smart grid applications and in particular for smart lighting systems.

The architecture of wake-up receivers is quite uniform. The implemented wake-up receiver is aligned with the traditional scheme, and it is composed by: *(i)* a decoder, needed for implementing the addressing functionality, *(ii)* an energy harvester that scavenges energy from the signal itself and powers the decoder and finally *(iii)* a switching relay to turn on the main transceiver, namely the PLM itself. This last element can represent a potential issue because of the typically high power consumption of a relay. However, a clever solution has been implemented to avoid this and was proven to work well, with the additional advantage to be easily applicable not only to wake-up PLMs but, in theory, for every appliance connected to the grid.

Hardware Prototype

The prototype is based on an energy harvester that exploits the energy carried by the wake-up signal to energize the decoder part of the wake-up system, realizing therefore a passive wake-up receiver.
The prototype can be decomposed in three parts:

- an energy harvester, based on a voltage multiplier scheme;
- the decoder, i.e. a low-power microcontroller;
- a relay element, which turns the main node on.

Energy harvester The design of the voltage multiplier (VM) is based on the Cockroft-Walton scheme and it requires particular care on some parameters affecting its performance. For instance, relevant losses are caused by the diodes forward voltage and the capacitors ESR (Equivalent Series Resistance). In a smaller share also the diodes leakage current can affect the multiplier performance [68], [69]. The behavior of the Cockcroft-Walton VM can be predicted using both theoretical results (e.g. in [68] the losses are modeled) and data simulated with SPICE. It was found that the

most convenient number of stages of the multiplier is 5, which provides a usable voltage at the end of the multiplier chain. Capacitors size also affects the performance of the energy harvester but also contributes to lower the overall impedance of the system at the PLM working frequencies. This can be a relevant problem when it comes to scale the system to a big network. Moreover, at the end of the multiplier chain there is another (relatively small, i.e. 200 µF) buffer capacitor. This is needed to provide an energy reservoir during during the reception of the signal.

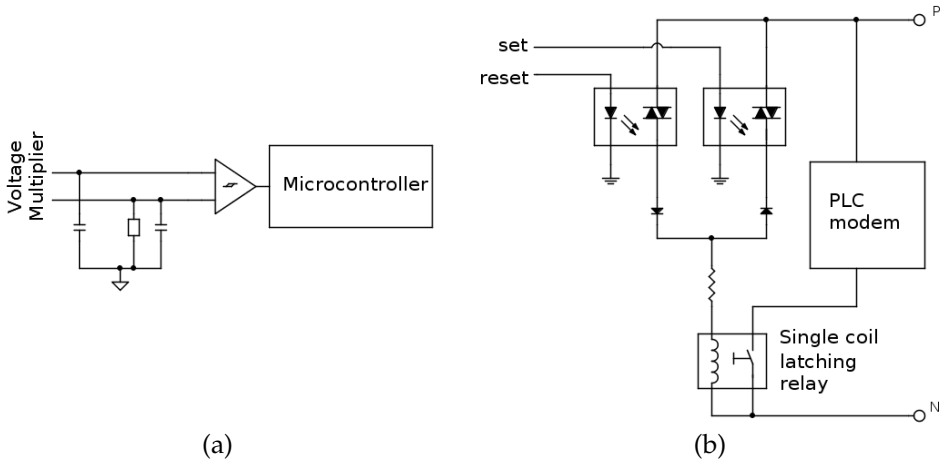

FIGURE 1.9: In (a) the signal demodulator circuit: two branch on the voltage multiplier provide the two signals depicted in figure **??** to the comparator, then the microcontroller decode the signal extracted and turn on or off the PLM with the two signals in (b) representing the two stages relay solution.

Signal and decoder The wake-up message is designed to be easily decoded and provides sufficient power to the wake-up circuitry. Manchester encoding is used, to exploit its constant power transmission during the message. The energy buffer is designed to supply the electronics during the low part of the bit period. At first a long high-gain signal is transmitted as preamble to provide the energy for the correct start-up of the decoder. Then a sync phase is used by the wake-up system to detect the bit rate of the message. A start bit closes the sync phase. It follows a code, used to address the nodes and finally, a last high gain phase is needed to provide the final energy burst to trig the relay. The signal consists of several FSK (frequency shift keying) modulated packets generated by another PLC modem, and then further modulated in amplitude to build an OOK (on-off keying) message. The decoder in fact works discriminating the level of the signal coded with the OOK modulation. A Comparator in Schmitt trigger configuration provides a clean signal out of two noisy signals extracted at two consequent branches on the voltage multiplier chain. As can be seen in figure 1.10 (a), one signal has a quite

constant slope (the yellow one in the figure) while the other (i.e. the green noisy one) follows the slope of the input signal because of a resistor that discharges the capacitor on that net. The implementation of this part can be seen in figure 1.9 (a). Afterward, the microcontroller decodes quite easily the message that the comparator provide, shown in figure 1.10 (b). The microcontroller used is a STM32L053 from STMicroelectronics[9], while the comparator is a TS881[10]. The components are chosen for their ultra-low power footprint: the comparator works with less than 300 nA in normal conditions, featuring a rail-to-rail output, while the microcontroller needs around 400 nA in stop mode. A convenient low-power timer can interrupt the microcontroller even when in stand-by mode and is used to decode the wake-up signal.

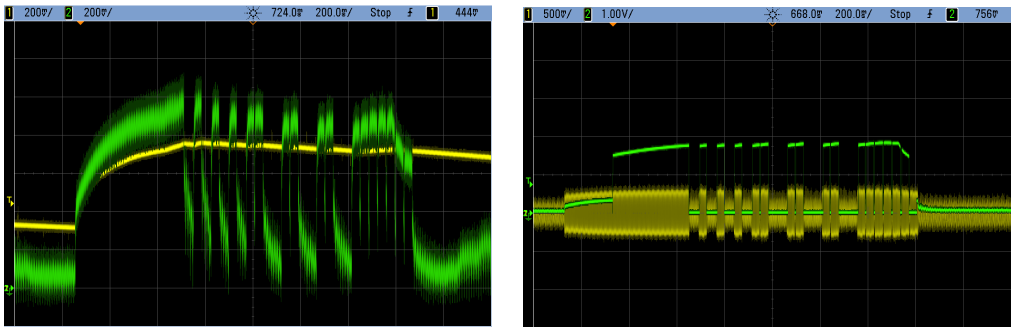

(a) (b)

FIGURE 1.10: Scope acquisitions of the comparator signals in (a) the two input signals that come from two branches of the voltage multiplier, and in (b) the output of the comparotor with respect to the input signal of the PLC wake-up system.

Switching The actual switch-on of the entire modem depends on a two-stage cascade relay. Two low-power solid state optocoupler (photo TRIAC based, i.e. IL4116[11]) provides the two signals (opposite in magnitude thanks to a couple of diodes) for driving the latching electromechanical relay. It results that the relay is operated with either the closing or opening signal from the microcontroller itself. This design is driven by the PCB limited space and power consumption constraints. An alternative solution would require a single, but bigger and power inefficient bistable relay. The implemented relay stage is depicted in figure 1.9 (b).

As a result, the system is able to produce the switch-on of the modem from the power harvested from a simple PLC signal.

[9] Datasheet at https://www.st.com/en/microcontrollers-microprocessors/stm32l053r8.html
[10] Datasheet at https://www.st.com/en/amplifiers-and-comparators/ts881.html
[11] Datahseet at https://www.vishay.com/optocouplers/list/product-83628/

Results

The prototype, shown in Figure 1.11, was tested in laboratory while connected on the mains and on a sample cable 100 m long. The prototype shown is able to work with an input signal of 560 mV peak-to-peak. Considering the maximum signal magnitude allowed by CENELEC regulation in the NB-PLC bands (which is 10 V peak-to-peak), the system work with a line attenuation of 25 dB (tested with a line impedance stabilization network also). However, because the energy harvester intrinsically has a low impedance, it decreases the PLC signal gain, also affecting the signal propagation negatively. This insertion loss effect, although present, does not harm the reception of the signals, because the main PLM has input amplifiers and high sensitivity (for instance, the ST7580 used as main modem has a rated sensitivity of 39 dB µV RMS for FSK encoded messages).

Moreover, it is almost impossible in real PLC networks to work in proper impedance matching conditions, even if some limits are imposed by the CENELEC regulation on the minimum impedance of the network at the working frequencies. This is mainly due to the fact that the power lines are not designed to transmit data. Thus every junction and discontinuity can introduce noise and attenuate the signal. Therefore, the slightly lower impedance exposed by the wake-up circuitry (w.r.t. the PLM) only partially influences the reception of the signal.

To further investigate how the signal propagates in the presence of wake-up receivers, PLMs and lights, a simulation approach was chosen.

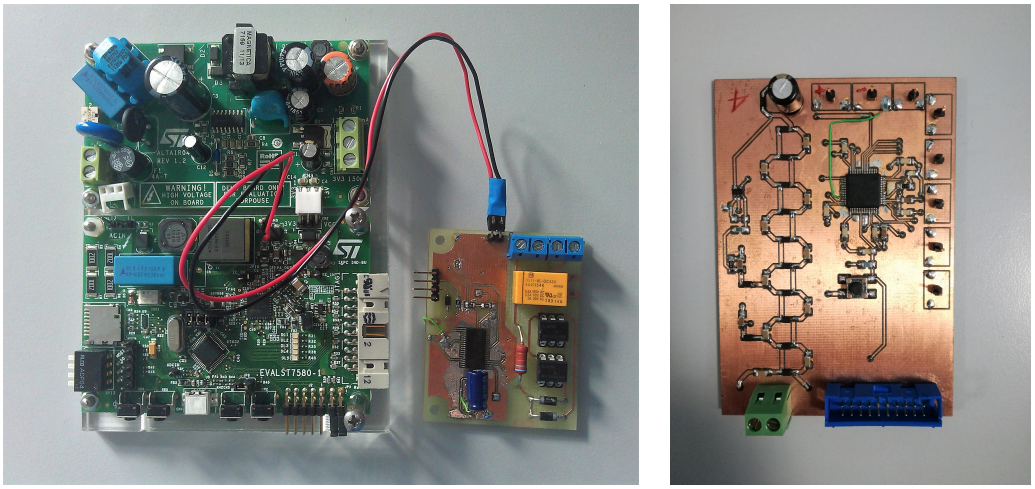

(a) (b)

FIGURE 1.11: Picture of the prototype produced with the main PLM in (a) and in a prototype version in (b).

1.3.3 The network view

When a system is supposed to interact with other nodes on a network, some rules need to be posed. It would be easy to transmit a wake-up signal with a lot of power, in order to easily cross the network and reach a specific node. Besides the presence of disturbing elements, like lamp ballasts, connections and branches, there are also regulations, which impose certain frequency and power output.
The CENELEC EN50065 regulation on *Signalling on low-voltage electrical installations in the frequency range 3 kHz to 148,5 kHz* [54] imposes limits on the transmission level for PLC modems and impedance of the devices connected to the PLC network.

Simulation model

A smart street lighting network based on PLC is usually managed from a *concentrator*, located at the beginning of the line or in strategic locations. Then every lamp post has its own PLC modem (PLM) and lamp ballast. For simulation purposes the lamp posts are considered 7 m high, equally spaced with an inter-pole distance of 20 m. The developed simulator is flexible enough to allow the user to change these parameters depending on the specific scenario considered. A schematic of a simulated network is depicted in Figure 1.12, where the light bulbs represent the lamp ballasts and the transformer icon denotes the line coupling element of the PLM, i.e. the element exposed to the network. In the following all these elements are listed.

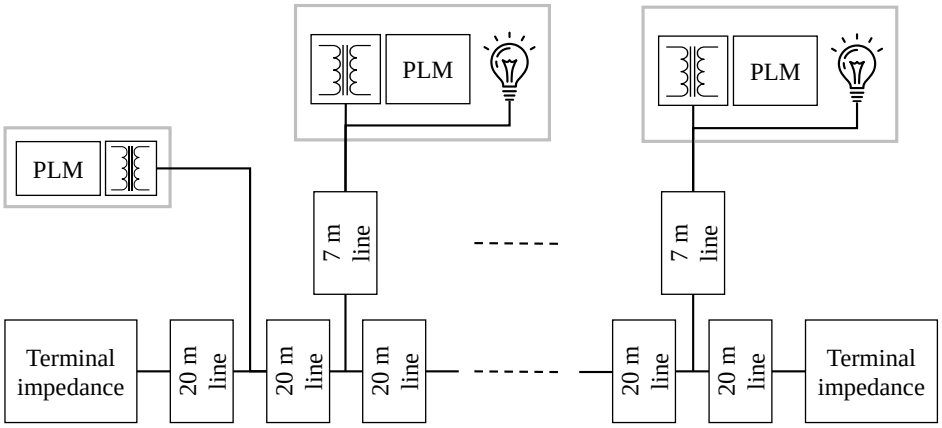

FIGURE 1.12: Example of a street lighting network as it was simulated.

- **PLC modems.** They have usually a proprietary architecture, that depends on design choices and specific implementations. Nevertheless, some elements are in common, as the input coupling section. This is usually implemented using a transformer and a capacitor to provide proper isolation. An inductance complete the electromagnetic interference (EMI) filter. A general electrical model of a PLM is hard to define. However, according to existing standards, the equivalent input impedance of such modems has to lie within given ranges. Since the total reactance associated with both the transformer and the EMI filter is much larger than the reactance of the modem's internal circuitry, the latter terms can be neglected. As result, the digital signal processing section of a PLM (typically based on a microcontroller unit - MCU) can be roughly modeled as a time-varying resistive load, which changes as a function of the power supply voltage, the computational load, and the specific features of the chosen MCU. The default nominal value of the modem input impedance is often reported in the data sheet of the device [70]. The available evaluation tool used was the EVALKIT-ST7580 based on the ST7580 transceiver. The coupling element of the modem, which is the main responsible for its termination impedance, is illustrated in Figure 1.13.

- **Lamp ballasts.** Lamps are usually driven by an electronic ballast or, in the case of old fluorescent lamps, an electromagnetic ballast. The first can be modeled as a resonant series RLC element (which is the input filtering element usually present in the lamp power supply circuitry), as in Figure 1.13. However, the capacitive element is typically the main one, realized with safety–oriented capacitors (called X-cap) whose total capacitance can be as large as hundreds of nF. Consider that the capacitive elements represent a problem, filtering the PLC signals as well.

- **Cables.** Low voltage power lines consist of 3-wires cable, i.e. the line, the neutral and the earth conductors. For communication purposes only live conductors are used. So the classic two-wire RLCG model can be used. The values of parameters R, L, C and G are given by the following expressions:

$$\begin{aligned} R &= \sqrt{\frac{\mu_r \mu_0 f}{\pi \sigma a^2}} \left[\frac{d/2a}{\sqrt{(d/2a)^2 - 1}} \right] \\ L &= \frac{R}{2\pi f} + \frac{\mu_r \mu_0}{\pi} \cdot \cosh^{-1}\left(\frac{d}{2a}\right) \\ C &= \frac{\pi \epsilon_r \epsilon_0}{\cosh^{-1}(d/2a)} \\ G &= 2\pi C f \tan(\delta) \end{aligned} \tag{1.1}$$

where

- μ_r is the relative magnetic permeability of the conductor, a typical value for copper and aluminum is $1.25 \cdot 10^{-6}$;
- μ_0 and ϵ_0 are the vacuum magnetic permeability and permittivity;
- ϵ_r is the relative permittivity of the insulating shield, it normally ranges form 1 to 2;
- σ is the conductivity ($5.96 \times 10^7\,\mathrm{S\,m^{-1}}$ for copper and $3.5 \times 10^7\,\mathrm{S\,m^{-1}}$ for aluminum);
- a is the radius of the conductors;
- d is the distance between two conductors, and is given as the sum between the conductor radius and the insulation thickness considered twice;
- $\tan(\delta)$ is the dissipation factor of the insulation (equal to 10^{-2} for PVC and 10^{-6} for G7-HEPR insulation)
- f is the signal frequency.

Model Parameters For simulation purposes, all the electrical parameters introduced before, need to be estimated. Three FROR 3G4 sample cables of different length were measured (at 100 kHz) and, if the values of each electrical parameter are divided by the respective cable lengths, the result is: $R \approx 28\,\mathrm{m\Omega\,m^{-1}}$, $L \approx 0.45\,\mathrm{\mu H\,m^{-1}}$, $C \approx 0.037\,\mathrm{nF\,m^{-1}}$ and $G \approx 0.23\,\mathrm{\mu S\,m^{-1}}$. These numbers are in good accordance with the result of the previous equations (1.1).

Considering that the typical wavelength of a NB-PLC signal is about 3 km while the distance between consecutive lamp posts are much less (tens of meters), then each branch of a street lighting network based on the purely distributed RLCG transmission line can be replaced by the cascade of a quite limited number of two-port

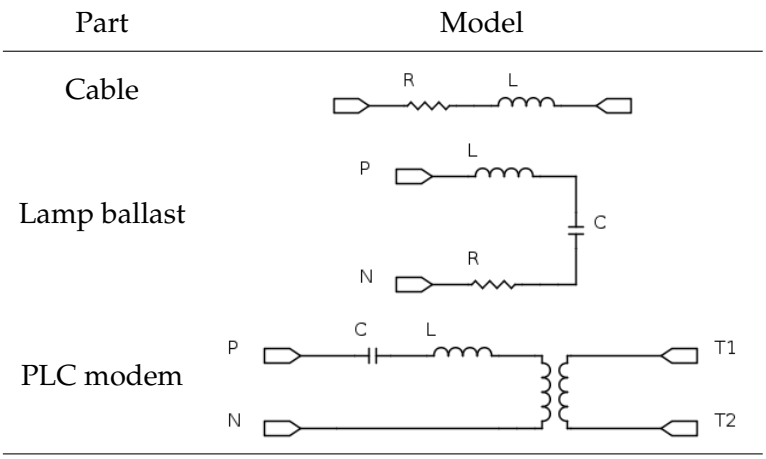

FIGURE 1.13: Equivalent circuits for simulating the cable transmission line, an electronic ballast and the coupling section of the modem.

lumped-element RLCG circuits of fixed length, thus reducing both computational complexity and simulation time substantially.

Some introductory simulations showed that the result is almost independent of the model used, i.e. regardless of the use of the G element in the model or not. Moreover, if the equivalent input capacitance of the PLC modem and the shunt capacitance of the ballast are much larger than the total capacitance of the line (as typically occurs in practice), then also the value of C can be neglected. Under these conditions, the original model becomes a simpler distributed RL model, which is less demanding from the computational point of view, thus reducing simulation time, especially when large networks are considered.

Model Validation For validation purposes, simulation and measurement results have been compared in similar conditions. Two NB-PLC modems ST7580 have been connected to the ends of three FROR 3G4 power line cables with a cross section area of 4 mm^2 and different lengths (i.e. 30 m, 60 m and 90 m, respectively). Then the transmitting modem is set to transmit a 100 kHz 10 Vpp FSK signal over the lines. On the receiver side, the line was loaded with either a resistive load or an electronic ballast for street lighting. Figure 1.14 depicts the configuration used for the validation, with the terminal impedance, the cable model and both the receiving and transmitting PLMs. The parameters of the received waveforms were measured with a Digital Storage Oscilloscope (DSO) Agilent 70321 on the receiver side, after the coupling section of the modem.
The simulations are based on the model introduced so far, implemented using LTSpice. The simulation results are in excellent accordance with the experimental data

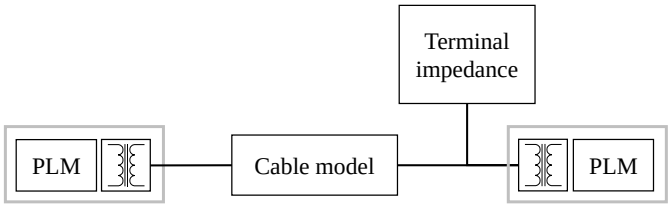

FIGURE 1.14: Schematic of the model used to validate the parameters of the cable.

in all the conditions: the relative differences between pairs of values are indeed in the order of a few percent. Such differences are also generally consistent with the estimated worst-case uncertainty, which is about $\pm 0.5\,\mathrm{V}$. This value includes not only the intrinsic fluctuations of the waveform and the instrumental uncertainty of the DSO, but also the uncertainty affecting the waveform amplitude at the transmitting end, since this parameter can be just roughly controlled by the modem and it also is partially influenced by the total line impedance.

Simulation Results

Some simulation results related to a realistic street lighting system are reported in Table 1.3. An example of schematic of street lighting network as implemented on LTSpice is shown in Figure 1.15. In this example, the distance between two consecutive lamp posts is 20 m, and each post is 7 m high. As a result, each power line is partitioned into 20 m segments. Such segments are modeled as two-port, lumped-element RL circuits labeled as *20 RL* in the figure, while the *7 RL* elements correspond to the cable of the lamp posts. Each lamp post includes a PLC modem and an electronic ballast.
The values reported in Table 1.3 are the peak-to-peak amplitudes of the FSK signals (with nominal amplitude equal to 10 Vpp) received by modems at various distances

TABLE 1.3: Simulated peak-to-peak voltage amplitude of a $10\,\mathrm{V_{PP}}$ FSK signal in different points of a street lighting network.
(from [71] with permissions)

Line length	1st node	10th node	20th node	30th node	50th node
200 m	8.36	5.28	-	-	-
600 m	8.05	2.94	1.03	0.6	-
1 km	8.05	2.94	0.96	0.31	0.07

from the transmitting node and over lines of different total length (i.e. 200 m, 600 m and 1 km), when no intermediate branches are considered.

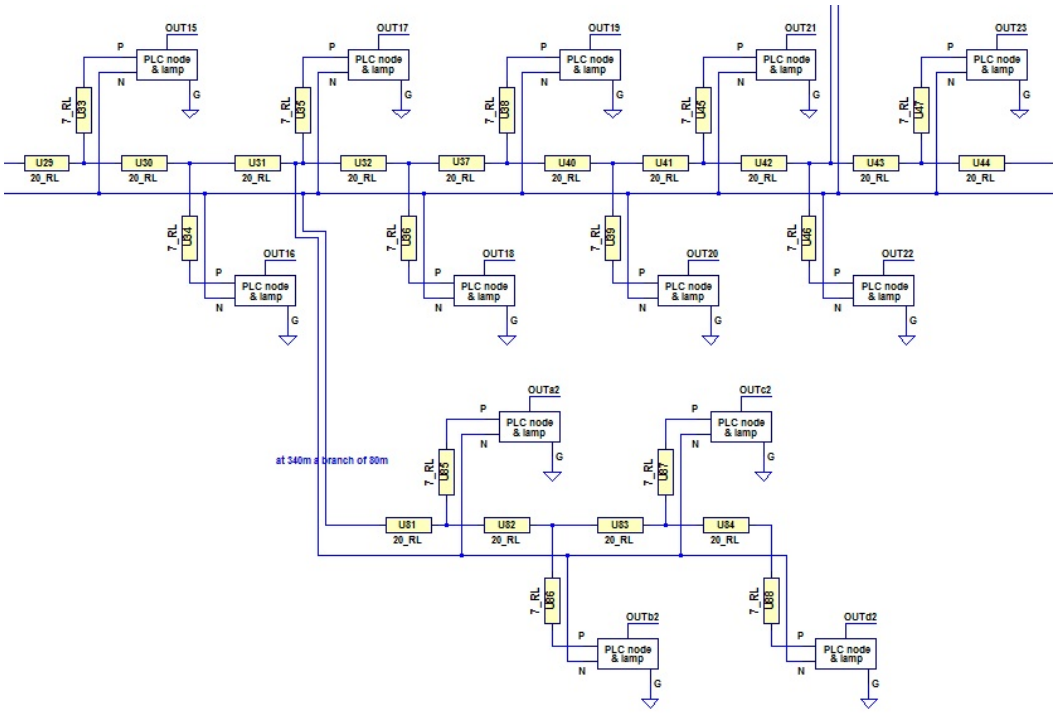

FIGURE 1.15: Schematic of a realistic street lighting network.
(from [71] with permissions)

Additional results are presented in Table 1.4. In this case, the peak-to-peak voltage values at the input of various nodes along the 600 m line are compared with those obtained when three branches are inserted at 200 m, 340 m and 440 m from the transmitter. The dash symbols in Table 1.4 denotes infeasible configurations. For instance, the eleventh node on the second and on the third branch simply does not exist. Notice that in this example the waveforms amplitude becomes quickly very small over both the main line and the various branches, thus making signal decoding harder for modems. Due to the high sensitivity of a PLM modem, the decoding of such low signals is still possible. However, the wake-up receiver presented in the previous section cannot work properly with such a low signal (mainly due to the fact that it is passive). Besides the wake-up receiver, these results confirm the importance of evaluating the electrical features of the adopted NB-PLC signals carefully at an early design stage, especially if the smart street lighting networks have considerable size and complexity.

TABLE 1.4: Simulated peak-to-peak voltage amplitude of a 10 V_{PP} FSK signal in different points of a street lighting network, with the branches as in Figure 1.12.
(from [71] with permissions)

	1st node	11th node	17th node	20th node	23rd node	30th node
600 m line	8.05	2.68	1.4	1.03	0.82	0.6
600 m (with branches)	7.92	1.58	0.18	0.13	0.09	0.07
first branch (at 200 m)	-	1.7	1.17	1.09	-	-
second branch (at 340 m)	-	-	0.18	0.17	-	-
third branch (at 440 m)	-	-	-	-	0.09	-

Wake-up receiver simulation

Further simulation results are obtained by inserting the wake-up receiver in parallel to the PLM (downstream of the line coupling section). Figure 1.16 shows the PLC network with the addition of the WuRx.

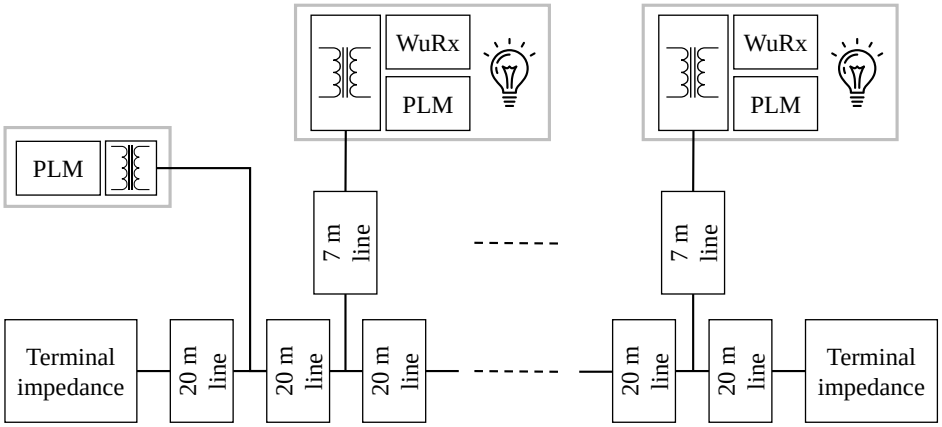

FIGURE 1.16: Example of a street lighting network as it was simulated with the addition of the wake-up receivers.

The simulation becomes complicated because of the nonlinear behavior of the voltage multiplier harvester of the WuRx, increasing the complexity of the simulation. Besides taking longer time to LTSpice to calculate the result, the signal propagates in the network in a slightly different way as the impedance of the WuRx affects signal transmission.

With the assumption that the WuRx circuitry is disconnected from the PLM when it is not needed (i.e. when the PLM is on), thus not impacting on the reception and

propagation of the signal. Three different cases can be considered, as explained in the following.

1. All the PLMs are OFF, that is the worst case scenario for the WuRx, because they are all listening and connected to the network.
2. All the PLM are ON except one, that is the addressed node. This is the best condition for the signal propagation and it works exactly as in the previous simulations.
3. In all the other possible combination, one or more nodes of the network are in stand-by conditions, listening for the wake-up signal. These nodes can be spread all over the network.

The simulated case refers to the worst conditions, with all the WuRx active and connected to the network. In a simple network with no branches, the wake-up signal is able to reach and wake-up a node at the distance of 200 m from the transmitter. Notice that this distance is more than doubled in the second case (all the PLM of the network are active). In fact, the application of the wake-up circuitry improves the overall system power consumption, but slightly reduces the functionality of the network. This trade-off has to be accepted to decrease the overall system power consumption. Some more considerations can help.
First of all, since transmitting at the maximum power is not always profitable. Thus, the best routing strategy in terms of transmitted power to reach a certain node was evaluated through simulations (using the network of Figure 1.16). In Table 1.5 some examples of the minimum energy required to reach a defined node in the network, with a single transmission operation (one hop) or with multiple retransmissions (multiple hops), are reported.

TABLE 1.5: Minimum energy associated to the wake-up operation of a node addressed with a defined number of retransmissions of the wake-up message (hops).

Node addressed	Minimum energy required				
10th	hops	1	2	5	10
	[J]	7	1.26	1.95	4.41
8th	hops	1	2	4	8
	[J]	2.28	0.76	1.25	2.83
6th	hops	1	2	3	6
	[J]	0.57	0.52	0.70	1.6

It is clear that transmitting at the maximum power to reach the farthest node is not a good choice, due to the different behavior of the WuRx at high gain signals. All the simulations are performed searching for the minimum power to reach the target node, splitting the transmitting power in chunks to be assigned to different nodes along the network for the retransmission of the message. An average transmitting power between 0.15 W to 0.25 W is the optimal one.

Considering that the PLM without the WuRx consumes around 1 W in standby conditions (i.e. listening), the proposed wake-up system is able to eliminate this overhead and, with a proper routing strategy, to minimize the energy needed to wake-up the nodes of the network, consuming even less power than a PLM in listening mode. The price, eventually, is the higher latency introduced by the wake-up operation.

1.4 A modern power system

Overview The electrical power grid is rapidly changing. Many heterogeneous energy sources are often integrated into the electric grid, exploiting the broader vision of energy systems, which may include heterogeneous energy sources. Some of the challenges that are currently under study are the integration of electric vehicles (EV) and Distributed Energy Resources (DER). These elements, spread all over the grid, are able to inject power, besides consuming it, causing a complex dynamic behavior of the grid that needs to be managed. Thus, one of the main features that has to be better handled in the future is the capability to manage bi-directional power flows safely and efficiently. This is very different from the traditional approach in which producers are clearly separated from consumers so that electricity flows in one direction only. Thus, consumers become *prosumers*, being able to produce and trade the energy with distribution system operators (DSO). To face these changes, many solutions have been proposed and they are commonly put inside the big container named Smart Grid.

Smart Grid The term Smart Grid (SG) was used for the first time in 2005 [72], and, even if a unique definition does not exists, it is agreed that the core advantage of the smart grid is the use of modern computation and communication technologies to improve the operation of the grid, enabling a number of advantages. In the SG, information communication technologies (ICT) help devices to interact with the aim of exchanging energy with higher flexibility, finally harmonizing the control of the grid with the end devices connected to it. The SG can be defined as a grid *"that incorporates information and communications technology into every aspect of*

electricity generation, delivery and consumption in order to: minimize environmental impact; enhance markets; improve service; reduce costs and improve efficiency" [73]. Now, it should be evident how the management of such a big and pervasive grid can pose many problems, such as the huge amount of data generated, creation of new communication links, cyber security issues and novel business models, among others.

From this picture it emerges the need for both:

1. a finer control of the grid, based on a deeper awareness of the state of the grid and proper state estimation algorithms,
2. new generation measurement instruments, able to provide valuable data to support the grid control.

Such a paradigm is already used for transmission grid operation and it is supported by *synchrophasor* measurements. The basics of synchrophasor measurement and the so-called phasor measurement units (PMUs) will be introduced in Chapter 2.

Grid control and operation Traditionally, power grid is controlled in a load-driven fashion, tuning large power plants to satisfy the grid power demand. In particular, the *transmission* grid transfers large power flows, and feeds the *distribution* systems linked to industrial or residential loads. The substations manage the power flows between different portions of the grid. Transmission and distribution systems are deeply different.
In particular the distribution systems exhibit the following features:

- the observability of the system may be problematic, due to the lower number of instruments on the grid;
- the R/X ratio of the lines is higher than in transmission systems;
- imbalances and harmonic distortions due to the presence of an increasing number of time-varying and non-linear loads are larger than at transmission level;
- the uncertainty on the line parameters is generally higher.

With the main assumption that large aggregated loads are more or less predictable, transmission system operators (TSOs) schedule power generation, while small deviations with respect to the scheduled power demand are compensated at run-time and generally do not create problems [74]. Power systems in the future are going to be significantly different. The current operating conditions are already changing towards a decentralized energy productions, because of the growing penetration of renewable resources in the grid, and, in general, of DERs. The DERs include

not only generating components (e.g. wind farms, photovoltaic systems), but storage also (e.g. plug-in electric cars can behave like storage elements), mainly connected to both medium-voltage (MV) and low-voltage (LV) levels. These elements, spread over the grid, make the problem of grid stability more complex. On the other hand, their integration in the grid operation is possible and very attractive as well, because of the enhanced flexibility and energy sustainability that the grid would achieve. With this final goal, the scientific community is active in producing also standards and communication protocols to manage distributed grid elements. For instance, the National Institute of Standard and Technology (NIST), in the context of the Smart Grid program, has developed a comprehensive *"Framework and Roadmap for Smart Grid Interoperability Standards"*, now at the 4.0 version [75]. Moreover, research activities are currently declined in a variety of ways, e.g. advanced sensors, algorithms and techniques to monitor the grid, load modeling, and others [76].
Estimating the state of the grid is particularly important when its operating conditions change. Only with a deep and accurate knowledge of its state is possible to finely control the grid [77]. A deep discussion on the grid state estimation (SE) techniques is out of the scope of this dissertation (comprehensive reviews already exist in the scientific literature [78]–[80]).

At the distribution level a number of additional problems may arise, e.g. due to the need to place PMUs or other measurement instruments in suitable locations to ensure grid observability or to improve state estimation accuracy.
The so called distribution system state estimation (DSSE) is growing, pushed by both industry and research sides. For instance, commercial programs have been developed by Eaton, Survalent, ETAP, OSI and Nexant [80]. In fact, the use of synchrophasor data for DSSE enables the integration of DERs [81], [82]. However, the high costs and infrastructural constraints limit the deployment of PMUs in distribution grids. This problem can be partially tackled with optimal placement strategies [83]–[86]. Moreover, the accuracy of such PMUs have to be higher than the ones deployed at transmission level. This is mainly due to the shorter line length and lower power flows that make the angle differences between voltage bus or line current phasors very small (i.e., in the order of a few mrad or less). Algorithms that achieve higher phase measurement accuracy have already been developed [87]–[90], but not many practical implementations have been released.

Even if PMUs are currently expensive, their price is expected to decrease. One good example is the µPMU [91] which was developed to meet the measurements requirements of distribution grids at a lower cost [92], [93]. A deeper and critical discussion on the existing PMU implementations is given in Chapter 5.

PMU benefits Nowadays, synchrophasors are employed almost exclusively to observe transmission systems [94]. However, the synchrophasor measurement benefits can be profited by distribution systems as well and in many ways: *(i)* improving reliability and resilience of the grid, *(ii)* producing more accurate models and enabling better planning and operations on the grid, *(iii)* enhancing the diagnostic and analysis operations, *(iv)* improving the maintenance and *(v)* ultimately producing environmental benefits. One important characteristic of PMU measurement data is the possibility to accurately time-stamp data, which permits to compare the measurements in different locations of the grid, at the same time.
Unlike smart meters, PMUs are able to produce high resolution voltage and currents profiles thanks to higher sampling rates. A smart meter, in fact, typically samples data at fractions of Hz (usually 0.277 mHz to 16.7 mHz), while a PMU works with sampling frequencies in the order of tens of kHz, reporting the results up to 50 times per second. As result, PMUs can be used for oscillation detection and, in general, event detection [91]. Power quality applications can be implemented as well [95], [96], e.g. voltage dips detection [97]. Besides real-time monitoring and protection applications, diagnosis applications, fault detection and localization are also possible with PMUs. For instance, islanding protection has already been studied in [98], [99].

Due to the high number of useful applications, the interest in installing PMUs is high, even for national institutions. For instance, NASPI is the North American Synchrophaosr Initiative [12] of the US Department of Energy, while VISOR is a real-time monitoring system for Great Britain power grid [100].
In 2014, the US Department of Energy published a study on the factors affecting PMU costs, identifying cost drivers such as: *(i)* communication, *(ii)* security, *(iii)* labor and *(iv)* equipment [101]. According to this study, *"the average overall cost per PMU (cost for procurement, installation, and commissioning) ranged from $40,000 to $180,000"*.

Exploiting the current IoT vision and the last electronic technologies, the current trend is the reduction of the cost with the goal of implementing PMUs extensively in the grid. For instance, the cost of a modern instrument is around $3500 [91] but it can be further reduced.

Once benefits and costs are identified, economic parameters such as benefits-to-costs ratio, net present value, and payback can be calculated. For instance, in 2016

[12] https://www.naspi.org/

it was calculated that a PMU network payback is 4 years and the benefits of synchrophasor technology (in the case at hand, i.e. in Great Britain) was estimated to range between 188 M£and 450 M£ [102].

CHAPTER 2

Phasor Measurement Units

In this chapter, the basic concepts and definitions for understanding the Phasor Measurement Units technology are introduced. The synchronized phasor model is presented as in the Standard IEEE C37.118-2011 and then the main PMU measurement requirements in different testing conditions are introduced.

2.1 Introduction

Phasor Measurement Units (PMU) enable grid operators to better control the grid, thanks to the more valuable data available, i.e. a large amount of synchronous data. The benefits gained by the PMU deployment are many, mainly: *(i)* improved reliability of the grid, *(ii)* the more accurate models enable better planning and operation, *(iii)* improved maintenance, *(iv)* environmental benefits due to the integration of many renewable resources in distribution grid.
It is not that easy though. PMU are complex instrument and the grid state estimation itself is a complex operation, leading the scientific community to put a considerable effort in designing measurement and control techniques for grid management, as previously explained in Section 1.4. In this chapter, the synchrophasor measurements and the principles of operations of a PMU are introduced together with the phasor model needed to define PMU operation and performance.

2.2 Synchrophasor Measurement

Traditional measurements in power systems are scalar, providing voltage and current by means of Root Mean Squared (RMS) values of AC signals. It is clear that the phase of an AC signal can be as important as the magnitude. Phase measurements can be used to estimate the state of the grid at a given time, at both transmission and distribution levels. Indeed, the technological development impose to improve the awareness of the state of the grid at the local level, to cope with the changes in the distribution systems mentioned before.

A local, direct and fast estimation of the phase is therefore needed, and PMUs are the devices that enable to extract not only the amplitude of the signal but also its phase, at times synchronized with a common time base (the coordinated universal time, i.e. UTC). In this way, different measurements can be coherently compared within a wide geographical area. Despite its apparently simple role, a PMU is a rather complex instrument. Starting from the transducer and the analog front end of the instrument, the design of a PMU require a particular attention because of the strict accuracy requirements needed. The fact that the measurement data have to be synchronized is another big challenge.

Phasor Measurement Units, like many other instruments, can be decomposed into few parts, namely: *(i)* an acquisition subsystem with an analog front-end and transducers, *(ii)* a digital signal processing subsystem, and *(iii)* a synchronization unit, timestamping the measurement results. Because of the strict time requirements, the acquisition part of the PMU needs a careful design, choosing a simultaneous sampling Analog-to-Digital converter (ADC), properly clocked by a UTC-locked signal and designing a filter with a flat pass-band and linear phase distortion. Transducers need also to be quite accurate, often reaching high costs, to ensure high linearity and to introduce as little disturbance as possible. As to signal processing, in this work the focus is on computationally inexpensive techniques, in order to implement PMUs on low-cost and simple embedded platforms. Other PMUs that can be found in the literature use high power and high performance FPGAs (Field Programmable Gate Array). It is somehow simpler to design a PMU with no constraint in terms of cost and performance, while using constrained resources turn out to be a challenging yet promising design approach. Also, for the synchronization process, the same consideration holds. High-end hardware and stable oscillators are expensive, while a careful design with less hardware resources is hard.

The use of PMU is already well established in power systems and the IEEE proposed two Standards for testing. These Standards, and in particular the IEEE Std.

C37.118.1-2011 [103], regulate the behavior of a PMU, imposing several performance limits, even if Distribution System Operators (DSOs) sometimes need even higher accuracy [91], [95], [96].

2.3 A basic phasor model

Given the usual representation of a sinusoidal waveform as:

$$\begin{aligned} x(t) &= X_m \cos(\omega t + \phi) \\ &= X_m \cos(\psi(t)) \end{aligned} \tag{2.1}$$

its phasor can be represented with the following:

$$\begin{aligned} \mathbf{X} &= \frac{X_m}{\sqrt{2}} e^{j\phi} \\ &= \frac{X_m}{\sqrt{2}} (\cos\phi + j \sin\phi) \end{aligned} \tag{2.2}$$

where $X_m/\sqrt{2}$ is the Root Mean Square (RMS) value of the waveform amplitude, ω is the angular frequency and ϕ is the phase, at a given reference time. Therefore, the *synchrophasor* of a sinusoidal signal is given by equation (2.2), and it is properly synchronized to the Coordinated Universal Time (UTC). Time synchronization is one key feature of a PMU. The phase is measured with respect to a cosine waveform so that the synchrophasor angle is 0 when the UTC second rollover occurs, i.e. at the maximum of a cosine function. An example waveform, with the respective phasor representation, is shown in Figure 2.1. The blue waveform is centered at the UTC second rollover, i.e. with phase zero, while the red one is shifted by -90 degree.

However, equation (2.1) does not fully describe the signal being acquired by a PMU as other disturbances are always present in power systems. One of the most important parameters affecting the synchrophasor measurement is the frequency deviation $\Delta f(t)$ from the nominal frequency f_0. Equation (2.1) thus changes, expressing $\omega = 2\pi f(t)$ with $f(t) = f_0 + \Delta f(t)$. Of course, the frequency shift results in a rotation of the synchrophasor with respect to the reference. If the frequency offset is constant, the phasor angle rotates. This effect can be obtained also in presence of

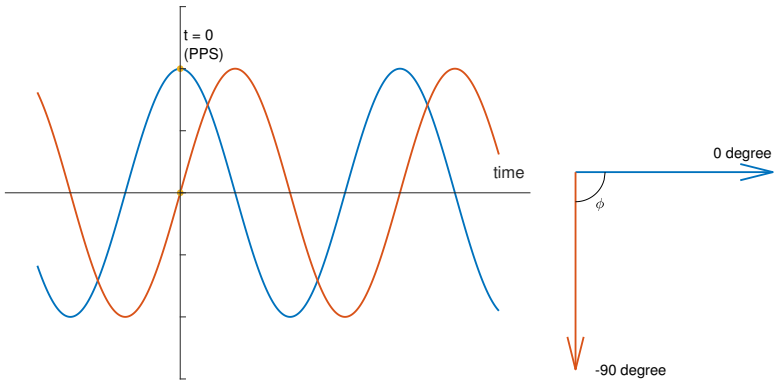

FIGURE 2.1: A couple of example waveforms, with a phase difference of 90 degrees and the respective phasor representation (with the same color).

incoherent sampling. This is just the first reason why the synchronization of PMUs must be taken into particular consideration.

Sampled waveform

The need for sampling the waveform obviously comes from the use of digital signal processing techniques to estimate waveform parameters. Moreover, phasor data are computed over a limited observation interval. The input analog signals are discretized using ADCs with a limited resolution and frequency. Usually, for a PMU, a 16-bit ADC with a sampling frequency of 10 kSample/s is enough.

The sampling frequency f_s is usually conveniently chosen as multiple of the nominal frequency f_0, resulting in $f_s = M \cdot f_0$ with $M \in \mathbb{N}$. It follows that the data records to be processed are split into observation intervals consisting of $N = C \cdot M$ samples, where C is the integer number of nominal power line cycles observed. Usually C ranges between 1 and 8. Note that in the presence of frequency deviation, the number of waveform cycles observed is no longer integer. It is convenient to define also the fractional off-nominal frequency deviation as δ, so that $f = f_0 \cdot (1 + \delta)$. The sampling frequency of a PMU has to be properly disciplined by a UTC clock. On the contrary, if the sampling frequency is not *syntonized* correctly, the effect is a wrong phase drift measurement, as shown in Figure 2.2. The same effect can be produced by the power line frequency deviation δ, but this drift is exactly what a PMU should measure.

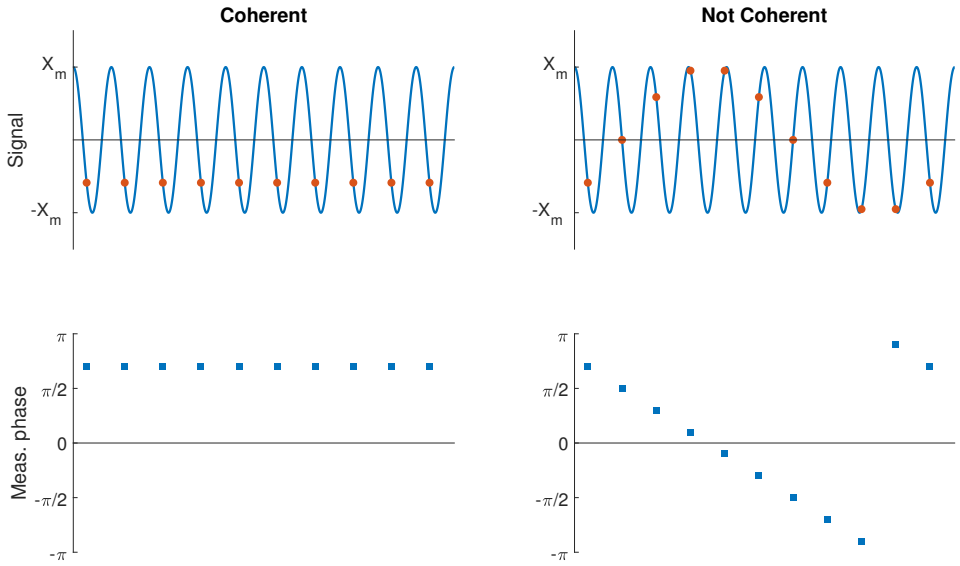

FIGURE 2.2: Difference between the coherent and not coherent operation of a PMU. These effects can be caused by both sampling frequency problems and frequency offset δ. The red dots indicate the time instant when the phasor is computed and, in the plots on the bottom, the result measured phase is shown.

2.4 The dynamic phasor model

Besides the first simple model introduced in the previous section, a more complete model can be built, including:

- Frequency deviation,
- Harmonics,
- Amplitude modulation,
- Phase modulation,
- Inter-harmonics,
- Wideband noise.

All of these disturbances are well defined in the standard C37.118.1-2011 [103], which reports the measurement compliance in specific testing conditions. Most of the scientific literature about synchrophasor measurement refer to these specifications for implementing new algorithms and software components for PMUs.

Starting from (2.1), it is possible to express some variables as a function of time, like:

$$x(t) = X(t)\cos[\varphi(t)] + \epsilon_h(t) + \eta(t) \tag{2.3}$$

where

$$\begin{aligned} X(t) &= X[1 + \epsilon_a(t)] \\ \varphi(t) &= 2\pi f(t)t + \epsilon_p(t) + \phi. \end{aligned}$$

The expressions above include multiple possible disturbances, i.e.:

- $\eta(t)$ models the total additive wideband noise; this is usually introduced by the analog front-end, synchronization circuitry, data acquisition and transducers;
- $\epsilon_h(t)$ is the contribution of harmonics and inter-harmonics components;
- $\epsilon_a(t)$ and $\epsilon_p(t)$ represent the amplitude and phase oscillations of the fundamental tone, and can both be modeled as cosine functions with their own amplitude, frequency and relative phase;
- $f(t)$ varies with respect to the nominal frequency f_0, as previously described.

The initial phase is ϕ, but, in the case of synchrophasor, the concept of phase depends on the UTC timestamp within a given observation interval. According to the standard, the phase $\phi(t_r)$ of the phasor is referenced to a given point of the observation interval (at time t_r), which is usually in the center of the observation interval. In the practice, a number of power line cycles are recorded and processed to estimate the phasor.

The aforementioned disturbances contributions included in the signal (2.3) can be expanded as follows.
The harmonics and inter-harmonics are modeled as:

$$\begin{aligned} \epsilon_h(t) = &\sum_h X_h \cos(2\pi h f(t)t + \phi_h) \\ &+ \sum_{h_i} X_{h_i} \cos(2\pi f_{h_i}(t)t + \phi_{h_i}) \end{aligned} \tag{2.4}$$

where h is the index of the harmonic component, while h_i is the inter-harmonic one. Note that for the latter, the frequency is not a multiple of the fundamental tone. The

standard prescribes strict limits for such interferences that are out of the bandwidth which depends on the PMU reporting rate, as it will be explained.

Dynamic amplitude and phase oscillations can be modeled as:

$$\begin{aligned} \epsilon_a(t) &= k_a \cos(2\pi d_a f(t)t + \phi_a) \\ \epsilon_p(t) &= k_p \cos(2\pi d_p f(t)t + \phi_p) \end{aligned} \tag{2.5}$$

where k_a and k_p are the amplitude and phase modulation levels, d_a and d_p are the fractional modulating frequencies with respect to the fundamental one, and ϕ_a or ϕ_p are the phases of the modulating signals.

The resulting model is fairly complex. Expanding all the equations can lead to a number of parameters which may strongly affect PMU measurements.

2.4.1 Synchrophasor measurement requirements

Together with the phasor defined previously (amplitude and phase), a PMU has to report also a couple of additional measurement, i.e. the Frequency and the Rate Of Change Of Frequency (ROCOF) of the fundamental tone [103].
Given the input signal as in equation (2.1), the frequency is defined as:

$$f(t) = \frac{1}{2\pi}\frac{\mathrm{d}\psi(t)}{\mathrm{d}t} = f_0 + \Delta f(t) \tag{2.6}$$

while the ROCOF is:

$$ROCOF(t) = \frac{\mathrm{d}f(t)}{\mathrm{d}t} = \frac{\mathrm{d}\Delta f(t)}{\mathrm{d}t}. \tag{2.7}$$

The measurement uncertainty has to lie within given limits, which are defined in the Standard and depend on the testing conditions. There are three parameters that define the performance of a PMU, namely the Total Vector Error (TVE), the Frequency Error (FE) and the ROCOF Error (RFE). While amplitude and phase error can be measured independently, the TVE is the relative difference between the *ideal* phasor and the measured one.
If the real and imaginary part of the phasor $\mathbf{X}$ are denoted as X_R and X_I respectively and if the respective measured values are denoted by the symbol $\hat{\cdot}$, the TVE at a specific time instant t_r is defined by:

$$TVE(t_r) = \sqrt{\frac{(\hat{X}_R(t_r) - X_R(t_r))^2 + (\hat{X}_I(t_r) - X_I(t_r))^2}{X_R(t_r)^2 + X_I(t_r)^2}} = \frac{|\hat{X}(t_r)e^{j\phi(t_r)} - X(t_r)e^{j\phi(t_r)}|}{|X(t_r)e^{j\phi(t_r)}|} \tag{2.8}$$

In the same way, the FE and RFE are defined as the difference between the actual frequency and the measured frequency:

$$FE(t_r) = |f(t_r) - \hat{f}(t_r)| \tag{2.9}$$

and similarly for the RFE:

$$RFE(t_r) = |ROCOF(t_r) - \widehat{ROCOF}(t_r)| \tag{2.10}$$

2.5 The IEEE Standard C37.118.1-2011

The history of PMU standards started in 1995, with the IEEE 1344-1995 document, that now is obsolete. Such a document do not report any requirements for PMU accuracy, rather the specifications on what a PMU is supposed to measure. The current standards are the IEEE Std. C37.118.1-2011 [103] and C37.118.2-2011 [104] edited in 2011. These two important documents define all the accuracy requirement that a PMU should meet. In particular, in the first part of the standard [103], after defining the phasor model, all the compliance tests and limits are explained. In 2014 some performance requirements were corrected in the IEEE Std. C37.118.1a Amendment [105].
Dually, the second part (i.e. the IEEE Std. C37.118.2-2011 [104]) provides the system overview of the measurement of phasors, defining the Phasor Data Concentrator (PDC) and the communication protocol for exchanging data between PMUs and PDC.

In the following, the accuracy limits and features of a PMU are described more in depth.

Performance classes

Two PMU classes are defined. The *M class* PMU is intended to be used for measurement application, that do not require high reporting rates but high accuracy. These PMUs usually relies on quite long observation intervals. On the other hand, *P class* PMUs are used when a fast response and reduced reporting latency are required, for instance in protection applications.
The error limits for such classes are different, because of different target applications, but this *"does not indicate that either class is adequate or required for a particular application"* [103].

Measurement reporting

PMUs have to report the measurement results at a specific rate, which usually is sub-multiple of the nominal power line frequency. The Standard prescribes some required rates, i.e. $F_R = 10,\ 25$ and 50 frames-per-second (fps) if the system frequency is 50 Hz, while $F_R = 10,\ 12,\ 20,\ 30$ and 60 fps for 60 Hz systems. Higher reporting rates are also encouraged. The reporting times shall be evenly spaced through the UTC second, numbering the frames from 0 to R-1, where R is a positive integer equal to the frames per second F_R.

The latency, intended as the time difference between the synchrophasor time-stamp and the time when the data becomes available at the output of the PMU, is also bounded by the Standard. For a P class instrument, the latency shall be below $2/F_R$ that means, for a 50 Hz reporting rate, a latency of 40 ms, i.e. 2 power line cycles. For a M class PMU instead, the constraint is less strict, i.e. $7/F_R$, which allows to use more cycles for each observation interval, thus usually incrementing the accuracy of the estimation.
The latency of measurement reporting is important for dynamic compliance testing because of the delay between an event occurring in the power system and the time that it is reported by the PMU. This latency is usually a function of the observation interval length (i.e. the number of cycles that the PMU uses for the synchrophasor computation).

2.5.1 Measurement compliance

The standard requires that the PMU maximum values of TVE, FE and RFE are below certain limits. Moreover, the Standard specifies some influence quantities that

have to be varied within certain limits. The worst case uncertainties requirements depend on the type of disturbing signals in input and are reported in the following.

Steady-state compliance

The test signals prescribed for the steady-state compliance are relatively simple to reproduce, as the characteristics of such signals do not change along the period of each test.
All the testing conditions for steady-state compliance are illustrated in Table 2.1. For some of them, the parameters to be changed depend on the reporting rate F_R. The corresponding table for the performance limits of the steady-state tests is shown in Table 2.2. Note that some limits are suspended by the last amendment of the standard in 2014 [105].

TABLE 2.1: Test conditions for both P and M class PMU, for the steady-state compliance reported in IEEE Std. C37.118.1 [103] considering the Amendment [105].

Influence quantity	**Test conditions**	
	P class	**M class**
Frequency deviation	$f_0 \pm 2$ Hz	$f_0 \pm 2$ Hz for $F_R \leq 10$ $f_0 \pm F_R/5$ for $10 < F_R < 25$ $f_0 \pm 5$ Hz for $F_R \geq 25$
Magnitude deviation - Voltage	80 to 120 %	10 to 120 %
Magnitude deviation - Current	10 to 200 %	10 to 200 %
Harmonic distortion	1 %, each up to 50th	10 %, each up to 50th
Out-of-band interference	none	10 % outside the passband, for $f_0 \pm 10\% \cdot F_R/2$ (only for $F_R \geq 10$)

The quantities to be varied for steady-state compliance are described in the following.

Signal frequency During this test the frequency is varied within up to ± 5 Hz with respect to the nominal frequency, while the other tone parameters (amplitude and phase) remain constant. Actually the frequency range depends on the reporting rate of the PMU, as in Table 2.1.

Signal magnitude The test signal amplitude is changed while phase and frequency are kept constant. The amplitude variation can be different with respect to voltage and current measurements and depend on their rated values. PMUs

TABLE 2.2: TVE, FE and RFE limits for both P and M class PMU, for the steady-state compliance tests of the IEEE Std. C37.118.1 [103] considering the Amendment [105]. The symbol (*) refers to the most stringent limit in the Standard, which depends on the reporting rate, while the "-" means that either the class does not require the specific performance or that the performance limit has been suspended.

Influence quantity	Class	TVE [%]	FE [Hz]	RFE [Hz/s]
Frequency deviation	P	1	0.005	0.4
	M	1	0.005	0.1
Magnitude deviation	P	1	-	-
	M	1	-	-
Harmonic distortion	P	1	0.005	0.4
	M	1	0.005 (*)	-
Out-of-band interference	P	-	-	-
	M	1.3	0.01	-

have to provide accurate results also in highly-stressed operating conditions, e.g. during faults.

Phase angle The measurement performed by the PMU need to be accurate within all the range $\pm\pi$. This test can be performed using a signal with a small off-nominal frequency (less than ± 0.25 Hz) which in turn produces a slowly varying phase angle.

Harmonic distortion For this test, the steady-state fundamental tone is corrupted by a single harmonic component up to the 50th with an amplitude of 1 % or 10 % of the fundamental for P class and M class, respectively. Using multiple harmonics at the same time could lead to measurement problems due to signal crest factor and rise time, even if in power systems such conditions can be found. For compliance testing, however, the harmonics are considered one at a time [106].

Out of band interference The out-of-band inter-harmonic interferences are considered the most critical disturbances for the PMU measurement and it is required only for M class compliance. For this test, the PMU is stimulated with a main frequency tone with a disturbance signal added at a frequency outside the passband, i.e. $|f - f_0| \geq F_R/2$. In particular, for a 50 fps reporting rate, the out-of-band signal is in the band $[10, 25] \cup [75, 100]$ Hz. The main tone signal frequency has also to be varied within ± 10 % of the Nyquist frequency of the reporting rate, i.e. between 47.5 Hz and 52.5 Hz for mains frequency of 50 Hz and reporting rate of 50 fps.

Dynamic compliance

In the case of dynamic compliance testing, the input signal amplitude, phase and frequency change over the observation interval.
The tests required consists of *(i)* amplitude and phase modulated signals, *(ii)* abrupt step changes in amplitude and phase, and *(iii)* frequency ramp.

Amplitude and phase modulation Amplitude and phase modulated (AM and PM) signals describe power swings that can be caused, for instance, by a lack of balance between power generation and loads. They are quite common and slow phenomena in power systems and usually appear simultaneously. However, the Standard prescribe separate tests (amended in the IEEE Std. C37.118.1a [105] in 2014), providing also a mathematical representation of amplitude and phase modulated signals, exactly as previously described in the dynamic phasor model (amplitude and phase modulations are expressed in equation (2.5)).
The fairly simple characteristics of the AM and PM disturbances for the test are reported in Table 2.3, while the error limits on Phasor, Frequency and ROCOF estimation are reported in Table 2.4. These error requirements are actually function of the reporting rate, while in the table only the most stringent limits are reported (corresponding to the slowest reporting rate).

TABLE 2.3: Test conditions for both P and M class PMU, for the AM and PM test signals for compliance reported in IEEE Std. C37.118.1 [103] considering the Amendment [105]. k_a and k_p are defined in equation (2.5).

Influence quantity	**Test conditions**	
	P class	**M class**
Amplitude modulation	$k_a = 0.1$ $k_p = 0$	$k_a = 0.1$ $k_p = 0$
Phase modulation	$k_a = 0$ $k_p = 0.1$	$k_a = 0$ $k_p = 0.1$
Modulating frequency	up to $F_R/10$	up to $F_R/5$

Frequency ramp This test usually returns similar results to those obtained considering static frequency deviations. However, having specific frequency rate characteristics, the PMU is stressed in a different way. The test conditions for the frequency ramp expects to simply produce a chirp waveform with a frequency rate of ± 1 Hz/s, and a frequency range inside the limits of frequency deviation for the respective class, i.e. ± 2 Hz for P Class and ± 5 Hz for M Class. The Standard prescribes to exclude the discontinuities at the beginning and at the end of the ramp,

TABLE 2.4: Compliance limits for both P and M class PMU, for the dynamic compliance tests (AM and PM modulation and frequency ramp) of the IEEE Std. C37.118.1 [103], considering the Amendment [105]. The symbol (*) refers to the most stringent limit in the standard, which depends on the reporting rate.

Influence quantity	Class	TVE [%]	FE [Hz]	RFE [Hz/s]
Amplitude and phase modulation	P	3	0.03 (*)	0.6 (*)
	M	3	0.12 (*)	2.3 (*)
Frequency ramp	P	1	0.01	0.4
	M	1	0.01	0.2

excluding the first samples during transitions. More details can be found in the Standard [103]. The TVE, FE and RFE limits are reported in Table 2.4.

Amplitude and phase step changes The step changes are usually produced by system faults or switching operations. However, PMUs are not expected to produce accurate results during these events and then the performance are evaluated on specific dynamic characteristics, i.e. the response time, delay time and overshoot/undershoot in measurements. For the step test, an abrupt transition between two steady-state signals happens at a specific time (with a step of 10 % in amplitude or 10° in phase). The step test indirectly includes the filtering performance of the PMU and can be considered different from the tests previously described, which are specific on the measurement accuracy only. The response time is defined as the *"time to transition between two steady-state measurements before and after a step change is applied to the input"*. In practice, this time interval is measured between the instant when the measurement overshoot exceeds the given TVE, FE or RFE limits and the time instant when such limits are met again steadly. The measurement delay time is just the delay between the step UTC time and the instant when the measured parameter value achieves half the step size. Also, the response time is considered on the UTC time base. The limits on such tests are illustrated in Table. 2.5. Note that most of the limits are expressed as a function of the reporting rate F_R.

2.6 Other relevant technical documents

The IEEE Standard on PMU have been developed by the working group WG-H11. At the time of writing, this commettee is preparing the newer version of the C37.118.1-2011, i.e. the IEC IEEE 60255-118-1 [107]. The newer version of the synchrophasor standard contains a nearly identical set of requirements and testing procedures. However, the definitions and procedures have been clarified and

TABLE 2.5: Test conditions for both P and M class PMU, for the step test of the IEEE Std. C37.118.1 [103], considering the Amendment [105]. The response time requirement is different for phasor, frequency and ROCOF measurements: here is reported only the phasor response time, which is the strictest.

Step specification	Class	Response time	Delay time	Overshoot
Magnitude step of $\pm 10\,\%$	P	$2/f_0$	$1/(4 \cdot F_R)$	$\pm 5\%$
	M	$7/F_R$	$1/(4 \cdot F_R)$	$\pm 10\%$
Phase step of $\pm \pi/18$	P	$2/f_0$	$1/(4 \cdot F_R)$	$\pm 5\%$
	M	$7/F_R$	$1/(4 \cdot F_R)$	$\pm 10\%$

simplified. It is more than 10 years that the WG-H11 is working on the problem of dynamic frequency and ROCOF measurements requirements [108].

Besides the standard on PMU measurement accuracy and data transfer, there are few more documents that can come handy when dealing with power system and PMU. The first one is the EN 50160:2010 [109]. This is the European standard for the *"Voltage Characteristics of Electricity Supplied by Public Electricity Networks"*, that reports the specifications of the voltage waveforms that the distribution system operators should meet. This is a regulation on the waveform usually present at the distribution level, and it is not mandatory for PMU compliance. However, it can be still used as an additional testing condition. In other words, the PMU measurement accuracy should not be significantly influenced by the disturbances usually present on the grid and expressed in the standard EN 50160.
Moreover, the C37.118.x Standard was originally conceived for PMUs operating at the transmission level, where power flows are usually higher and distortion levels lower. In the future, however, PMUs will be employed at the distribution level as well. Therefore, accuracy and robustness requirements could be higher.

In 2013, another document concerning PMUs was released by IEEE, namely the *"IEEE Guide for Synchronization, Calibration, Testing, and Installation of Phasor Measurement Units (PMUs) for Power System Protection and Control"* (C37.242-2013 [110]). This is a guide rather than a Standard. The C37.118 Standard is mentioned many times in this document, providing also details on the calibration and testing procedures.

The IEEE Std. C37.118.2-2011 [104] specifically deals with the *"method for exchange of synchronized phasor measurement data between power system equipment"*, and in the specific between the PMU and the so called phasor data concentrator (PDC). The PDC is the device able to collect all the measurement from a wide area network of PMUs, and store it for non-real-time applications. In case of real-time analysis of

the network status, the PDC has also to align data using the timestamp included in each PMU message. In this case PDCs have to provide proper latency and processing capabilities. The complete analysis of the protocol in all its messages and configurations is out of the scope of this dissertation, but it is worth noticing few interesting details. The phasor, frequency and ROCOF data is streamed along with many other data describing the status of the PMU, such as the lock state indication of the local clock and the so called time quality indication code. This can range from less than 100 ns to more than 10 ms, giving also an indirect estimation on the aiming accuracy. Another information exchanged is related to the presence of errors.
Some configuration messages can be exchanged to set the PMU as well. These messages give information, for instance, on the size of observation interval, the time base resolution, the number of channels and even some scaling factor for the computation of the output phasor.

Finally, it is important to mention the IEC 61850 in its many parts. Since 1980s, this standard was conceived to facilitate the interoperability between the so called Intelligent Electronic Devices (IEDs) to automate substations. IEC 61850 is widely accepted and used for wide area monitoring, protection and control (WAMPAC) applications. PMUs can be compliant with this standard as well. In particular, the IEC TR 61850-90-5 was developed as a secure and scalable alternative to the IEEE Std. C37.118.2 [108].
However, the latter provides neither specifications on the communication protocol to be used nor security requirements. The IEC 61850 instead provides the complete framework for harmonizing the substation automation, including PMUs. Moreover, PMU-to-PDC communication for wide area applications is also expected by this Standard.
Besides modeling the synchrophasor measurements into a logical node (called MMXU node) it provides specifications on how to encapsulate the application messages (UDP/IP multicast with IGMP v3 to avoid network flooding) and enhanced security by means of encryption keys (i.e. based on the RFC 3546-GDOI). Flexibility, security and scalability are indeed enabling factors for the future distribution system automation.

CHAPTER 3

A PMU testbed for algorithm characterization

In this chapter, a testbed based on the Fluke 6135A/PMUCAL is analyzed in order to identify and quantify the uncertainty contributions affecting estimation results in realistic scenarios. A metrological characterization is proposed in the following, properly supported by a noise propagation model, with the purpose not only to evaluate testbed uncertainty, but also to quantify the impact of the uncertainty of every component of the testbed on measurement results.

3.1 Introduction

It is clear that the accuracy of a PMU is crucial, but actual testing results are rarely disclosed by PMU producers, even if the compliance to the IEEE Standard is essential for correct grid state estimation. In 2014, NIST performed some tests on a number of commercial PMUs, finding that, out of the box, none of them was compliant to the IEEE Std. C37.118.1 and the Amendment C37.118.1a [111]. After some tuning operation on the firmware, a couple of PMUs were close to pass the test, while others did not. This is also a clear reason why the scientific community was, and still is, very active in producing new algorithms and phasor estimation techniques for PMUs.

Estimation algorithms for PMUs are usually tested on simulated environments. However, the performance of a PMU may depend on several uncertainty contributions affecting the acquisition and synchronization circuitry as well.
As a result, the accuracy of different estimation algorithms proposed in the scientific literature can be hardly compared when they are actually implemented in different real instruments and tested on the field.
At the same time, the need for a comprehensive characterization of PMUs with superior accuracy has become a research challenge for metrological institutes as well [112]. Indeed, several reference algorithms for calibrators [113], [114], flexible laboratory testbeds for PMU characterization [115]–[118], and even dedicated calibration systems [119], [120] have been developed over the last few years.
The most accurate existing testbeds are used for PMUs calibration and have been developed by national metrological institutes. The scientific literature reports some calibration testbeds for PMUs, developed at NIST [121] and at the Swiss Federal Institute of Metrology (METAS) [122]. Virginia Tech, where the first PMU was developed, also reported a PMU testing setup [123]. These setups are installed at their host location, connected to stable clock source such as reference atomic clocks. Some PMU characterization can be also automatized by means of commercial calibrator systems, such as the Fluke 6135A/PMUCAL.

Note that all these setups are mostly conceived to test a PMU in its entirety. However, for the sake of design optimization, a different testbed is needed to finely identify the influence of software and hardware parts on the overall measurement uncertainty. Usually such uncertainty contributions are grossly estimated and used for numerical simulations only. In fact, the relationship between PMU accuracy, algorithm performance and metrological characteristics of the hardware components is hard to predict or to simulate.

The testbed described in the following and developed in cooperation with the University of Campania *"L. Vanvitelli"* is purposely conceived to address this need, i.e., to implement and to test different PMU estimation algorithms under conditions that include not only the disturbances specified in the IEEE Std. C37.118.1-2011 and its Amendment IEEE C37.118.1a-2014, but also the effects of given (partially controllable) uncertainty contributions due to different hardware components. A thorough metrological characterization of the testbed, properly supported by a noise propagation model, can be used not only to evaluate the accuracy of the testbed, but also to quantify the impact of input waveform noise, transducers, data acquisition stage and synchronization circuitry on the uncertainty of the measurement results provided by the testbed, i.e. the estimates of synchrophasor magnitude, phase fundamental frequency and ROCOF returned by an algorithm under test (AUT).

FIGURE 3.1: Picture of the testbed.

3.2 Testbed description

The testbed (Figure 3.1) described in the following allows researchers to test and to compare different algorithms under the same operating conditions, i.e. including most disturbances that may appear in a real scenario. The stages of the testbed are described below [124].

- **Calibrator** The signals that stimulate the system under test are generated by a Fluke calibrator, namely the 6135A/PMUCAL . This is one of the most accurate signal generator able to generate three phase voltage and current signals up to 1 kV and 50 A RMS, respectively. The base accuracy of the signals generated by this instrument is listed in Table 3.1.
- **Transducers** A number of transducers can be found in the market. An international standard, the IEC 61869, regulate Instrument Transformers (ITs), which are key elements for power system monitoring. In one of the 15 parts

TABLE 3.1: Fluke 6135/PMUCAL specifications for the test under C37.118.1a [105].

	TVE [%]	FE [mHz]	RFE [Hz/s]
Steady-state	0.1	0.5	0.001
Dynamic, modulation	0.3	1	0.02
Dynamic, Frequency ramp	0.1	0.5	0.01

that compose the Standard, a clear classification of IT divides *"conventional"* ITs, which are inductive transformers, from Low-Power ITs (LPITs) which are *"intended to transmit a low power analog or digital information signal to measuring instruments"* and include voltage dividers, Rogowsky coils and Hall-effect transducers. In the testbed considered a couple of voltage and current transducers belonging to either groups are selected.

Voltage. The LEM CV3-1000 is a voltage transducer based on Hall-effect with a ratio of 100 V/V. The maximum input signal is 1000 VRMS and the rated accuracy is 0.2 %. The ABB TV2-380/100 is a instrument transformer with a ratio of 380/100, designed to work with a maximum input of 380 V RMS with a rated accuracy class of 0.5. Because of the different working principles, the linearity and the frequency response of these transducers are different.

Current. Again, two transducers are used, i.e. a Hall-effect LEM CT10-T sensor, with a rated accuracy of 0.1 % over 0-500 kHz with a maximum input RMS current of 10 A and a current instrument transformer SOCOMEC TO 58 500/5 of accuracy class 0.5.

- **Data acquisition modules** A PXI platform is used for acquisition, with a couple of NI PXIe-6124 modules. These data acquisition modules are able to sample a total of 8 waveforms simultaneously at a rate up to 4 MHz. For operation instead, the sampling rate is fixed at 10 kHz, as customary for commercial PMUs. Sampling frequency is a key parameter for PMU data processing, as a large sampling rate may harm the real-time operation of the PMU, while a too low sampling frequency, besides being problematic for harmonics rejection, may cause a larger impact of wideband quantization noise over a smaller Nyquist bandwidth. This delicate trade-off will be discussed later.

- **Time synchronization module** Another PXI module, namely the NI PXI-6683H, takes care of proper synchronization of the sampling operation to the UTC time base. This module disciplines the sampling clock so that the acquisition starts at the rollover of the UTC second. The time reference of the module can be a convenient external source, like GPS, IEEE 1588 [125] or IRIG-B [126]. In particular, the latter are solutions for clock distribution and are frequently adopted for substation automation because of the crucial role of time synchronization in power systems. IRIG-B is the Inter-range instrumentation group time code B, which is one of the most used standard to transmit time information in instruments. It was developed in 1998 by the Range Commander Council (RCC) of the US Army and then the IEEE Std. 1344 adopted it, extending its purpose. However, IEEE Std. 1588-2008, namely the *"Standard for a Precision Clock Synchronization Protocol for Networked Measurement and*

Control Systems" is more interesting nowadays, as it provides better performance, defining the Precision Time Protocol (PTP), which conveniently relies on Ethernet networks. The interest in using PTP is attested by the publication of a specific IEEE 1588 profile specifically conceived for power industries application, namely the IEEE Std. C37.238-2017 [127].
In the case at hand, the Fluke PMUCAL is synchronized through GPS and, in turn, it generates an IRIG-B synchronization signal used to synchronize the data acquisition module.

- **Processing module** The sampled data is processed by a NI PXIe-8135. This system is equipped with a quad-core Intel i7 processor running at 2.3 GHz and 16 GB of RAM.

- **Software** All the software for the Fluke PMUCAL control, data acquisition and data processing is based on LabVIEW. However, instead of replicating the estimation algorithm under tests (AUTs) in LabVIEW, they are implemented in C/C++ and instantiated in a LabVIEW virtual instrument using a wrapper function. This choice allows an easier AUT portability. Indeed, by using a Dynamic Link Library (DLL), the very same code can be compiled and can run on different processing platforms as well (e.g. on a PMU prototype) without the risk of introducing bugs due to the porting. The DLL is called from a *Call Library Function* node from the main LabVIEW program. The AUT functions require only few parameters, i.e. the record of data collected, a window function, the size of each data record and the nominal frequency. The outputs of the AUT are simply the magnitude, phase, frequency and ROCOF estimated for each data record. The time-stamp of each measure is then computed using the UTC reference from the synchronization module, i.e. the center of the observation interval.

3.3 Uncertainty analysis

The purpose of the testbed is to distinguish the inherent estimation errors of the AUT from the other uncertainty contributions. For this purpose such contributions need to be identified and modeled accurately. From a functional point of view, the entire chain is composed by a four multi-channel independent stages, i.e. the already described calibrator, the transducers, the data acquisition module and the synchronization module. Each one can introduce noise that then propagates and accumulates all the way through the chain, till reaching the processing module,

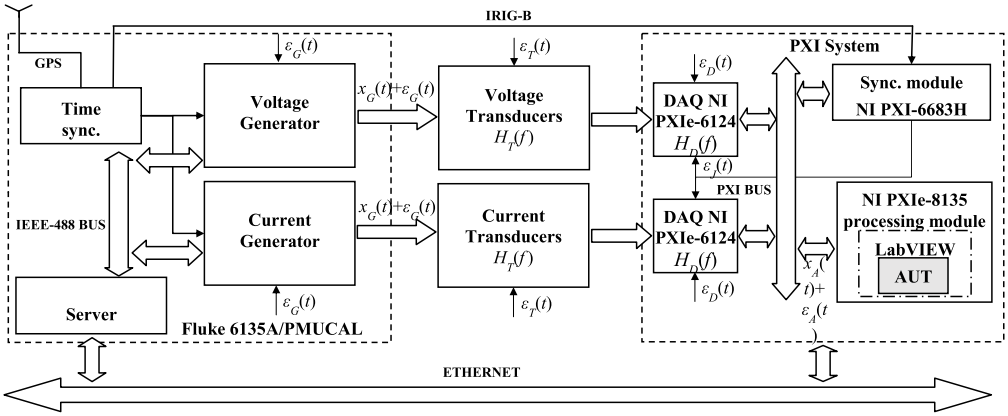

FIGURE 3.2: Block Diagram of the testbed.
(from [124] with permissions)

where the AUT runs. Hence an analysis is needed to identify how the noise introduced by each block affects the measurement results, eventually affecting the values of TVE, FE and RFE.

Assumptions

Given a sine wave $x_G(t)$ of given amplitude A and random initial phase, the frequency is chosen inside the interval $[45, 55]$ Hz and a number of known disturbances may be included if needed. In fact, harmonics, inter-harmonics, amplitude and phase modulations are generated by the calibrator along with $x_G(t)$, as prescribed by the standard C37.118.1.

All the random uncertainty contributions not included in $x_G(t)$ are modeled as stationary noise sources local to each stage. As stated before, such noise contributions propagate through the following blocks of the model. Because these disturbance are generated at different stages, they can be considered as uncorrelated and wide-sense stationary (WSS) random processes. In particular, $\varepsilon_G(t)$ is the specific noise on the calibrator, $\varepsilon_T(t)$ denotes the transducer one, $\varepsilon_D(t)$ refers to the data acquisition and finally $\varepsilon_J(t)$ is the synchronization jitter (in seconds). All these random noise contributions can be found in Figure 3.2 which shows the all the testbed modules discussed so far. The corresponding power spectral densities (PSD) in the following will be labeled with $\Phi(f)$ using the same subscripts referring to the specific element of the model. Note that these processes could include a DC component (or, in the case of $\varepsilon_J(t)$, a delay). Moreover, such processes can be considered as independent from the specific disturbances introduced for testing purpose. This assumption is confirmed by results also, as it will be shown later.

The frequency response $H_T(f)$ and $H_D(f)$ of transducer and data acquisition blocks respectively, are not perfectly flat in the passband. Possible systematic gain deviations of $|H_T(f)|$ and $|H_D(f)|$ at given frequencies can be compensated if they are known. More in general, magnitude response deviations can be regarded as uniformly distributed, i.e. $H_T \pm \Delta_T$ and $H_D \pm \Delta_D$, where H_T and H_D are the average magnitude response of $H_T(f)$ and $H_D(f)$ respectively and Δ_T and Δ_D are the corresponding worst-case deviations.

3.4 Noise propagation model

Based on the previous considerations, given that the signal processed by the AUT is $x_A(t)$, its PSD is:

$$S_{X_A}(f) = |H_D(f)\, H_T(f)|^2\, S_{X_G}(f) + \Phi_A(f) \tag{3.1}$$

where $S_{X_G}(f)$ is the PSD of $x_G(t)$ and $\Phi_A(f)$ is the PSD of the random process $\varepsilon_A(t)$ that is given by:

$$\Phi_A(f) = |H_D(f)H_T(f)|^2\Phi_G(f) + |H_D(f)|^2\Phi_T(f) + \Phi_D(f) + \Phi_S(f) \tag{3.2}$$

with $\Phi_G(f)$, $\Phi_T(f)$ and $\Phi_D(f)$ are the PSD of the random processes associated with the generator, transducer and data acquisition respectively; $\Phi_S(f)$ instead is the PSD of the cyclostationary process $\varepsilon_S(t)$ which results from the modulation of phase noise $\varepsilon_J(t)$.

In particular, since the random processes associated to each module are uncorrelated, and assuming that $\varepsilon_G(t)$, $\varepsilon_T(t)$, $\varepsilon_D(t)$ are negligible and $|\varepsilon_J(t)| \ll 1$, then $\sin[\varepsilon_J(t)] \approx \varepsilon_J(t)$ and $\cos[\varepsilon_J(t)] \approx 1$.
In this case, the testing signal can be modeled as:

$$\begin{aligned} x_G(t) &= A \sin[2\pi f_0 t + \phi + \varepsilon_J(t)] \\ &\approx A \sin(2\pi f_0 t + \phi) + \varepsilon_S(t) \end{aligned} \tag{3.3}$$

where

$$\varepsilon_S(t) = A\varepsilon_J(t)\cos(2\pi f_o t + \phi). \tag{3.4}$$

The autocorrelation of $\varepsilon_S(t)$ is a cyclostationary random process and its average autocorrelation function is:

$$R_S(t) = \frac{A^2}{2} R_J(t) \cos(2\pi f_0 t) \tag{3.5}$$

where $R_J(t)$ is the autocorrelation of $\varepsilon_J(t)$. Therefore, the PSD of the cyclostationary process $\varepsilon_S(t)$ is:

$$\Phi_S(f) \approx \frac{A^2 |H_D(f) H_T(f)|^2}{4} \left[\Phi_J(f - f_0) + \Phi_J(f + f_0)\right]. \tag{3.6}$$

Now that the PSDs of all noise contributions are defined, and recalling the expression of $\Phi_A(f)$ in equation (3.2), the RMS value of $\varepsilon_A(t)$ can be estimated as follows:

$$\hat{E}_A = \sqrt{\hat{H}_D^2 \, \hat{H}_T^2 \, \hat{E}_G^2 + \hat{H}_D^2 \, \hat{E}_T^2 + \hat{E}_D^2 + \hat{E}_S^2} \tag{3.7}$$

where $\hat{H}_T$ and $\hat{H}_D$ are the estimates of H_T and H_D respectively, and $\hat{E}_T$, $\hat{E}_D$, $\hat{E}_G$ and $\hat{E}_S$ are the estimated RMS values of the noise processes $\varepsilon_T(t)$, $\varepsilon_D(t)$, $\varepsilon_G(t)$ and $\varepsilon_S(t)$, respectively. In particular, the last one can be expressed as:

$$\hat{E}_S = \frac{\hat{A}}{\sqrt{2}} \hat{H}_D \, \hat{H}_T \, \hat{E}_J \tag{3.8}$$

highlighting that the RMS of $\varepsilon_S(t)$ depends on both the RMS value of $\varepsilon_J(t)$ and the estimated sinewave amplitude $\hat{A}$.

The combined standard uncertainty associated with (3.7) can be estimated using the well known law of propagation of uncertainties [128]. The estimates of the parameters $\hat{A}$, $\hat{E}_G$, $\hat{H}_T$, $\hat{H}_D$, $\hat{E}_T$ and $\hat{E}_D$ can be obtained from the data collected by a reference instrument, as described in Section 3.4.1. In this case, the measurement results can be considered as perfectly correlated. Therefore, the worst-case combined standard uncertainty associated with $\hat{E}_A$ is conservatively given by:

$$u(\hat{E}_A) = \sum_{i \in \{T,D\}} \left| \frac{\partial E_A}{\partial H_i} \right| u(\hat{H}_i) + \sum_{k \in \{G,T,D,S\}} \left| \frac{\partial E_A}{\partial E_k} \right| u(\hat{E}_k) \tag{3.9}$$

where $u(\cdot)$ is the standard uncertainty associated with the respective quantity.
As far as $u(\hat{E}_S)$ is concerned, while $\hat{A}$, $\hat{H}_T$, and $\hat{H}_D$ can be considered correlated, $\hat{E}_J$ (namely the RMS value of the phase noise on synchronization) is certainly uncorrelated to the others because a different measurement instrument (e.g. a frequency

counter) is typically used to measure the data needed to estimate $\hat{E}_J$. Thus the final combined standard uncertainty associated with $\hat{E}_S$ can be computed using [128]:

$$u(\hat{E}_S) = \frac{\hat{A}\hat{H}_T\hat{H}_D\hat{E}_J}{\sqrt{2}}\sqrt{\left[\left|\frac{u(\hat{A})}{\hat{A}}\right| + \left|\frac{u(\hat{H}_T)}{\hat{H}_T}\right| + \left|\frac{u(\hat{H}_D)}{\hat{H}_D}\right|\right]^2 + \frac{u^2(\hat{E}_J)}{\hat{E}_J^2}} \tag{3.10}$$

3.4.1 Noise model parameters

Summarizing, the parameters that need to be estimated are:

1. $\hat{A}$, the amplitude of the signal $x_G(t)$;
2. $\hat{E}_G$, the RMS value of the noise process $\varepsilon_G(t)$, associated with the calibrator;
3. $\hat{H}_T$, the estimation of the frequency response of the transducer;
4. $\hat{E}_T$, the RMS value of the noise process $\varepsilon_T(t)$, related to the transducer;
5. $\hat{H}_D$, the estimation of the frequency response of the data acquisition module;
6. $\hat{E}_D$, the RMS value of the noise process $\varepsilon_D(t)$, related to the data acquisition;
7. $\hat{E}_J$, the RMS value of the noise process $\varepsilon_J(t)$, associated with the synchronization process.

All these parameters are reported at the end of this section in Table 3.2, together with the other relevant metrological parameters discussed in the following.

Calibrator

The Fluke 6135A/PMUCAL is a flexible instrument, yet introduces its own uncertainty in the generated waveform. The model parameters $\hat{A}$ and $\hat{E}_G$ can be estimated using a four-parameters sinewave fitting (SF) test. This is a well-established technique to estimate, through least-square fitting, the amplitude, frequency, initial phase and DC offset of a digitized signal (a sinewave). The SF algorithm employed is described in the IEEE Std. 1057-2017 [129] and summarized in Appendix A as well. Of course, a very accurate digitizer is needed in this case, e.g. a Keysight 3458A reference digitizer, synchronized as the PXI 6683H module of the testbed.
A number of sinewaves with nominal RMS value of 230 V, random phase and frequency in the set $\{45, 47.5, 50, 52.5, 55\}$ Hz were generated to this purpose. The experiments can be affected by both systematic and random contributions, but, by

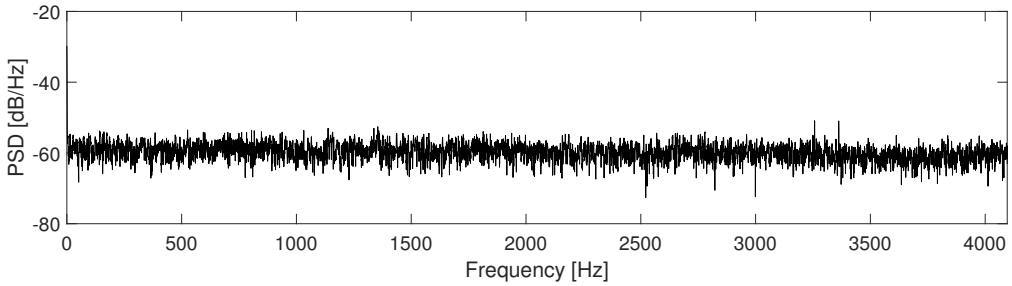

FIGURE 3.3: Estimated PSD $\Phi_G(f)$ of the noise introduced by the Fluke 6135A/PMUCAL.

averaging the results of independent experiments, the random contribution can be made negligible. The standard uncertainty can be computed using the classic *Type A* evaluation procedure [128]. For each experiment, the PSD $\Phi_G(f)$ is estimated by the modified periodogram (over 2^{14} points) of the independent residuals $\varepsilon_G(t)$. The periodogram relies on a Hann window. The average periodogram over 50 tests is shown in Figure 3.3. In Table 3.2 the RMS value is shown, together with other parameters of interests, namely the sine wave amplitude, the residual DC offset, the average Signal-to-Noise-and-Distortion ratio (SINAD) and the Spurious Free Dynamic Range (SFDR) [130]. These values result from the average over 50 tests. The respective standard uncertainty values, between one and two order of magnitude smaller, confirm that the experimental procedure is adequate. It is worth noticing that the residual DC offset and the average RMS value of the noise floor are significant, but reasonably small compared with the amplitude of the signal produced. Finally, the RMS value $\hat{E}_G$ is approximately proportional to the output signal level. The SINAD is between 65 and 67 dB (see also Table 3.2), which is in line with the values reported in the instrument documentation.

Transducers

Voltage and current transducers have to be calibrated to determine $\hat{H}_T$ and Δ_T. Using a procedure similar to the previous one, the mean magnitude and phase response of the transducers can be measured in the frequency interval of interest, i.e. from 45 Hz Hz to 55 Hz, with the transducer between the reference generator and the high accuracy digitizer. The RMS noise of the input signal is not negligible though. This must be compensated in order to properly compute $\hat{E}_T$, its standard uncertainty $u(\hat{E}_T)$ and the PSD $\Phi_T(f)$. The average magnitude response of the transducers are $\hat{H}_T = 0.0100\,\mathrm{V/V}$ and $0.009\,99\,\mathrm{V/V}$ for the LEM and the VT devices, respectively. The ripple amplitude is the same, i.e. $\Delta_T = \pm 1\,\mu\mathrm{V/V}$. The phase delay at 50 Hz is better for the LEM transducer, i.e. -0.5 mrad, than

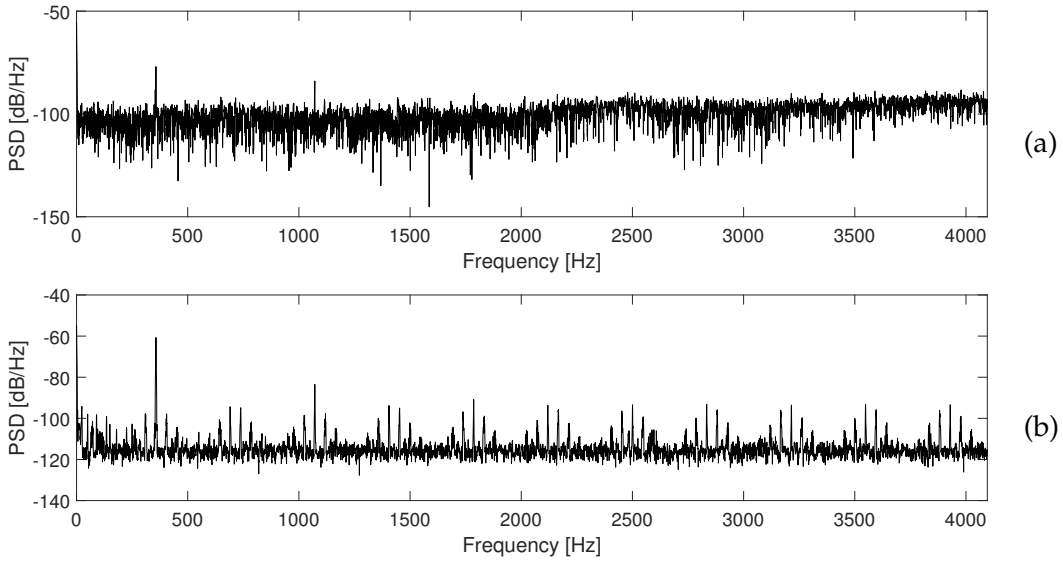

FIGURE 3.4: Estimated PSD $\Phi_T(f)$ of the noise introduced by transducer. Respectively, (a) is the LEM CV3-1000 and (b) the ABB TV2-380/100.

for the inductive transducer, i.e. -1.4 mrad [131], [132]. These delays have to be compensated at the output of the synchrophasor estimation algorithm. To determine $\hat{E}_T$, the same four-parameters sinewave fitting procedure was applied. Using the PMUCAL generator and two Keysight 3458A digitizers, 50 input and output waveforms were recorded and analyzed to determine the residuals of the fitting. The corresponding averaged periodogram of $\Phi_T(f)$ is shown in Figure 3.4 for both transducers. It is worth noting the difference between them. The inductive VT has intrinsically higher nonlinearity that causes a larger number of harmonic and spurious components. In the LEM transducer harmonics are not present, but there are two spurious components at 357 and 1071 Hz, probably caused by the internal electronics used to power the transducer. On the other hand, the noise floor of the VT is lower. Globally, the SINAD of the LEM transducer is 6 dB lower than the VT (reported in Table 3.2).

Data acquisition module

A similar approach has been used to evaluate the noise introduced by the data acquisition module NI PXIe-6124. The reference digitizer (Keysight 3458A) collects the data of a spectrally pure sinewave in parallel with the DAQ, synchronously. The magnitude and the phase response of the DAQ are computed together with the ripples in the frequency interval given by $[-f_s/2, f_s/2]$. The value of $\hat{E}_D$, the

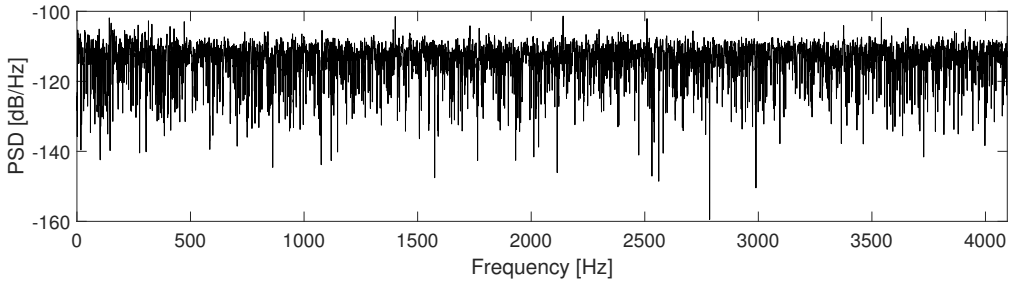

FIGURE 3.5: Estimated PSD $\Phi_D(f)$ of the noise introduced by the data acquisition module (NI PXIe-6124).

standard uncertainty $u(\hat{E}_D)$ and the estimated PSD $\Phi_D(f)$ are also computed using the same approach as in the transducer case. However, instead of using the PMUCAL, a NI PXIe-5422 is used for generating the input signals, as the noise floor and THD of this generator are lower than those of the PMUCAL at the voltage level of interest. As a result, $\hat{H}_D = 1.0005\,\mathrm{V/V}$ with ripples within $\Delta_D = \pm 60\,\mu\mathrm{V/V}$. The phase delay at 50 Hz is much smaller than 1 mrad, i.e. negligible, while the systematic deviation of the magnitude response (about $50\,\mu\mathrm{V/V}$) can be compensated in the processing module of the testbed. Again, the values of $\hat{E}_D$ and $u(\hat{E}_D)$ result from a four-parameters sine-fitting test, as explained before. The average periodogram of $\Phi_D(f)$ is shown in Figure 3.5. Note that this is quite flat and several dB lower than the transducers one. The average values of the SINAD and SFDR parameters are also quite low (reported in the Table 3.2).

Synchronization module

The synchronization noise, for the testbed under examination, is the result of two independent phenomena, i.e. the fluctuations of the sampling clock and the jitter affecting the start of data acquisition with respect to the waveform generation when the PMUCAL is triggered by a Pulse-Per-Second (PPS) signal. These two contribution have to be measured separately and contribute independently to the phase noise $\varepsilon_J(t)$.

A first group of experiments was performed with a Keysight 53230A frequency counter, to assess the performance of the sampling clock of the DAQ module. The result of this test show that the DAQ clock signal is stable over one day of observation, i.e. with a standard deviation of 30 ps that is close to the value reported in the instrument specifications. This noise has clearly a negligible impact on synchrophasor estimation. The second group of tests is needed to measure the delay between

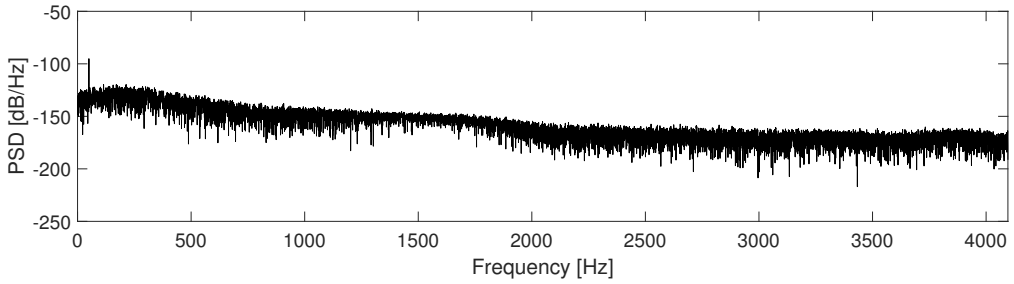

FIGURE 3.6: Estimated PSD $\Phi_S(f)$ of the noise introduced by the Synchronization module (NI PXI-6683H).

waveform generation and acquisition. Such a delay depends on the synchronization performed over an IRIG-B link. A Lecroy MDA810 digital storage oscilloscope was used to measure this delay for about 1 day. The time intervals recorded exhibit a normal distribution with a mean of 19 ns and a standard deviation of about 13 ns. However, sporadic variations of about ± 90 ns have been observed. Thus, the phase jitter $\varepsilon_J(t)$ is included in ± 30 µrad. The resulting RMS value is $\hat{E}_J \approx 7$ µrad, while $\hat{E}_S$, as given by equation (3.8), is about 16 µV. This has definitely a negligible impact on the overall testbed uncertainty. The average periodogram of $\Phi_S(f)$ is shown in Figure 3.6. This is well below the previous PSDs, except for a 50 Hz contribution due to the modulation of the 19 ns delay mentioned before. The slope of this plot is not flat due to nonstationary clock noises (e.g. flicker and random walk), which become evident only over long observation intervals [133].

Total noise

The experimental results associated with each stage of the testbed are reported in Table 3.2, along with the respective standard uncertainties. Using equations (3.7) and (3.8), the RMS of the overall noise floor of the testbed can be estimated.

When the LEM CV3-1000 transducer is used, $\hat{E}_A = 2.7$ mV with a combined standard uncertainty of $u(\hat{E}_A) = 0.1$ mV. The overall SINAD of the signal at the input of the processing module (after compensating the total DC offset) is about 60 dB.

When the inductive VT is used instead, $\hat{E}_A = 1.5$ mV with a combined standard uncertainty of $u(\hat{E}_A) = 0.7$ mV. The resulting SINAD instead is about 64 dB.

Note that the relative impact of noise contribution of the transducer is particularly large. In the case of the LEM transducer it is about 80 % of the total noise power, while for the inductive VT it is much lower (38 %). Conversely, in the former scenario, the noise of the calibrator accounts for 19 % of the total noise power, while in

TABLE 3.2: Measured value and standard uncertainties of the parameters of the model.

Stage	Device	Parameter	Measured value	Standard uncertainty
Generation stage	Fluke 6135A/PMUCAL	$\hat{A}$	325.295 V	1 mV
		DC offset	26 mV	3 mV
		SINAD	67 dB	0.02 dB
		SFDR	90 dB	0.2 dB
		$\hat{E}_G$	103 mV	0.9 mV
Transducer stage (voltage)	LEM CV3 1000	$\hat{H}_T$	0.0100 V/V	0.3 µV/V
		DC offset	-1.6 mV	0.2 mV
		SINAD	62 dB	0.02 dB
		SFDR	80 dB	0.2 dB
		$\hat{E}_T$	2.4 mV	0.1 mV
	Inductive VT	$\hat{H}_T$	0.00999 V/V	0.3 µV/V
		DC offset	0 V	30 µV
		SINAD	68 dB	0.2 dB
		SFDR	77 dB	0.3 dB
		$\hat{E}_T$	0.9 mV	0.02 mV
Data acquisition stage	NI PXIe-6124	$\hat{H}_D$	1.0005 V/V	35 µV/V
		DC offset	0.031 mV	0.002 mV
		SINAD	81 dB	0.2 dB
		SFDR	76 dB	0.1 dB
		$\hat{E}_D$	0.21 mV	0.01 mV
Synchronization stage	NI PXI-6683H	Sync. delay	19 ns	< 1 ns
		$\hat{E}_J$	7.0 µrad	< 1 µrad
		$\hat{E}_S$	16 µV	< 2 µV

the latter its contribution to total noise power is about 60 %. In both cases, the noise introduced by the DAQ and synchronization circuitry is negligible (less than 1 %).

Because of the better linearity and bandwidth of the LEM transducer, the setup with 60 dB is used in the next section for the comparison with the simulated results. Moreover, the main systematic contributions, namely the overall DC offset, the systematic magnitude and phase response deviations affecting $H_T(f)$ and $H_D(f)$ have been compensated.

3.5 Experimental results and validation

With the purpose of validating the testbed, three AUTs have been tested on it. These are:

- **IpD^{2}FT**, namely the Interpolated Dynamic Discrete Fourier Transform [134];
- **IpDFT**, which is the simpler Interpolated Discrete Fourier Transform [135];
- **TWLS**, that is weighted least square fitting of a Taylor's series expansion of the synchrophasor model [136].

All of them will be further explained in the following Chapter 4.

The purpose of this comparison is not to evaluate the difference between algorithm performances although they have a different behavior with respect to different disturbances. On the contrary, the different sensitivity with respect to different disturbances is exploited to perform a more complete analysis of the impact of the testbed on different algorithms.

The testbed measurements were compared with those obtained with a Monte Carlo simulator implemented in MATLAB, with the purpose of checking the consistency of results between the testbed and the model. To this aim, the three algorithms have been tested with both the simulated environment and testbed. TVE, FE and RFE are evaluated over 900 simulations, changing the noise sequence and the initial phase of the sinewave. The fundamental frequency of the input signal is also changed in the set $\{45, 47.5, 50, 52.5, 55\}$ Hz.
For the simulations, the SNR used to generate the input signal is 60 dB (in accordance to the analysis reported before, when the transducer LEM CV3-1000 is used). The amplitude of the waveform is set to the same value as the one collected by the DAQ, i.e. 2.3 , according to the scaling factor given by the transducer, i.e. $\hat{H}_T = 0.01$. All the AUTs make use of the same window function, i.e. a *Maximum Image Rejection* (MIR) window [134]; the purpose of this window is addressed in the next Chapter 4 and in the Appendix B. The length of the observation interval is set to $C = 4$ cycles and the sampling frequency to 8 kHz (close to the value used for the sinewave fitting algorithms described in the previous Section 3.4.1).

The maximum absolute differences between experiments and simulation-based values of TVE, FE and RFE associated with each algorithm, are shown in Table 3.3.

This table highlights the mismatch between the real experimental data and the simulations results based on the model. Such difference are on average 0.002 %, 0.17 mHz and 0.04 Hz/s, for TVE, FE and RFE, respectively. These small values

TABLE 3.3: Absolute values of the difference between the maximum TVe, FE and RFE measured using pure sinewaves of given frequency and the corresponding Monte Carlo simulation with a comparable noise floor (SNR = 60 dB).

Frequency	$\lvert\Delta TVE\rvert_{max}$ [%]			$\lvert\Delta FE\rvert_{max}$ [mHz]			$\lvert\Delta RFE\rvert_{max}$ [Hz/s]		
[Hz]	IpD^{2}FT	IpDFT	TWLS	IpD^{2}FT	IpDFT	TWLS	IpD^{2}FT	IpDFT	TWLS
45	0.001	0.002	0.004	0.33	0.26	0.05	0.03	0.02	0.01
47.5	0.003	0.003	0.001	0.13	0.13	0.17	0.05	0.04	0.08
50	0.000	0.000	0.000	0.09	0.22	0.30	0.01	0.06	0.08
52.5	0.003	0.003	0.001	0.28	0.07	0.31	0.01	0.03	0.09
57.5	0.002	0.002	0.001	0.04	0.03	0.09	0.01	0.04	0.07

highlight the good consistency between experimental results and simulation-based results. Therefore the noise propagation model can be considered correct.

In a second kind of tests, the simulations were repeated assuming a negligible noise floor (i.e. setting the SNR to 120 dB). The purpose of this comparison is to highlight the impact of the noise floor of the testbed on the algorithm estimation uncertainty with respect to ideal conditions.
The corresponding results are shown in Table 3.4. In this case, observe that the TVE, FE and RFE metrics are quite stable and independent of the algorithm considered, highlighting the accuracy limits of the testbed, i.e. the lower bound of TVE, FE and RFE are respectively 0.02 %, 1.5 mHz and 0.2 Hz/s. These values are particularly important for the evaluation of the testbed performance because they provide the minimum TVE, FE and RFE under which the differences between the corresponding values returned by different AUTs are no longer meaningful.
Notice that these values are slightly different from those shown in Table 3.1.

The last kind of tests has been performed to assess to what extent the noise propagation model and the analysis discussed so far are sensitive to additional disturbances not included in the model, but commonly present in power systems. Most of them are the one based on the conditions reported in the IEEE Std. C37.118.1 [103] and already discussed in Section 2.5.

Briefly, the input signals are:

- A sinewave with an offnominal frequency deviation of ± 5 Hz and an harmonic component (the 2nd and 3rd with amplitude of 10 % w.r.t. the fundamental tone);
- An amplitude modulated sinewave, with a 5 Hz modulating tone of amplitude equal to 10 % of the fundamental;

TABLE 3.4: Absolute values of the difference between the maximum TVe, FE and RFE measured using pure sinewaves of given frequency and the corresponding Monte Carlo simulation with a negligible noise floor (SNR = 120 dB).

Frequency	$\lvert\Delta\text{TVE}\rvert_{max}$ [%]			$\lvert\Delta\text{FE}\rvert_{max}$ [mHz]			$\lvert\Delta\text{RFE}\rvert_{max}$ [Hz/s]		
[Hz]	IpD^{2}FT	IpDFT	TWLS	IpD^{2}FT	IpDFT	TWLS	IpD^{2}FT	IpDFT	TWLS
45	0.02	0.01	0.02	1.35	1.27	1.85	0.19	0.25	0.28
47.5	0.02	0.02	0.02	1.46	1.38	1.74	0.16	0.28	0.24
50	0.02	0.02	0.02	1.47	1.74	1.63	0.14	0.27	0.23
52.5	0.02	0.02	0.02	1.44	1.41	1.86	0.16	0.28	0.25
57.5	0.02	0.02	0.02	1.31	1.23	1.93	0.20	0.24	0.29

- A phase modulated sinewave, with a 5 Hz modulating tone of amplitude equal to 1 rad;
- A nominal 50 Hz sinewave corrupted with a single out-of-band inter-harmonic at 24.9 Hz with amplitude equal to 10 % of the fundamental;
- A chirp waveform with constant frequency rate of ± 1 Hz/s from 45 Hz to 55 Hz;
- In addition to the previous testing conditions provided by the IEEE Stdandard C37.118.1, an additional testing condition is reported with the aim of reproducing more realistic operating conditions of PMUs in distribution systems. To this purpose, 25 harmonics components of different amplitude (i.e. between 0.5 % and 6.0 % of the fundamental one) have been added to $x_G(t)$ in order to have a Total Harmonic Distortion (THD) equal to 8 %, namely the maximum value specified in the EN Standard 50160:2010 both for LV and MV distribution systems.

The complete results are shown in Table 3.5. In all cases, the maximum values of TVE, FE and RFE over a record of 250 measurements are reported. The absolute values of the difference between measured and simulated values of TVE, FE and RFE are shortly denoted as $|\Delta|$ in the table. The average values of $|\Delta|$ are slightly higher than those shown in Table 3.3. They are 0.012 %, 0.6 mHz and 0.07 Hz/s for TVE, FE and RFE respectively, for all the algorithms. Therefore, the impact of the disturbance-specific and algorithmic-specific unmodeled phenomena is generally smaller than the impact of the overall noise floor of the testbed.

As final remark, the analysis highlights how transducers introduce the biggest share of random uncertainty contribution into the measurement chain. The accuracy limits of the testbed are TVE $\approx$ 0.02 %, FE $\approx$ 1.5 mHz and RFE $\approx$ 0.2 Hz/s.

TABLE 3.5: Maximum TVE, FE and RFE values obtained in different testing conditions for both simulated environment and testbed. The reported results belong to different AUTs (i.e. IpD^{2}FT, IpDFT and TWLS), with an observation interval $C = 4$ nominal power line cycles and reporting rate equal to 50 Hz.

Test type	**AUT**	**TVE [%]**			**FE [mHz]**			**RFE [Hz/s]**		
		Sim	Meas	$\lvert\Delta\rvert$	Sim	Meas	$\lvert\Delta\rvert$	Sim	Meas	$\lvert\Delta\rvert$
Freq. offset ($\pm$5 Hz) + 10% 2nd harmonic	IpD^{2}FT	0.25	0.24	0.00	5.00	4.55	0.45	5.0	5.0	0.0
	IpDFT	0.07	0.08	0.01	8.75	8.20	0.55	0.4	0.3	0.1
	TWLS	0.75	0.74	0.01	310.2	309.0	1.80	17.5	17.4	0.1
Freq. offset ($\pm$5 Hz) + 10% 3nd harmonic	IpD^{2}FT	0.03	0.03	0.00	1.97	1.49	0.49	0.3	0.3	0.0
	IpDFT	0.02	0.02	0.00	1.58	1.48	0.10	0.1	0.1	0.0
	TWLS	0.16	0.16	0.1	270.2	270.0	0.1	0.3	0.4	0.1
25 harmonics with THD = 8% in compliance with EN 50160	IpD^{2}FT	0.03	0.02	0.01	1.71	1.00	0.69	0.2	0.1	0.1
	IpDFT	0.02	0.01	0.01	1.91	1.21	0.70	0.1	0.2	0.1
	TWLS	0.04	0.03	0.01	3.11	2.75	0.36	0.7	0.6	0.1
AM (10% at 5 Hz)	IpD^{2}FT	0.05	0.06	0.01	1.63	1.23	0.40	0.2	0.1	0.1
	IpDFT	1.14	1.09	0.05	107.3	106.8	0.50	5.4	5.0	0.4
	TWLS	0.03	0.06	0.04	1.86	1.41	0.45	0.2	0.2	0.1
PM (0.1 rad at 5 Hz)	IpD^{2}FT	0.04	0.04	0.00	32.0	32.4	0.60	1.1	1.1	0.0
	IpDFT	1.02	1.03	0.01	33.5	32.8	0.70	15.8	16.2	0.4
	TWLS	0.04	0.04	0.00	28.8	28.0	0.80	1.0	0.9	0.1
10 % out-of-band inter-harmonic at 24.9 Hz	IpD^{2}FT	4.12	4.14	0.02	417.8	418.8	0.30	61.4	61.2	0.2
	IpDFT	0.26	0.26	0.00	782.6	782.8	0.20	39.1	39.1	0.0
	TWLS	5.82	5.82	0.00	565.2	564.1	1.10	103.5	103.6	0.1
Freq. ramp ($\pm$ 5 Hz at 1 Hz/s)	IpD^{2}FT	0.03	0.03	0.00	1.99	1.54	0.45	0.2	0.2	0.00
	IpDFT	0.02	0.08	0.06	1.55	1.85	0.30	0.1	0.2	0.1
	TWLS	0.13	0.14	0.02	260.0	259.8	1.20	0.4	0.3	0.1

CHAPTER 4

An estimation algorithm for low-cost PMUs

In this chapter, a lightweight algorithm suitable for low-cost PMUs, briefly called Tuned Lightweight Taylor-Fourier Transform (TLTFT), is presented. Before the description of the TLTFT, a brief overview of the two algorithms upon which the TLTFT relies (i.e. DFT and TFT) is given. Finally, the results of the major tests described in the IEEE Standard are presented.

4.1 Introduction

A variety of algorithms and different approaches can be used to estimate synchrophasor, frequency and ROCOF. The scientific production on this topic is evolving day by day, delivering new signal processing techniques and algorithms.

Generally speaking, the estimation algorithms can be divided into two simple groups, on the basis of the model they use, e.g. a *static* or *dynamic* phasor model. The first one is based on the assumption that the phasor does not change over the interval used to compute the measurement. The static phasor model is suitable for transmission systems, while for distribution systems PMUs need to be more accurate and must be able to track fast dynamic changes in amplitude and phase. Moreover, the model on which an algorithm relies can be complicated including other possible disturbances.

Another important distinction between estimation techniques is related to the domain in which the algorithm works, i.e. time or frequency domain. It must be noticed that fundamental frequency and ROCOF, depending on the specific algorithm, can be extrapolated with a postprocessing step (sometimes with a dedicated estimation procedure) or with the very same algorithm.

A complete review of all the algorithms that have been proposed in literature is out of scope. Among the algorithms based on the *static* phasor model, there are the classic windowed Discrete Fourier Transform (DFT) [137] and its Interpolated variant (IpDFT) [135]. The IEEE Standard also reports an estimation technique (in the Annex C [103]) based on the direct down-conversion of the digitized waveform followed by the low-pass filtering of the resulting in-phase and quadrature components. The performance of this technique, used by many PMU manufacturers, is strongly affected by the filters used [138]–[140].
In the group of algorithms based on the *dynamic* phasor model, an effective approach is to approximate the synchrophasor with its Taylor's series. The coefficients are then estimated through wighted least squares fitting [141], [142], finite difference equations [143] or in the frequency domain with a DFT [134]. The same approach can be extended to estimate the harmonics also through the so called Taylor-Fourier Transform (TFT) [144], [145]. Some of these techniques can be combined with digital filters, with other types of transformations (e.g. the Clarke Transformation), with custom windowing techniques or implemented with a Compressive Sensing (CS) approach [146]–[149].
Finally, other relevant estimation techniques are based on Kalman filters [150]–[152], Wavelet Transformation (WT) [153] and sine-fit (SF) [154], among others [155].

4.2 Algorithms overview

4.2.1 Reference synchrophasor estimation

In the Annex C of the IEEE Standard C37.118.1 [103] is described a signal processing scheme for synchrophasor estimation. This estimation technique is important as all the Standard is conceived for testing a PMU based on such a working principle. The phasor is extracted by demodulation of the collected waveform (which is down-converted to the baseband), followed by a low pass filtering stage. Both the acquisition and the quadrature oscillators are disciplined by a synchronized clock to obtain correct synchrophasors. The schematic is depicted in Figure 4.1. The phasor at the sample ith is therefore given by [103]:

$$X(i) = \frac{\sqrt{2}}{G} \sum_{k=-\Psi/2}^{\Psi/2} x[i+k]\, W[k]\, e^{[-j(i+k)2\pi f_0/f_s]} \tag{4.1}$$

where:

$$\begin{aligned} x[i] &= \text{sample of the waveform} \\ G &= \sum_{k=-\Psi/2}^{\Psi/2} W(k) \\ f_0 &= \text{nominal power system frequency} \\ f_s &= \text{sampling frequnecy} \\ \Psi &= \text{FIR filter order} \\ W[k] &= \text{low-pass filter coefficients} \end{aligned}$$

In the IEEE Standard, some hints on the design of the filter are given. The standard filter for the P class is a fixed-length two-cycles finite impulse response (FIR) filter with a triangular impulse response. Of course this introduces a delay that needs to be compensated as well as a magnitude distortion in off-nominal frequency conditions that needs to be corrected. For M class PMUs the standard expresses the need to *"attenuate by at least* 20 dB *signals that are above the Nyquist frequency for a given reporting rate"*. This filter affects the resulting phasor estimation in terms of immunity to disturbance such as noise or inter-harmonics, and reporting latency. A balanced trade-off between them should be achieved, with the result of being compliant to the Standard as well.

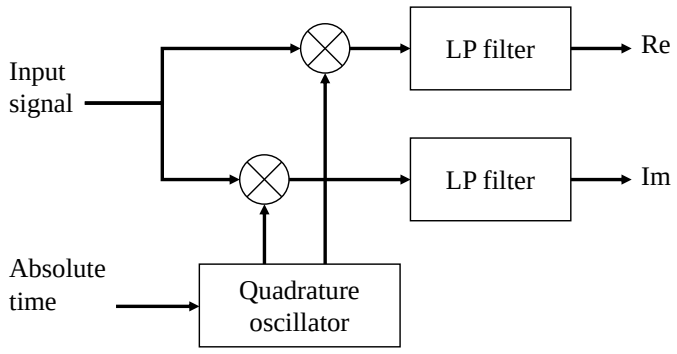

FIGURE 4.1: Phasor estimation via demodulation and filtering approach, as in the Annex of the standard C37.118.1 [103].

4.2.2 DFT-based algorithms

The Discrete Fourier Transform (DFT) is probably the simplest and fastest approach for phasor estimation. The accuracy of the DFT alone is usually not enough though.

Given a record of samples $x[n]$, the classic DFT is usually computed as:

$$X(\lambda) = \frac{1}{N} \sum_{n=-\frac{N-1}{2}}^{\frac{N-1}{2}} x[n]\, e^{-j2\pi \frac{\lambda n}{N}}, \quad \lambda = 0, \ldots, N-1 \tag{4.2}$$

where N is the number of samples of the interval (in this example N is odd, but can be extended to the even case easily) and λ denotes the frequency bin. The DFT algorithm works well in the case of coherent sampling, i.e. when the observation interval $x[n]$ includes an integer number of power line cycles C. Of course this is not the case of phasor measurement, because the frequency of the input signal $x[n]$ can differ. Therefore, the number of cycles that can be observed is not always integer. As a result, the accuracy of the estimator is often reduced by the scalopping loss of the rectangular window and by spectral leakage especially of the image component and of possible harmonics. Therefore, to mitigate these issues especially in presence of interfering signals, other window functions are used.
Thus, if a generic window $w[n]$ is used, the DFT formulation becomes:

$$X_w(\lambda) = \sum_{n=-\frac{N-1}{2}}^{\frac{N-1}{2}} w[n]\, x[n]\, e^{-j2\pi \frac{\lambda n}{N}}, \quad \lambda = 0, \ldots, N-1. \tag{4.3}$$

The joint combination of observation interval length and window type greatly helps to improve the accuracy of the DFT estimator [156]. Some windows have the effect of increasing the main lobe flatness or reducing the effect of harmonics, while other specific windows are designed to reduce the leakage of the image component. A deeper discussion on window functions is given in the Appendix B.

IpDFT

In addition to a proper window choice, the scalloping loss effect can be compensated by using the Interpolated DFT (IpDFT). The basic idea of the IpDFT is to compute a usual windowed DFT, finding, in addition, the fraction of frequency bin where the spectral peak of the main lobe is located [148], [157], [158].

Let P be the frequency bin corresponding to the magnitude spectrum peak of the fundamental component of x. As mentioned before, coherent sampling is achieved only in nominal conditions. Otherwise, it can be shown that [159]:

$$\alpha = \frac{|X(P+i)|}{|X(P-1+i)|} \tag{4.4}$$

where i is:

$$i = \begin{cases} 0 & |X(P-1)| \geq |X(P+1)| \\ 1 & |X(P-1)| < |X(P+1)| \vee P = 1. \end{cases} \tag{4.5}$$

Moreover, if the spectral leakage of the image component has a negligible impact on the fundamental tone, the following approximate expression holds [135]:

$$\alpha \approx \frac{|W(i-P\delta)|}{|W(-1+i-P\delta)|} \tag{4.6}$$

where $W(\cdot)$ is the discrete time Fourier Transform of the window w and δ is the fractional frequency deviation, as previously introduced.

Thus, δ can be estimated by inverting equation (4.6):

$$\hat{\delta} = g\left(\alpha, i\right). \tag{4.7}$$

The function $g(\cdot)$ depends on the adopted window w and can be determined *a priori*. Some analytical formulation of $g(\cdot)$ can be found in the literature for Maximum Side-lobe Decay (MSD) windows [159], while some approximated solutions (e.g. for Maximum Image Rejection windows) are also reported in [160] .

Finally, for the IpDFT, the phasor is given by:

$$\mathbf{X} = \frac{|X(P)|}{|W(-\hat{\delta})|} e^{-j\angle X(P)} \tag{4.8}$$

4.2.3 TFT-based alorithms

An effective approach for synchrophasor estimation is based on its Taylor's series approximation. The Taylor-Fourier Transform (TFT) relies on the Taylor's series of the fundamental phasor and those of the harmonics till a predefined order H [144].

The coefficients of this series, truncated to a predefined order K, can be estimated using a Least Square approximation (LS) or other methods (e.g. IpD^{2}FT [134]). One of the main advantages of this approach is the adoption of a dynamic phasor model to represent the input signal, that is (from section 2.4):

$$\begin{aligned} x(t) &= \sum_{h=0}^{H} X_h(t)\, \cos\left(2\pi h f_0 t + \varphi_h(t)\right) \\ &= \sum_{h=0}^{H} c_h(t) e^{j2\pi h f_0 t} \end{aligned} \tag{4.9}$$

where $c_h(t) = X_h(t)e^{j\varphi_h(t)}$ can be seen as the complex phasor of the harmonic h [144]. In static conditions, c_h is constant and the DFT can get accurate estimation, but under dynamic oscillations, signal amplitude and phase may change quite rapidly, causing inaccuracies of any algorithm based on the static model.

Expressing the Taylor's series of $c_h(t)$:

$$c_h(t) \approx \sum_{k=0}^{K} c_h^{(k)} \frac{t^k}{k!} \tag{4.10}$$

the dynamic signal model in equation 4.9 can be rewritten as:

$$x(t) \approx \sum_{h=0}^{H} \sum_{k=0}^{K} c_h^{(k)} \frac{t^k}{k!} e^{j2\pi h f_0 t} \tag{4.11}$$

where $c_h^{(k)}$ denotes the k-th derivative of $c_h(t)$ at a given reference time t_r [145]. Rearranging equation (4.11) in a discrete form, considering T as the sampling period, it results that:

$$x(n) = \sum_{h=0}^{H} \sum_{k=0}^{K} X_{(k,h)}\, (nT)^k\, e^{j2\pi h f_0 nT} \tag{4.12}$$

where the (k,h)-th coefficient of the Taylor's series is:

$$X_{(k,h)} = \frac{1}{k!(M \cdot f_0)^k} \left. \frac{d^k c_h(t)}{dt^k} \right|_{t_r} \tag{4.13}$$

where $h = 1, \ldots, H$, $k = 0, \ldots, K$, M represents the number of samples in each power line cycle and f_0 the nominal frequency, as previously introduced. It can be easily shown that $M \cdot f_0 = f_s$, namely, the nominal sampling frequency.

If the samples collected in the r-th observation interval are included in a $1 \times N$ column vector $\mathbf{x}_r$, the expression of (4.12) can be rearranged in a matrix form as:

$$\mathbf{x}_r = \mathcal{M}\,\mathbf{X}_r$$

where $\mathcal{M}$ is a $N \times 2 \cdot (K+1)(2H+1)$ complex valued matrix whose elements depends on the model, i.e. the number of harmonics, the length of observation interval and the number of Taylor's series terms considered [144].
Thus, the synchrophasor coefficients result from:

$$\hat{\mathbf{X}}_r = \left(\mathcal{M}^\dagger \mathcal{M}\right)^{-1} \mathcal{M}^\dagger \mathbf{x}_r \tag{4.14}$$

In [141], the same approach is used in the WLS sense, using a proper weighting function, (i.e. the coefficients of a window $v(\cdot)$) which can be used to build an $N \times N$ diagonal matrix $V = \mathrm{diag}\{v(0), \ldots, v(N-1)\}$. The previous equation (4.14) thus becomes:

$$\hat{\mathbf{X}}_r = 2\left(\mathcal{M}^\dagger V^\dagger V \mathcal{M}\right)^{-1} \mathcal{M}^\dagger V^\dagger V \mathbf{x_r} \tag{4.15}$$

Once the elements of $\hat{\mathbf{X}}_r$ are computed, the phasor (and its derivatives) at time t_r are given by [161]:

$$\begin{aligned}
\hat{X}_r &= |\hat{X}_{(0,1)}| \\
\hat{\varphi}_r &= \angle \hat{X}_{(0,1)} \\
\hat{X}'_r &= 2\,\Re\{\hat{X}_{(1,1)}\, e^{-j\hat{\varphi}_r}\} \\
\hat{\varphi}'_r &= \frac{2}{\hat{X}_r}\,\Im\{\hat{X}_{(1,1)}\, e^{-j\hat{\varphi}_r}\} \\
\hat{X}''_r &= 4\,\Re\{\hat{X}_{(2,1)}\, e^{-j\hat{\varphi}_r}\} + \hat{X}_r(\hat{\varphi}'_r)^2 \\
\hat{\varphi}''_r &= \frac{4\,\Im\{\hat{X}_{(2,1)}\, e^{-j\hat{\varphi}_r}\} - 2\,\hat{X}_r\hat{\varphi}'_r}{\hat{X}_r}
\end{aligned} \tag{4.16}$$

4.3 TLTFT algorithm

The Tuned Lightweight Taylor-Fourier Transform algorithm (TLTFT) is a combination of the aforementioned TFT algorithm with a preliminary IpDFT stage, all implemented in a computationally efficient way. The algorithm is lightweight in the sense that it is specifically tuned to run on low-cost hardware (in the specific, on a BeagleBone Black board) meeting the performance requirements of the IEEE Standard with a limited computational burden. The TLTFT aims to achieve a good trade-off between estimation accuracy, robustness to unmodeled disturbances and processing time. Unlike the TFT, the coefficients of the system matrix $\mathcal{M}$ are tuned at run-time to compensate possible static off-nominal frequency deviations. The idea of tuning the coefficients of the TFT is not completely new. Castello *et al.* [142] already proposed a similar solution. However, the first stage of the TLTFT is computationally lighter, it is not iterative and returns a very accurate frequency estimation, given that the other disturbances are correctly filtered out. The TFT stage finally is tuned for minimizing the complexity of the model, while preserving accuracy with respect to the length of the observation window. The implementation is also optimized as it relies on a real-valued formulation of the TFT algorithm.

In the following, the algorithm is illustrated in its two core parts: the IpDFT-based frequency deviation estimation and the TFT-based synchrophasor estimation. More details on the actual implementation will be provided in the next chapter.

4.3.1 Frequency deviation estimation

The frequency deviation δ is estimated through the IpDFT. This first step is required in order to compensate for the off-nominal frequency deviation. A Maximum Image Rejection (MIR) window is used to mitigate the effect of the spectral leakage from the image component of the fundamental, which is one of the inherent sources of uncertainty of IpDFT. In addition, a preliminary filter is used to reduce the effect of other disturbances, e.g. harmonics, that could have a detrimental impact on the fundamental frequency estimation.

The filter implemented is a band pass filter, centered at 50 Hz, with a passband of ± 5 Hz, so that frequency changes between 45 and 55 Hz can be accurately tracked, as the IEEE Standard requires [103]. The stop-band specifications are chosen to filter the harmonics as much as possible while relaxing the transition bandwidth. The attenuation in the stopband is set to 34 dB, while ripple magnitude in the passband is -0.009 dB. For practical implementation needs, i.e. the convenience of using a

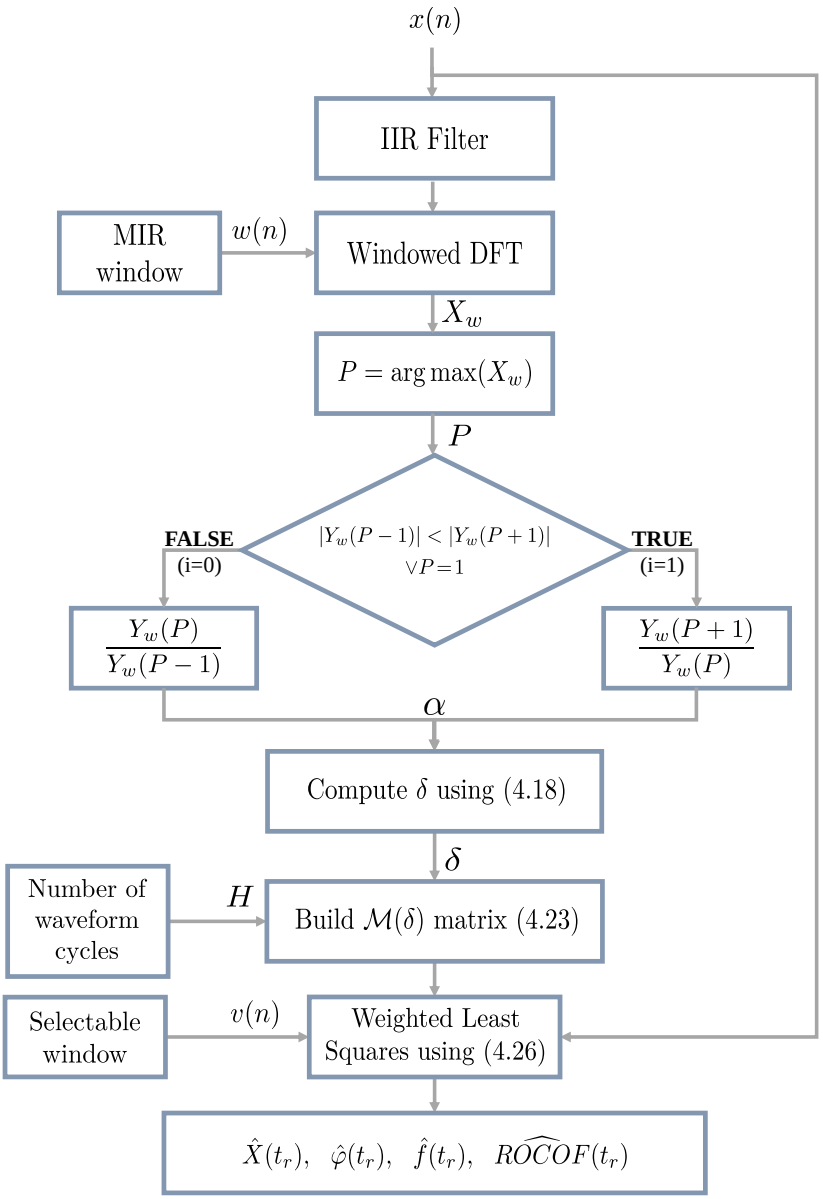

FIGURE 4.2: Flow chart of the TLTFT estimation algorithm.

filter with a fixed order and the same computational burden at different sampling frequencies, an Infinite Impulse Response (IIR) elliptic filter is used. Of course, the coefficients of the filter change, but its realization remains the same, i.e. a Canonical Form II, which requires a little number of multiply and accumulation operations. Due to the low order of the filter, no numerical instability occurs. In the case at hand, the filter order is 6, that is much lower than the order of a Finite Impulse Response (FIR) filter with similar specifications. The main problem of IIR (and particularly elliptic filters) is the in-band phase distortion. However, the proposed filter is used only to clean up the signal before the frequency deviation δ is estimated by the windowed IpDFT, as can be seen in Figure 4.2. Therefore, the phase distortion introduced by the filter is not a problem, while for the upcoming TFT algorithm, no filter is applied.

As briefly discussed in Section 4.2.2, assuming that equation (4.6) holds (i.e. the spectral leakage is negligible), the frequency offset δ (expressed in bins) can be estimated.

If the MIR window is used, then the equation:

$$\alpha = \frac{|X_w(P+i)|}{|X_w(P-1+i)|} \approx \frac{|W(i-P\delta)|}{|W(-1+i-P\delta)|} \tag{4.17}$$

can be solved to estimate $\hat{\delta}$ as follows [160]:

$$\hat{\delta} = \begin{cases} \frac{1}{C}\left[P - C + 2\sqrt{p}\cos\left(\frac{\pi}{3}+\frac{\psi}{3}\right) - \frac{\alpha+2}{3(\alpha+1)}\right] & i=0 \\ \frac{1}{C}\left[P - C - 2\sqrt{p}\cos\left(\frac{\pi}{3}+\frac{\psi}{3}\right) + \frac{\alpha+2}{3(\alpha+1)}\right] & i=1 \end{cases} \tag{4.18}$$

where

$$p = \frac{12C^2+4}{9} - \frac{\alpha}{9(\alpha+1)^2}$$

and

$$\psi = \cos^{-1}\left(\frac{|u|}{p\sqrt{p}}\right), \quad \text{with } u = \frac{(\alpha-1)[(\alpha+1)^2(144C^2-16)+\alpha]}{54(\alpha+1)^3}.$$

The value of $\hat{\delta}$ given by (4.18) can be eventually used to tune the coefficients of the TFT.

4.3.2 TFT and synchrophasor estimation

The TFT algorithm, previously described in section 4.2.3, is based on the Taylor's series of the fundamental tone and a predefined number of harmonics H. The waveform model obtained is then fitted using a WLS approach. The TFT has been enhanced in order to be suitable for an embedded implementation. In particular, complexity reduction is obtained in two ways. First, the algorithm makes use only of real-valued operations, rather than complex ones. Second, the number of harmonics included in the waveform model is also chosen in an adaptive way, as a function of the length of the observation interval. The rationale of this choice is that the impact of harmonics on synchrophaosor estimation tends to decrease as the number of observed cycles C grows [162].

Starting from a model similar to the one introduced in equation (2.3), including H harmonics in ϵ_h, but neglecting wideband noise contributions η, the signal $x(n)$ can be rewritten as:

$$x(n) = \sum_{h=1}^{H} X_R^{(h)} \cos\left(2\pi h \frac{f}{f_s} n\right) - X_I^{(h)} \sin\left(2\pi h \frac{f}{f_s} n\right) \tag{4.19}$$

where, again, $r - \frac{N-1}{2} \leq r + n \leq \frac{N-1}{2}$ (for N odd), $f = f_0 \cdot (1+\delta)$, $X_R^{(h)}$ and $X_I^{(h)}$ are the real and imaginary parts of the phasor of the h-th harmonic at reference time t_r, respectively, i.e. $\bar{X}^{(h)} = X_R^{(h)} + jX_I^{(h)}$. Of course, $\bar{X}^{(1)} = \bar{X}$ is the synchrophasor of the fundamental.

As usual, the Taylor's series of $X_R^{(h)}$ and $X_I^{(h)}$ truncated to term K_h can be written as:

$$X_R^{(h)} \approx \sum_{k=1}^{K_h} X_{R_k}^{(h)} (n-r)^k \quad \text{and} \quad X_I^{(h)} \approx \sum_{k=1}^{K_h} X_{I_k}^{(h)} (n-r)^k \tag{4.20}$$

where

$$X_{R_k}^{(h)} = \frac{1}{k!(Mf_0)^k} \frac{d^k X_R^{(h)}}{dt^k}\bigg|_{t_r} \quad \text{and} \quad X_{I_k}^{(h)} = \frac{1}{k!(Mf_0)^k} \frac{d^k X_I^{(h)}}{dt^k}\bigg|_{t_r} \tag{4.21}$$

are the Taylor's series coefficients of $X_R^{(h)}$ and $X_I^{(h)}$, respectively, computed at time t_r.

Again, after some algebraic steps [144], it can be shown that the sequence of values $x(n)$ can be expressed in matrix form as:

$$\mathbf{x}_r = \mathcal{M}(\delta)\mathbf{X}_r \tag{4.22}$$

where $\mathbf{x}_r$ is a $1 \times N$ vector comprising the samples collected in the r-th observation interval and $\mathbf{X}_r = [\mathbf{X}_r^{(1)}, \ldots, \mathbf{X}_r^{(H)}]^T$ are the coefficients of the Taoylor's series properly rearranged. In particular, as in the traditional formulation of the TFT, but using the real and imaginary parts separately, it follows that:

$$\mathbf{X}_r^{(h)} = [X_{R_{K_h}}^{(h)}, \ldots, X_{R_0}^{(h)}, -X_{I_0}^{(h)}, \ldots, -X_{I_{K_h}}^{(h)}]^T \quad \text{for} \quad h = 1, \ldots, H$$

Therefore $\mathcal{M}(\delta)$ is a $N \times 2 \cdot (K_1 + ... + K_H + H)$ real-valued matrix, whose elements for $h = 1, \ldots, H$ are functions of δ.
Of course, $\mathcal{M}(\delta)$ can be written as:

$$\mathcal{M}(\delta) = \begin{bmatrix} A_{K_1}^{(1)}(\delta) & B_{K_1}^{(1)}(\delta) & \cdots & A_{K_H}^{(H)}(\delta) & B_{K_H}^{(H)}(\delta) \\ \Gamma_{K_1}^{(1)}(\delta) & \Delta_{K_1}^{(1)}(\delta) & \cdots & \Gamma_{K_H}^{(H)}(\delta) & \Delta_{K_H}^{(H)}(\delta) \end{bmatrix} \tag{4.23}$$

which is equivalent to the complex-valued counterpart of matrix $\mathcal{M}$ introduced in Section 4.2.3. In particular, in this case the terms of the matrix $\mathcal{M}(\delta)$ are real-valued and explicitly depend on the static offnominal frequency deviation δ. They are defined as follows:

$$\begin{aligned} \left(A_{K_h}^{(h)}(\delta)\right)_{lq} &= \left(l - \frac{N+1}{2}\right)^{K_h - q} \cos\left[\frac{2\pi h(1+\delta)}{M}\left(\frac{N+1}{2} - l\right)\right], \\ \left(B_{K_h}^{(h)}(\delta)\right)_{lq} &= -\left(l - \frac{N+1}{2}\right)^{q} \sin\left[\frac{2\pi h(1+\delta)}{M}\left(\frac{N+1}{2} - l\right)\right], \end{aligned} \tag{4.24}$$

for $q = 0, ..., K_h$ and $l = 1, ..., \frac{N+1}{2}$, while

$$\begin{aligned} \left(\Gamma_{K_h}^{(h)}(\delta)\right)_{lq} &= l^{K_h - q} \cos\left[\frac{2\pi h(1+\delta)}{M} l\right], \\ \left(\Delta_{K_h}^{(h)}(\delta)\right)_{lq} &= l^{q} \sin\left[\frac{2\pi h(1+\delta)}{M} l\right], \end{aligned} \tag{4.25}$$

for $q = 0, ..., K_h$ and $l = 1, ..., \frac{N-1}{2}$.

Observe that using the result of the IpDFT step, namely equation (4.18), it is possible to tune the coefficients of $\mathcal{M}(\delta)$ through a better estimation of the real frequency, which ultimately, returns better estimates than assuming that the waveform has a nominal frequency (i.e. that $\delta = 0$).

Again, it is possible to use a window function to smooth the Taylor's series approximation errors at the boundaries of the observation interval considered. The elements of the unknown vector $\mathbf{X}$ can therefore be estimated using a Weighted Least Squares (WLS) approach, i.e.

$$\hat{\mathbf{X}}_r = 2\left[\mathcal{M}(\hat{\delta})^T V^T V \mathcal{M}(\hat{\delta})\right]^{-1} \mathcal{M}(\hat{\delta})^T V^T V \mathbf{x}_r \tag{4.26}$$

where $V = \text{diag}\{v(0), \ldots, v(N-1)\}$ is the $N \times N$ diagonal matrix built using the coefficients of window $v(\cdot)$. Notice that the computation of (4.26) relies only on real-valued terms, while in the classic TFT the elements of $\mathcal{M}(\cdot)$ (equation 4.15) are complex-valued [144], [163]. The computational burden of the algorithm is therefore reduced with respect of the traditional complex-valued algorithm. Moreover, noticing that the size of $\mathcal{M}$ depends on the number H of harmonics used in the model, it is possible to further reduce the computational burden of the algorithm.

In the classic TFT, H can be large, up to 50, assuming that all the harmonics have to be estimated, as sometimes it is needed to estimate all of them or to find the Total Harmonic Distortion (THD). For synchrophasor estimation purposes, however, the impact of high order harmonics on the fundamental tone is quite low [162], while including in the model and estimating the first harmonics (e.g. up to the 4-th) can be advantageous. This behavior is not clearly visible when the window is a rectangular, due to its relevant spectral leakage, but it becomes more noticeable when two-term cosine-class windows are used. Moreover, the impact of harmonics on the synchrophasor estimation accuracy does not depend only on harmonics order and magnitude, but also on the length of observation interval, i.e. the (nominal) number of cycles observed C. This affect the width of the spectral main-lobes associated with the various waveform harmonic components. Therefore a trade-off is needed between the number of harmonics to be included in (4.22) and the observation interval length.

When C is low, to avoid that harmonics spectral components interfere with the main tone estimation, they are included in the system model (4.22). In this way, harmonics have a lower impact on the estimation of the fundamental phasor. On the other hand, when C is large enough, this is not needed, and the model can be

simplified. With a number of simulations, it was found that the estimation accuracy does not significantly change if:

- $H \geq 4$ for $C = 2$;
- $H \geq 3$ for $C = \{3, 4\}$;
- $H \geq 2$ for $C = \{5, 6, 7\}$.

Therefore, the TLTFT adaptively changes the number of harmonics included in the model as a function of the observation interval length C used. Finally, as introduced in the previous section, the Taylor's series of the harmonics can be truncated to order $K = 0$. Tracking harmonics over time is indeed unnecessary at the moment, as harmonic distortion is usually a steady-state contribution (as implicitly supposed by the IEEE Standard as well). This choice further reduces the overall computational burden of the algorithm.

In conclusion, the synchrophasor magnitude, phase, frequency and ROCOF at time t_r are given by [164]:

$$\begin{aligned}
\hat{X}(t_r) &= \sqrt{\hat{X}_{R_0}^{(1)^2} + \hat{X}_{I_0}^{(1)^2}} \\
\hat{\varphi}(t_r) &= \operatorname{atan} \frac{\hat{X}_{I_0}^{(1)}}{\hat{X}_{R_0}^{(1)}} \\
\hat{f}(t_r) &= f_0(1 + \hat{\delta}) + \frac{f_s}{2\pi} \frac{\hat{X}_{R_0}^{(1)} \hat{X}_{I_1}^{(1)} - \hat{X}_{I_0}^{(1)} \hat{X}_{R_1}^{(1)}}{|\hat{X}(t_r)|^2} \\
\widehat{ROCOF}(t_r) &= \frac{f_s^2}{\pi} \left[\frac{\hat{X}_{R_0}^{(1)} \hat{X}_{I_2}^{(1)} - \hat{X}_{I_0}^{(1)} \hat{X}_{R_2}^{(1)}}{|\hat{X}(t_r)|^2} - \right. \\
&\qquad \left. \frac{(\hat{X}_{R_0}^{(1)} \hat{X}_{R_1}^{(1)} + \hat{X}_{I_0}^{(1)} \hat{X}_{I_1}^{(1)})(\hat{X}_{R_0}^{(1)} \hat{X}_{I_1}^{(1)} - \hat{X}_{I_0}^{(1)} \hat{X}_{R_1}^{(1)})}{|\hat{X}(t_r)|^4} \right].
\end{aligned} \tag{4.27}$$

4.4 Simulations and results

The TLTFT algorithm described so far was tested in a simulated environment (through MATLAB) and using the physical testbed described in Chapter 3. In both cases, the sampling frequency was set to 8 kHz. The results of the simulations are shown in the following tables: Table 4.1 for the P class implementation and Table 4.2 for the M class counterpart.

The very same testing conditions were replicated on the physical testbed and the corresponding results are shown in Table 4.3 for P class and Table 4.4 for M class.

In all cases, the MIR window was used in both algorithm stages, i.e. $w(\cdot) = v(\cdot)$. This choice is due to the fact that the MIR window provides a good trade-off between accuracy and responsiveness compared to other windows. The synthesized signal was generated with a SNR $= 80$ dB. The initial phases of the fundamental component and the various disturbances considered (i.e. harmonics, inter-harmonics, modulating tones) were randomized over 200 independent records. The size of these data vectors are different for P class and M class. In the first case, responsiveness is more important than accuracy. Therefore shorter intervals are considered ($C = \{2, 3, 4\}$). For M class, the number of cycles considered is $C = \{5, 6, 7\}$, as longer intervals provide better accuracy. Of course the results are slightly different because, not only the observation interval length, but also the number of harmonics included in the model changes.

Concerning the results in the tables, a couple of comments deserve attention.
The accuracy of the designed algorithm is satisfactory for both P class and M class. However, in the latter case, full Standard compliance is assured only for $C = 7$. The effect of harmonics is almost negligible in all cases. This is achieved in two different ways: for $C \leq 4$, an adequate number of harmonics are included in the model, therefore their impact on fundamental phasor estimation is reduced as they are correctly estimated. Conversely, for $C \geq 5$ it is no longer needed to include harmonics higher than the second in the model.
As C increases, the sensitivity to amplitude and phase modulation disturbances grows. This is a customary effect for algorithms based on Taylor's series approximation, as the approximation errors increase with the distance from the central reference time of the observation interval. Nevertheless, the IEEE Standard limits are safely met.
The most critical results are obtained under the effect of out-of-band interferences, particularly when they are close to the main tone, i.e. 25 and 75 Hz with a reporting rate of 50 fps. Under this testing conditions, the TVE, FE and RFE values are below the IEEE Standard limits only for $C = 7$.

It is interesting to note that, instead of using harmonics in the TFT model, one can purposely choose to include interharmonics and then, estimating these components, to reduce the influence on the main tone. However, this approach works only if the interharmonic position is known, and despite the standard provides some intervals, they are too wide with respect to the frequency resolution of the TLTFT. In practice, placing some interharmonics frequencies in the model has not a satisfactory effect on the overall estimation. In fact, the estimation accuracy gain in presence of inter-harmonics is only minor. Moreover, including interharmonics in the model may increase the sensitivity to harmonics far from the main tone.

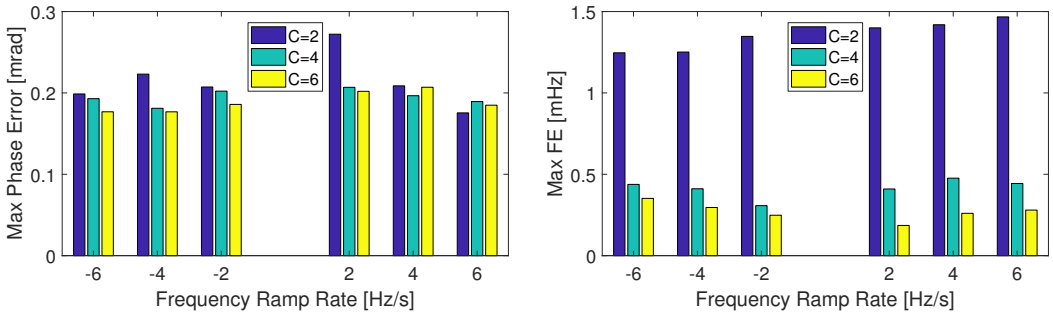

(a) (b)

FIGURE 4.3: Experimental results (phase and frequency errors) using a chirp waveform between 45 and 55 Hz at different rates.

In the context of active distribution networks, dynamic disturbances are commonly observed and the angle differences between voltage bus and current branch phasors are expected to be extremely small. The small TVE values in steady-state conditions already highlight the high performance of the TLTFT. To clarify the behavior of the algorithm in dynamic conditions, in Figure 4.3 the experimental results in terms of phase and frequency error are reported when the frequency changes linearly from 45 Hz to 55 Hz at the rates of ± 2 Hz/s, ± 4 Hz/s and ± 6 Hz/s. In this case, the phase error is the most interesting parameter, as it ranges between 0.2 and 0.3 mrad, with minor fluctuations that are independent of the frequency ramp rate. Note that this testing conditions are not present in the IEEE Standard.

TABLE 4.1: Maximum TVE, FE and RFE values obtained in simulation for some Class P tests reported in the IEEE Standards C37.118.1-2011 and C37.118.1a-2014 when observation lengths of $C = \{2, 3, 4\}$ cycles are considered and $f_s = 8$ kHz. The IEEE C37.118.1a-2014 limits when the reporting rate is 50 fps are shown as well.

Test type	**Conditions**	**TVE [%]**	**FE [mHz]**	**RFE [Hz/s]**
Freq. offset ($\pm$2 Hz) and amplitude within $[0.8, 1.2]$ p.u.	C37.118 limits	1	5	0.4
	$C = 2$	0.00	0.3	0.10
	$C = 3$	0.00	0.3	0.04
	$C = 4$	0.00	0.2	0.02
Freq. ramp ($\pm$2 Hz) at 1 Hz/s	C37.118 limits	1	10	0.2
	$C = 2$	0.00	0.4	0.11
	$C = 3$	0.00	0.4	0.03
	$C = 4$	0.00	0.3	0.02
Freq. offset ($\pm$2 Hz) + 1% 2nd harmonic	C37.118 limits	1	5	0.4
	$C = 2$	0.00	0.9	0.18
	$C = 3$	0.00	0.2	0.04
	$C = 4$	0.00	0.1	0.02
Freq. offset ($\pm$2 Hz) + 1% 3rd harmonic	C37.118 limits	1	5	0.4
	$C = 2$	0.00	0.6	0.19
	$C = 3$	0.00	0.3	0.04
	$C = 4$	0.00	0.1	0.02
Freq. offset ($\pm$2 Hz) + 1% 4th harmonic	C37.118 limits	1	5	0.4
	$C = 2$	0.00	0.5	0.12
	$C = 3$	0.00	0.3	0.04
	$C = 4$	0.00	0.1	0.02
AM (10% at 2 Hz)	C37.118 limits	3	60	2.3
	$C = 2$	0.00	0.3	0.15
	$C = 3$	0.00	0.2	0.03
	$C = 4$	0.00	0.2	0.01
PM (0.1 rad at 2 Hz)	C37.118 limits	3	60	2.3
	$C = 2$	0.00	0.8	0.13
	$C = 3$	0.00	1.3	0.04
	$C = 4$	0.00	1.9	0.03

TABLE 4.2: Maximum TVE, FE and RFE values obtained in simulation for some Class M tests reported in the IEEE Standards C37.118.1-2011 and C37.118.1a-2014 when observation intervals of $C = \{5, 6, 7\}$ cycles are considered and $f_s = 8$ kHz. The IEEE C37.118.1a-2014 limits when the reporting rate is 50 fps are shown as well.

Test type	**Conditions**	**TVE [%]**	**FE [mHz]**	**RFE [Hz/s]**
Freq. offset ($\pm$5 Hz) and amplitude within $[0.8, 1.2]$ p.u.	C37.118 limits	1	5	0.1
	$C = 5$	0.00	0.1	0.01
	$C = 6$	0.00	0.1	0.01
	$C = 7$	0.00	0.1	0.01
Freq. ramp ($\pm$5 Hz) at 1 Hz/s	C37.118 limits	1	10	0.2
	$C = 5$	0.00	0.3	0.02
	$C = 6$	0.00	0.4	0.01
	$C = 7$	0.00	0.3	0.01
Freq. offset ($\pm$5 Hz) + 10% 2nd harmonic	C37.118 limits	1	25	-
	$C = 5$	0.00	0.1	0.01
	$C = 6$	0.00	0.1	0.01
	$C = 7$	0.00	0.1	0.00
Freq. offset ($\pm$5 Hz) + 10% 3rd harmonic	C37.118 limits	1	25	-
	$C = 5$	0.00	0.1	0.01
	$C = 6$	0.00	0.1	0.01
	$C = 7$	0.00	0.1	0.01
Freq. offset ($\pm$5 Hz) + 10% 4th harmonic	C37.118 limits	1	25	-
	$C = 5$	0.00	0.1	0.01
	$C = 6$	0.00	0.1	0.01
	$C = 7$	0.00	0.1	0.00
AM (10% at 5 Hz)	C37.118 limits	3	300	14
	$C = 5$	0.04	3.1	0.04
	$C = 6$	0.07	4.6	0.03
	$C = 7$	0.13	7.4	0.06
PM (0.1 rad at 5 Hz)	C37.118 limits	3	300	14
	$C = 5$	0.03	42	1.2
	$C = 6$	0.07	62	1.6
	$C = 7$	0.12	79	2.2
10% out-of-band interference	C37.118 limits	1.3	10	-
	$C = 5$	3.2	196	44
	$C = 6$	1.2	34	13
	$C = 7$	0.19	6.1	1.2

TABLE 4.3: Maximum TVE, FE and RFE values obtained on the testbed for some Class P tests reported in the IEEE Standards C37.118.1-2011 and C37.118.1a-2014 when observation lengths of $C = \{2, 3, 4\}$ cycles are considered and $f_s = 8$ kHz. The IEEE C37.118.1a-2014 limits when the reporting rate is 50 fps are shown as well.

Test type	**Conditions**	**TVE [%]**	**FE [mHz]**	**RFE [Hz/s]**
Freq. offset ($\pm$2 Hz) and amplitude within $[0.8, 1.2]$ p.u.	C37.118 limits	1	5	0.4
	$C = 2$	0.02	1.8	0.78
	$C = 3$	0.02	0.7	0.13
	$C = 4$	0.02	0.4	0.05
Freq. ramp ($\pm$2 Hz) at 1 Hz/s	C37.118 limits	1	10	0.2
	$C = 2$	0.02	1.8	0.55
	$C = 3$	0.02	0.6	0.14
	$C = 4$	0.02	0.4	0.04
Freq. offset ($\pm$2 Hz) + 1% 2nd harmonic	C37.118 limits	1	5	0.4
	$C = 2$	0.02	2.2	0.88
	$C = 3$	0.02	0.6	0.15
	$C = 4$	0.02	0.4	0.04
Freq. offset ($\pm$2 Hz) + 1% 3rd harmonic	C37.118 limits	1	5	0.4
	$C = 2$	0.02	2.1	0.72
	$C = 3$	0.02	0.6	0.16
	$C = 4$	0.02	0.4	0.04
Freq. offset ($\pm$2 Hz) + 1% 4th harmonic	C37.118 limits	1	5	0.4
	$C = 2$	0.02	1.8	0.68
	$C = 3$	0.02	0.6	0.17
	$C = 4$	0.01	0.5	0.05
AM (10% at 2 Hz)	C37.118 limits	3	60	2.3
	$C = 2$	0.02	0.8	0.70
	$C = 3$	0.02	0.6	0.16
	$C = 4$	0.02	0.4	0.05
PM (0.1 rad at 2 Hz)	C37.118 limits	3	60	2.3
	$C = 2$	0.02	1.9	0.20
	$C = 3$	0.02	1.5	0.08
	$C = 4$	0.02	2.0	0.06

TABLE 4.4: Maximum TVE, FE and RFE values obtained on the testbed for some Class M tests reported in the IEEE Standards C37.118.1-2011 and C37.118.1a-2014 when observation intervals of $C = \{5, 6, 7\}$ cycles are considered and $f_s = 8$ kHz. The IEEE C37.118.1a-2014 limits when the reporting rate is 50 fps are shown as well.

Test type	**Conditions**	**TVE [%]**	**FE [mHz]**	**RFE [Hz/s]**
Freq. offset ($\pm$5 Hz) and amplitude within $[0.8, 1.2]$ p.u.	C37.118 limits	1	5	0.1
	$C = 5$	0.01	0.2	0.03
	$C = 6$	0.01	0.2	0.02
	$C = 7$	0.01	0.2	0.01
Freq. ramp ($\pm$5 Hz) at 1 Hz/s	C37.118 limits	1	10	0.2
	$C = 5$	0.02	0.3	0.03
	$C = 6$	0.02	0.2	0.02
	$C = 7$	0.02	0.2	0.01
Freq. offset ($\pm$5 Hz) + 10% 2nd harmonic	C37.118 limits	1	25	-
	$C = 5$	0.01	0.3	0.03
	$C = 6$	0.01	0.2	0.02
	$C = 7$	0.01	0.2	0.01
Freq. offset ($\pm$5 Hz) + 10% 3rd harmonic	C37.118 limits	1	25	-
	$C = 5$	0.01	0.3	0.03
	$C = 6$	0.01	0.2	0.02
	$C = 7$	0.01	0.2	0.01
Freq. offset ($\pm$5 Hz) + 10% 4th harmonic	C37.118 limits	1	25	-
	$C = 5$	0.01	0.3	0.03
	$C = 6$	0.01	0.2	0.02
	$C = 7$	0.01	0.2	0.01
AM (10% at 5 Hz)	C37.118 limits	3	300	14
	$C = 5$	0.06	3.2	0.04
	$C = 6$	0.09	4.9	0.05
	$C = 7$	0.14	7.2	0.07
PM (0.1 rad at 5 Hz)	C37.118 limits	3	300	14
	$C = 5$	0.03	40	1.2
	$C = 6$	0.07	56	1.6
	$C = 7$	0.12	75	2.2
10% out-of-band interference	C37.118 limits	1.3	10	-
	$C = 5$	3.2	196	44
	$C = 6$	1.2	33	13
	$C = 7$	0.12	6.5	1.2

CHAPTER 5

A low-cost embedded PMU implementation

In this chapter, the implementation of the TLTFT on a simple and low cost embedded platform is discussed. The most stringent problem is the real-time performance that a PMU has to deliver. Time synchronization and clock syntonization are crucial issues, usually solved with custom hardware solutions. On the contrary, in this case synchronization and syntonization are provided by a standard, properly optimized servo clock, implemented via software, using the resources available on the chosen embedded platform, i.e. a BeagleBone Black.

5.1 Introduction

As explained in the previous chapters, the implementation of a complete PMU is rather complex. The estimation algorithm usually deserves a particular attention, because of the high data rates that are required by the IEEE Standards. Even if some commercial PMUs are available, several research-oriented prototypes have been proposed as well. One of the most famous is the µPMU [165] which is an accurate PMU developed by University of California Berkeley and based on a commercial high-resolution power disturbance recorder produced by Power Standard Lab (PSL)[1]. Its implementation details are not disclosed, while the deployment of this instrument costs around $3500 per measurement point [91].
Many other research groups instead run PMU prototypes on FPGA platforms, mainly to speed up the synchrophasor estimation. *National Instruments* is well known for

[1] https://www.powerstandards.com/product/micropmu

providing a complete PMU based on its CompactRIO development platform. This is a resource-rich device, equipped with both an ARM processor and a Xilinx FPGA featuring very high computational capabilities, high-end synchronization modules and high-resolution ADCs. This platform is used by several groups [88], [166] and *National Instruments* itself sells it as a solution for PMU implementation.
In [167] a PMU is implemented on a commercial board designed for high-end industrial IoT applications, namely the IoT Octopus from NovTech. This implementation takes advantage of the powerful Cyclone V FPGA SoC by Intel and a 24-bit ADC running at 32 kHz. The cost of this solution is around 1000$, most of which are due to the FPGA. The major drawback of using FPGAs, in fact, is their cost, besides the fact that they are relatively hard to program. For these reasons, the actual direction is to implement computationally efficient yet effective algorithms that can run on simpler platforms as well [142], [163].
Single Board Computers (SBCs) are perfect candidates for this purpose. Their growth in the last decade has been impressive and, starting from the Raspberry PI, their cost has decreased, leading to a widespread use in many application fields. In the scientific literature there are many examples of applications built on top of these boards, also for power system applications. For instance, a frequency disturbance recorder (FDR) can be implemented on a BeagleBone Black [168].

OpenPMU[2] is an international project whose purpose is to build an open-source PMU for power system analysis and research activities. The project started in 2009, but different hardware resources were used for PMU implementation [169]. Currently OpenPMU relies on a BeagleBone Black as main acquisition and synchronization platform. Some details of this implementation are described in [170]. Data acquisition is performed through an AD7606 by Analog Devices, which is a 16-bit simultaneous sampling ADC, with a rated SNR of 94.2 dB[3]. A GPS receiver provides the syntonized 12.8 kHz signal to discipline the ADC sampling frequency. Finally, OpenPMU supports both the IEEE Standard C37.118.2 and IEC 61850-90-5 to transmit the synchrophasor measurements to a PDC.

In [171] a similar approach is presented, using a 12-bit commercial acquisition module (namely a MCC USB 201) running at 12.5 kHz which is coupled with a Raspberry PI (which runs the synchrophasor estimation algorithm) and a GPS receiver for time synchronization. The prototype was called LOCO PMU (LOw-COst PMU) and its total cost was reported to be around 250 euros. The prototype showed valuable results, but the full IEEE Standard compliance is not reported [172]. Besides that, this prototype was calibrated to produce accurate measurement when

[2] www.OpenPMU.org
[3] Datasheet at https://www.analog.com/en/products/ad7606.html

TABLE 5.1: An hardware comparison of some recent PMU implementations.

Ref.	Processing platform	ADC	Sync.	Estimated cost range	Year
[173]	not reported	16bit @ 500kSps [DT 9832]	GPS [XL-750]	n.a.	2008
[174]	[PXI 8106]	14bit @ 2.5MSps [PXI-6133]	GPS [PXI-6682]	10 k€	2009
[175]	FPGA Stratix 2 [NIOS 2]	16bit @ 12.8kSps [AD7656]	IEEE 1588 [DP83640]	n.a.	2013
[169]	PC CPU	14bit @ 6.4kSps [NI USB-6009]	GPS [Garmin]	1 k€	2013
[176]	Intel Quad Core [PXI-8110]	24bit @ 50kSps [PXI-6281]	GPS [PXI-6682]	>10 k€	2013
[88]	FPGA Virtex 5 [cRIO]	24bit @ 50kSps	GPS	10 k€	2014
[177]	FPGA Artix 7 [cRIO]	16bit @ 50kSps [NI-9215]	GPS [NI-9467]	10 k€	2015
[178]	FPGA [cRIO]	16bit @ 50kSps [NI-9215]	GPS [NI-9467]	10 k€	2016
[167]	FPGA Cyclone V [IoT Octopus]	24bit @ 32kSps [AD7770]	GPS [Telit]	<1 k€	2017
[171]	Raspberry PI	12bit @ 10kSps [MCC USB 201]	GPS [MTK3339]	250 €	2017
[170]	BeagleBone Black	16bit @ 12.8kSps [AD7606]	GPS [uBlox]	100 €	2017

coupled to a specific instrument transformer, highlighting the need to calibrate the PMU along with the specific transducer adopted.

Many others PMU implementations can be found in the literature, although many research activities are focused on PMU algorithms and its innovative applications rather than its implementation. For this reason, it is hard to compare the characteristics, the cost and the performances of the PMU used. Table 5.1 shows a comparison between the hardware resources used for some recent PMU implementation found in the literature.

The performances achieved with a different hardware are hardly comparable because of the often incomplete information that are reported by the authors. Moreover, despite included in the PMU setup, the development of a PMU usually does not include the transducers, whose metrological features may also strongly affect the overall measurement uncertainty [179]–[181]. Some standards (e.g. the IEC 61869) specify the metrological characteristics of instrumentation transformers

(ITs), dividing them into two different classes based on their accuracy and working principles, namely the *"conventional"* ITs (which include voltage and current inductive and capacitive transformers) and the *"low power"* ITs (e.g. Rogowski coils and Hall-effect transducers). The standard specifies various accuracy classes, i.e. class 0.1, 0.2, 0.5 or 1 are the nominal values for current transformer (CT) and class 0.1, 0.2, 0.5, 1 and 3 are the respective voltage transformer (VT) classes. For instance, a class 0.5 CT may introduce a nominal systematic deviation within $\pm 0.5\,\%$ of the rated value and a phase displacement of ± 9 mrad. This kind of CTs is commonly used in medium voltage grids, but in the case of synchrophasor measurement it is not enough [182]. In fact, even if it was considered to be the only source of uncertainty on the measurement chain, the resulting TVE can be higher than 1 % (by summing the errors in amplitude and phase). Therefore, even if a PMU is compliant to the IEEE Std. C37.118.1, the overall measurement uncertainty may exceed the limits reported in it. Moreover, *"no particular PMU-application standards have been written to specify the performance of the instrument transformers that they are connected to"* [110]. Considering the many uncertainty contributions affecting the data collected by a PMU (e.g. the instrumentation cable also play a role in a substation deployment), it is clear that the choice of transducers may has an important impact on the overall synchrophasor measurement uncertainty [110]. In the practice, compensation routines are applied at runtime, which however require knowledge of the metrological characteristics of the specific CTs or VTs adopted.

5.1.1 Synchrophasor on embedded platform

As previously introduced, many SBCs have recently gained great attention from researcher, also boosted by the growing interest of the scientific community in developing IoT applications. Many SBCs are characterized by a limited cost and size, good expansion capability and fairly high computational performance. One of the last trends, partially boosted by the availability of such cheap and efficient SBCs, is the so called edge computing, that is the decentralized processing of information, that in this way remains at the edges of the network.
Besides the famous Raspberry Pi, some SBCs have been developed for industry application, therefore including a large set of connectivity ports and industrial protocols, as well as enhanced digital signal processing capability.

The platform chosen for the TLTFT algorithm prototyping (discussed in Chapter 4) is a BeagleBone Black[4] (BBB), mainly because it is low-cost and it is specifically

[4] https://beagleboard.org/black

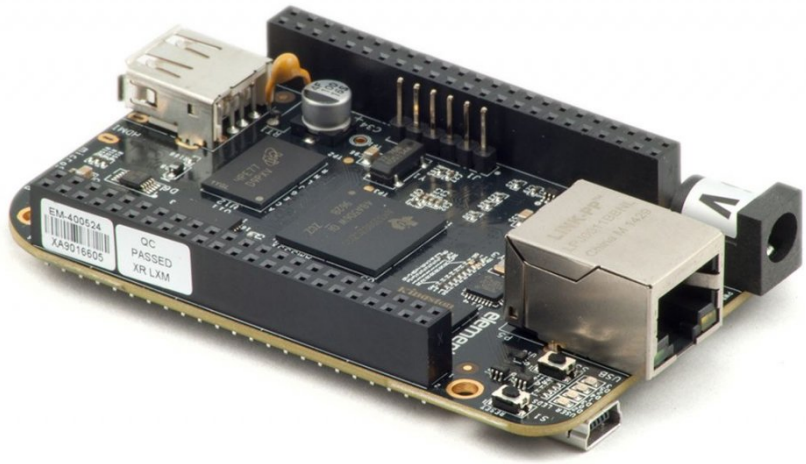

FIGURE 5.1: Picture of a BeagleBone Black board.

designed to run real-time applications (as a PMU need). This embedded development platform (Figure 5.1) features a Sitara AM3358 ARM Cortex-A8 processor by Texas Instruments supported by 4 GB of eMMC memory and 512 MB of DDR3 SDRAM. The clock speed of the ARM core is 1 GHz. The board is fully open source, so all the schematics and software are public and can be modified if necessary. The operating system (OS) running on the board is a Linux distribution based on Kernel 3.8. However, it is easy to update the kernel to a newer version, with PREEMPT-RT support as well. The BBB has plenty of peripherals and communication interfaces, such as a USB port, a HDMI interface, a 10/100 Ethernet port and two 46-headers for General Purpose Input/Output (GPIO) expansion. Moreover, it is easy to exploit the number of low-level peripherals of the AM3358, e.g. UART, SPI and I^2C ports, a 12-bit ADC and some timers. A detailed architecture of the AM3358 is depicted in Figure 5.2.

The BBB is not the fastest board available in the market, because, for instance, a Raspberry PI 3 is definitively faster with its 4-core 64-bit processor. The key advantage of the BBB compared with other development boards is the presence of two co-processors on board, specifically designed to run real-time and I/O tasks. These co-processors, called Programmable Real-time Units (PRUs), run at 200 MHz, with a reduced instruction set, but with a direct access to peripherals and I/O. Thanks to its architecture, each PRU can deliver deterministic performance. In fact, it does not support asynchronous interrupts and no operating system is running on the PRU. Therefore the software overhead is minimal.

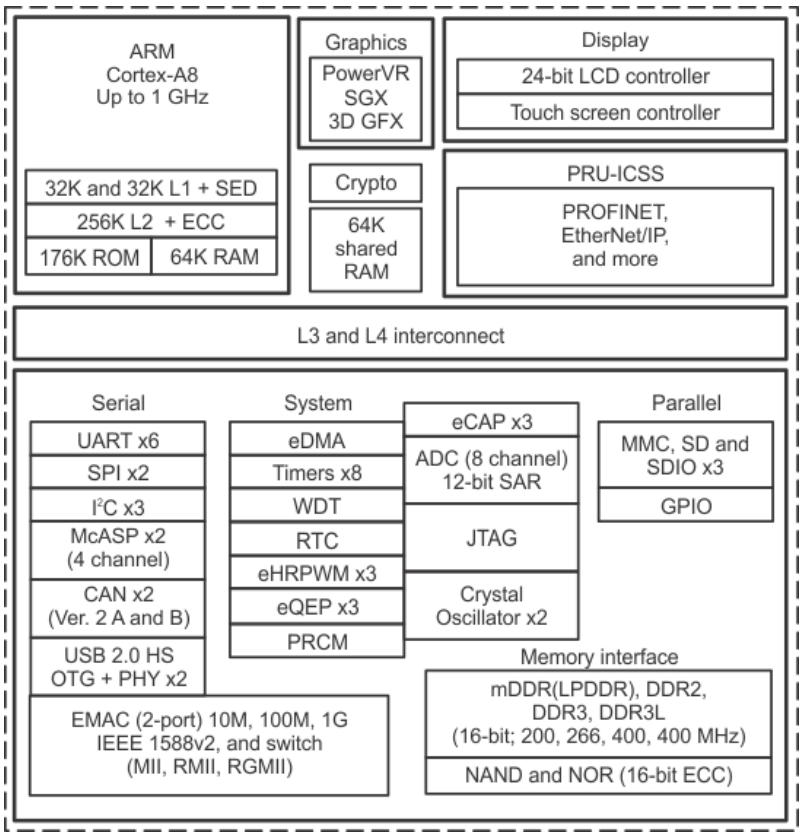

FIGURE 5.2: AM3358 functional diagram.
From http://www.ti.com/product/AM3358

In order to communicate with the main ARM core, a shared 12 kB of RAM memory and dedicated interrupt lines between ARM and PRUs can be used. On the other hand the computational capabilities of the PRU are limited: no floating point units are present and the local memory is quite small and easy to fill when many mathematical operations are required.

The flexibility of this board, along with the wide community using it, make it a good candidate also for research purposes. This is confirmed by many contributions that can be found in the scientific literature, also dealing with PRU programming [183].

5.2 Algorithm Implementation

The TLTFT algorithm described in the Chapter 4 has been designed and implemented for the BeagleBone Black. Then, the same C/C++ code has been deployed on the testbed described in the previous Chapter 3.

The choice of C coding is driven by the improved efficiency level achievable. The MATLAB code exporting tool is indeed not advisable in this case, as it produces heavy and not optimized programs, whose processing time is not compatible with the time constraints of a PMU implemented on a platform like the BBB. On the contrary, C coding gives to programmers the possibility to control the single processing operation and to manage the memory at a low level.

The code of the algorithm is compiled using GCC v4.6.3 for the BBB and relies on the *Eigen* library[5] for optimized linear algebra. The BBB kernel was patched for real-time operations. The compiler actually makes the difference as it has to parallelize all the mathematical operations in the Floating Point Unit (FPU). The BBB processor in fact has an FPU with a Single-Instruction Multiple-Data (SIMD) hardware accelerator that enables fast array processing, based on ARM NEON instructions. The use of the mentioned *Eigen* library is driven by its interesting features, namely the vectorization support for the NEON accelerator and the use of the *de facto* standard for low-level routines for linear algebra operations, i.e. the Basic Linear Algebra Subprograms[6] (BLAS).
Almost all the data processing is implemented using single precision floating point operations (i.e. using *float* variables), because the mentioned FPU has a 32-bit data path. The impact of a double-precision implementation on the numerical precision was assessed and found to bring only minor improvements. However, the processing time of a single precision implementation is about 35 % shorter than in the double precision case.
As explained in Section 4.3, an important advantage of the TLTFT algorithm is the use of real-valued quantities. In fact, the TLTFT processing time is about 50 % shorter than the complex-valued implementation described in [163] for the same data record length N. The comparison is shown in Figure 5.3.

PMU Processing time

As a general rule, the time to process data and to return a single synchrophasor measurement result should be smaller than 16 ms. This constraint comes from the need of producing a mandatory reporting rate of 60 fps, as prescribed by the IEEE standard C37.118.1-2011 [103] for 60 Hz systems. In this work, the limit of 20 ms is considered, as in Europe the standard expects a maximum reporting rate of 50 fps for a power system frequency of 50 Hz.

[5] http://eigen.tuxfamily.org/
[6] www.netlib.org/blas/

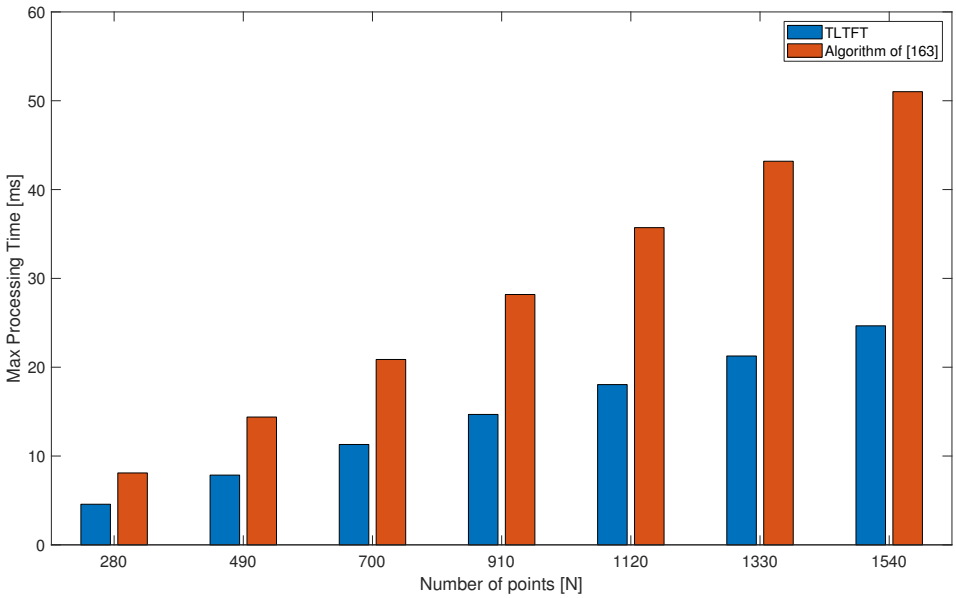

FIGURE 5.3: Processing time comparison between the TLTFT and the algorithm in [163] for different number of samples N and $C = 7$. (from [184] with permissions)

The processing time depends mainly on a couple of parameters: the sampling frequency and the number of nominal power line cycles C in each observation interval. These parameters directly affect the size of the data record to be processed. Of course, the longer the observation interval, the longer the PMU latency. As explained in Section 2.5, P class PMUs are envisioned for high responsiveness applications, thus it is fair to expect a small number of observed cycles C for this instrument class. In this respect, setting $C = 2$ is a sensible choice. For a M class instruments, instead, C can easily be higher than 6, because the estimation accuracy of the algorithms usually grow with the number of power line cycles observed. Concerning the PMU sample rate, it affects the processing time in the same way: by increasing the sampling frequency, both the amount of data and the time to process it grows, but the overall estimation accuracy improves as well.
In general, a trade-off between accuracy, observation interval length and sampling frequency needs to be achieved to ensure real-time operation with the platform adopted.
In this respect, the TLTFT algorithm running on the BBB meets the wanted time constraints. Indeed, the processing time of the TLTFT is generally under the limit of 20 ms, as depicted in Figure 5.4. The processing time was measured with low-level timers on the BBB for different sampling frequencies ranging from 2 kHz to 12 kHz. The maximum processing time was computed over 100 iterations of the

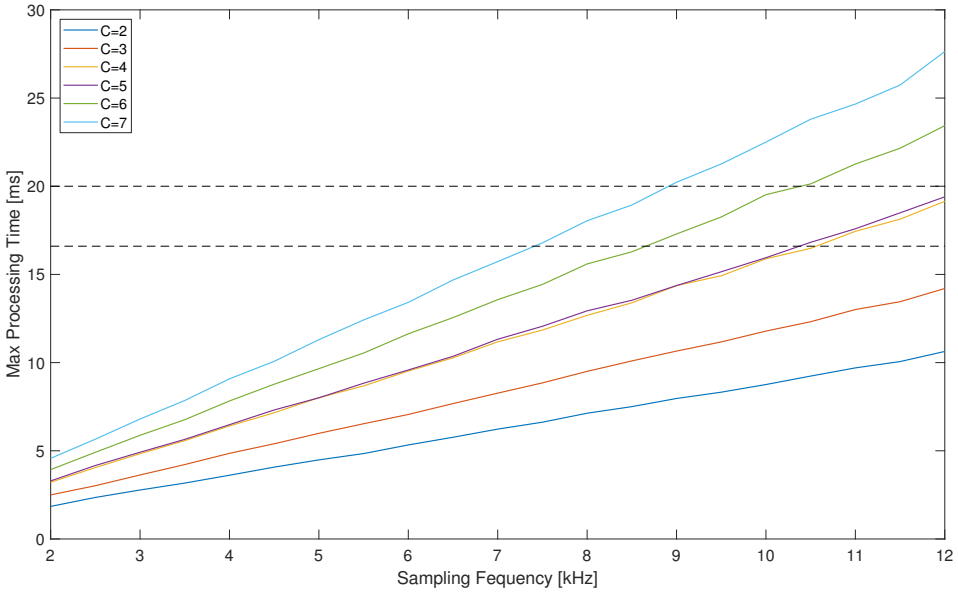

FIGURE 5.4: Maximum processing time of TLTFT algorithm on the BeagleBone Black. The curves are made changing the sampling frequency and observation interval length C

algorithm. In general, processing times are quite deterministic, exhibiting only minor fluctuations. Moreover, they tend to grow linearly with the sampling frequency (i.e. with the data record size N). This is consistent with the order of complexity of both the IpDFT and TFT stages of the TLTFT.
From Figure 5.4 it is possible to observe an apparently weird behavior in the cases of $C = 4$ and $C = 5$. The two lines are very close, even if the observation interval length and the related data record size are different. This is caused by the different number of harmonics included in the model, i.e. $H = 3$ and $H = 2$ for $C = 4$ and $C = 5$, respectively. As a result, the size of the matrix to be inverted in (4.26) is different and the smaller number of operations needed for $C = 5$ compensates for the larger amount of data to be processed. A similar situation, yet less evident, occurs when $C = 2$ and $C = 3$. The dashed horizontal lines of Figure 5.4 represent the time limits ensuring real-time reporting rates at 50 fps and 60 fps, respectively.

Observe that with a sampling frequency of $f_s = 8$ kHz a reporting rate of 50 fps can be safely achieved even with $C = 7$. To assure a reporting rate of 60 fps over 7 cycles, the sampling frequency should be slightly reduced.

Concerning the choice of sampling frequency and number of cycles C, another consideration can be done, with respect to the input wideband noise.

Effective ADC resolution settings

Taking care of the type of instrument (P or M class), another trade-off between accuracy, observation interval length and sampling frequency needs to be achieved. From a PMU design perspective, the impact of wideband noise could be considerable especially on ROCOF estimation. According to [185], in order to reduce the ROCOF estimation uncertainty below reasonable levels, the following condition should be met:

$$SNR \geq 10 \log_{10} \left(\frac{\beta_{RFE}^2}{f_s} \frac{2 f_0 \cdot \Gamma}{C^5} \right) \quad \text{dB} \tag{5.1}$$

where

- f_s, f_0 and C are the sampling frequency, the nominal power line frequency and the number of cycles in the observation interval, as previously defined;
- β_{RFE} is an algorithm-specific coefficient (approximately equal to 9 in the case considered) expressing the ratio between the 99.7th percentile of the ROCOF estimation error and the lowest possible root mean square (RMS) estimation error [185].

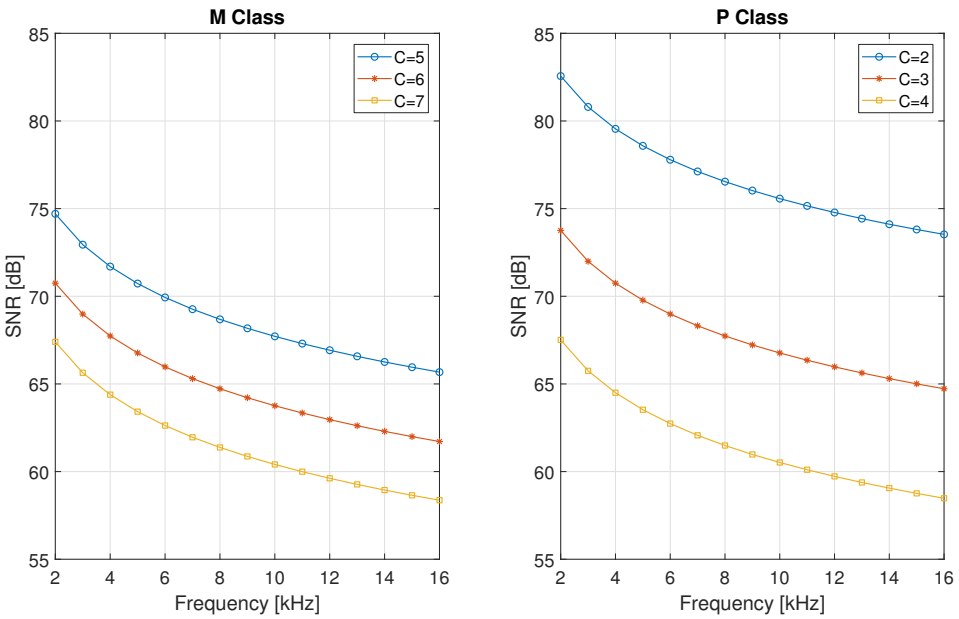

FIGURE 5.5: Maximum SNR values for which the RFE is smaller than 1/2 of the stricter limits of the standard τ_{RFE} as function of the sampling frequency, for different observation interval lengths C.

- $\Gamma = \frac{90 f_0^4}{\pi^2} \frac{F^2}{\tau_{RFE}^2}$ is a constant coefficient depending on
  1. The most stringent RFE limits τ_{RFE} reported in the IEEE Standards (i.e. $\tau_{RFE} = 0.4$ Hz/s and $\tau_{RFE} = 0.1$ Hz/s for class P and class M, respectively);
  2. An arbitrary factor (e.g. $F = 2$) which assures that the maximum noise-related uncertainty is F times smaller than such limits.

In Figure 5.5, the lowest SNR values enabling an RFE below τ_{RFE} for both M class and P class are depicted. The use of the RFE limits (instead of the FE or TVE) is driven by the fact that ROCOF estimation is most sensitive to noise. Therefore the resulting SNR limit is the most stringent one.

For instance, from (5.1) and using the previous considerations on processing time for $f_s = 8$ kHz, it is possible to estimate the maximum SNR affecting the input data with respect to the class and the number of cycles C. Figure 5.6 shows both the computational burden and the theoretical maximum SNR to meet the IEEE Standard requirements. These charts can be useful because from the knowledge of the input SNR it is possible to choose the sampling frequency or, on the contrary, it is possible to design a proper analog front-end for the PMU for a given sampling frequency.

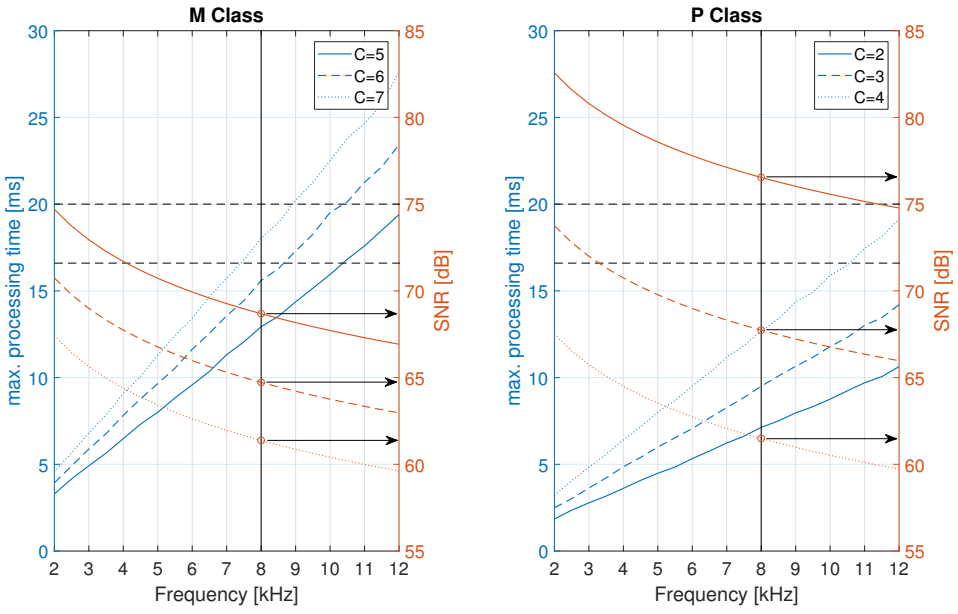

FIGURE 5.6: Example design of possible trade-offs between maximum processing (from Fig. 5.4) time and maximum SNR (from equation (5.1)). The arrows refer to the resulting SNR levels for a given sampling frequency of 8 kHz.

5.3 PMU Synchronization

Usually the sampling clock of a PMU is disciplined by a reference clock, through a synchronization technique that can be implemented in different ways. The local clock can be synchronized to the Universal Time Coordinated (UTC) with a direct GPS connection, or can take advantage of a clock distribution technology as IRIG-B or IEEE 1588. The operation of aligning a clock frequency to another reference frequency is commonly referred as *syntonization* (i.e. clock rate adjustment), while two clocks are *synchronized* if *"they have the same epoch and their measurements of the time of a single event at an arbitrary time differ by no more than [a specified] uncertainty"* [125].

Servo clocks (SCs) are feedback control systems tracking an input time reference. They can be realized in different ways. The basic scheme is based on a proportional integral (PI) controller fed with the time error, that in turn controls the actual local clock, thus correcting its offset. Several implementations of servo clocks are reported in the literature [186]. The most common examples of SCs are those developed for Ordinary and Boundary Clocks compliant with IEEE 1588 Standard [187], [188]. Other examples are used for distributed measurements over EtherCAT [189]. As far as power systems applications are concerned, IEEE 1588 is gaining more and more attention, due to its ability to synchronize the equipment usually deployed in a substation, including PMUs, usually within ± 1 µs. The recent introduction of the power profile of the IEEE 1588 by means of the IEEE Standard C37.238-2017 [127] confirms this trend. However, in both documents, no indication on SC design is provided.

The implementation of SC described in the following is specifically tailored for a possible PMU implementation on a low-cost embedded platform, such as the BBB, within the OpenPMU project mentioned in Section 5.1.

In particular, the synchronization of the OpenPMU is provided by an external GPS receiver. To discipline the sampling clock of the ADC, either a dedicated PLL in hardware (namely the AD9548) or a software PLL are used. The first is a commercially available IC by Analog Devices specifically designed for network synchronization and clocking applications [190], while the latter is a custom software PLL, tracking the input PPS signal, and implemented on a PRU of the BeagleBone Black. In the OpenPMU, in fact, the two PRUs control the acquisition and synchronization functions, respectively. A schematic of this implementation is shown in Figure 5.7.

The servo clock discussed in the next pages is conceived to be compatible with

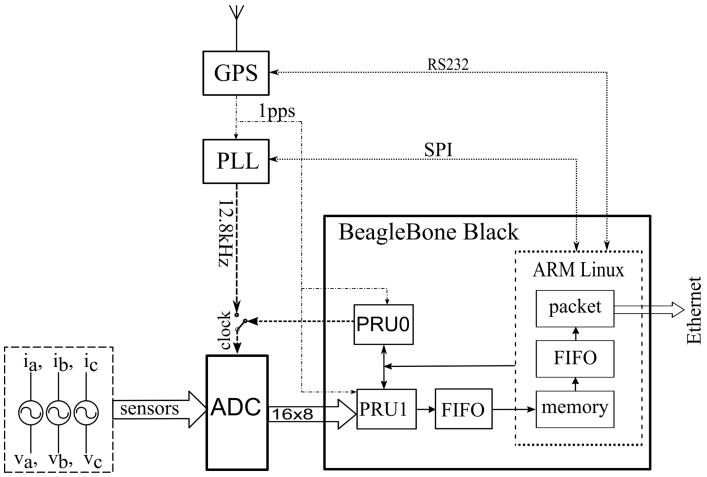

FIGURE 5.7: Architecture of the Acquisition and synchronization blocks as implemented in the OpenPMU project.
(from [170] with permissions)

OpenPMU, providing a disciplined sampling frequency and synchronization solution to timestamp measurement results, improving the previous performance, with no additional costs. In fact, no hardware PLL or synchronization circuit are needed, provided that the PRU timer can be initialized with UTC time (e.g. using PTP protocol).

The proposed SC has been designed to *(i)* minimize the synchronization uncertainty due to the rather poor quality of the local crystal oscillator (XO) on board of the BBB and *(ii)* to generate a stable sampling signal for digitizing the input waveforms.

5.3.1 Requirements

In the context of PMUs, time synchronization is needed to refer phasor, frequency and ROCOF measurements to a given reference time. Moreover, as explained in Chapter 2, the sampling rate needs to be stable and preferably syntonized to an integer multiple of the nominal power line frequency. At last, sometimes there is the need to compute the phasor at different positions of the same observation interval. The IEEE Standard C37.118.1 (in its first revision) reports that *"A phase error of 0.57 degrees (0.01 radian) will by itself cause 1% Total Vector Error (TVE) [...] This corresponds to a time error of* $\pm 26\,\mu s$ *for a 60 Hz system and* $\pm 31\,\mu s$ *for a 50 Hz system. [...] A time source that reliably provides time, frequency, and frequency stability at least 10 times better than these values corresponding to 1% TVE is highly recommended."*.

However, this was an underestimated boundary and, in the practice, the problem is more complex. For instance, it is possible to quickly estimate the maximum phase errors that result from the FE and RFE limits of the standard. Using the maximum values of such limits, combined with the maximum time misalignments [139], it follows that the maximum phase error (for P class) can be 8 mrad in steady-state testing conditions and up to 62 mrad for dynamic testing conditions, while for M class PMUs the limits are less strict [87]. It is widely accepted that the maximum error on time source of a PMU should be ± 1 µs. However, for future active distribution grids this limit should be lower, i.e. hundreds of ns [98], [191]. In fact, active distribution systems are very different from transmission ones (where PMUs were originally conceived to work on) and require more accurate measurements, because of the shorter distances and smaller power flows involved. For instance, differences of less than 1 mrad can be important for short lines. Distribution grid operators could be interested in phase angle differences tpically two orders of magnitude lower than those across transmission systems [91]. For example, the nominal phase measurement resolution of the µPMU in [165] is $\pm 0.01°$, where a $0.01°$ phase shift at 60 Hz corresponds to 0.46 µs.

5.3.2 Servo clock

The proposed Servo Clock (SC) has been implemented using a PRU of the BeagleBone Black board.

A classic SC can be modeled as a second-order discrete-time linear system. A PI controller acts directly on the time difference between the reference time and the local time, which in turn is used to adjust the local clock. The basic block diagram of the discrete-time model of a SC is depicted in Figure 5.8, where, t_m represents the absolute time reference (in IEEE 1588 this value is issued by a master clock) while t_c is the local clock time. A SC can actually be discretized in different ways, as explained, for instance, in [188], [193].

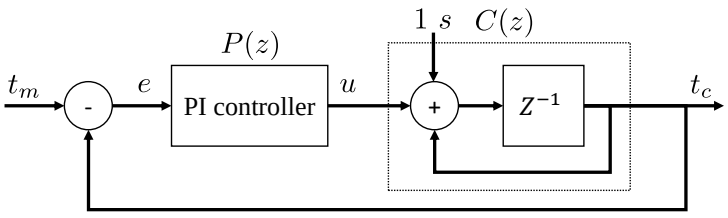

FIGURE 5.8: Model of the classic Servo Clock.
(from [192] with permissions)

In the z-domain, the servo clock basically consists of two blocks, i.e. the clock itself, represented as an accumulator, i.e.

$$C(z) = \frac{1}{z-1} \tag{5.2}$$

and the PI controller, that, using a classic backward Euler integration, has the following transfer function:

$$P(z) = K_P + K_I \cdot \frac{z}{z-1} \tag{5.3}$$

where K_P and K_I are the proportional and integral gains of the PI controller. Therefore, the closed-loop transfer function is:

$$H(z) = \frac{P(z)C(z)}{1 + P(z)C(z)} = \frac{(z-1)K_P + zK_I}{(z-1)^2 + (z-1)K_P + zK_I}. \tag{5.4}$$

Of course, the stability of the system is ensured if all the poles of $H(z)$ lie within the unit circle. In particular, the roots of the denominator of (5.4) have a magnitude smaller than 1 if and only if:

$$0 < K_P < 2 \tag{5.5}$$

$$0 < K_I < 4 - 2K_P \tag{5.6}$$

The corresponding stability region is plotted in Figure 5.9.

Besides ensuring stability, it is possible to tune the parameters K_I and K_P to meet wanted performance (e.g. convergence time or steady-state uncertainty), as explained in the following.

Implementation

Exploiting the peripherals of the BBB, and in particular using the PRU subsystem, it is possible to build a SC structurally different, but fundamentally equivalent to the one shown in Figure 5.8.

The structure of the servo clock actually implemented is depicted in Fig. 5.10. A purely software indirect frequency synthesizer is implemented to generate the 8 kHz signal clocking the Analog-to-Digital Converter (ADC) of the acquisition stage.

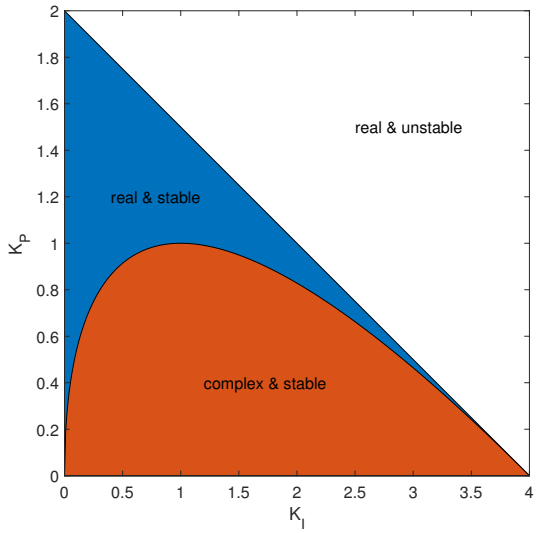

FIGURE 5.9: Stability region of the servo clock as a function of the PI coefficients.

Since a Voltage-Controlled Oscillator (VCO) is not available on the BBB, this is emulated by means of one of the timers of the PRU, clocked at 200 MHz and configured to be reloaded automatically. While the nominal timeout value to be loaded into the timer is 25000 ticks, its actual value is adjusted by the controller. The 8 kHz signal is used to increment both the system clock (which is implemented as a software counter properly initialized with a UTC timestamp as soon as it is available) and a second counter (labeled as *PPS generator* in Fig. 5.10) that generates a PPS signal. The difference in time (measured with a resolution of 5 ns) between the external (i.e. reference) PPS signal and the local one is integrated by a digital accumulator in order to compute the time error, which finally drives a PI controller adjusting the clock rate. Fig. 5.10 also highlights that the timer is driven by the main XO of the BBB. The main source of uncertainties are *(i)* the XO limited stability over time, and *(ii)* the jitter affecting the input PPS signal. In the following, these random processes are modeled with variables η and ν, respectively.

The block diagram of the equivalent discrete-time model (discretized at 1 Hz) is depicted in Figure 5.11. Even if the loop structure looks different from the one shown in Figure 5.8, the control loop acts in the very same way. The equivalence between the system considered and a classic SC is demonstrated in the following.

Let $\tau_m(k)$ and $\tau_c(k)$ be the periods of PPS signals at the input (i.e. the reference) and at the output of the SC, respectively, at the k-th second. The synchronization error $e(k)$, can be obtained by accumulating the difference between periods $\tau_m(k)$ and $\tau_c(k)$.

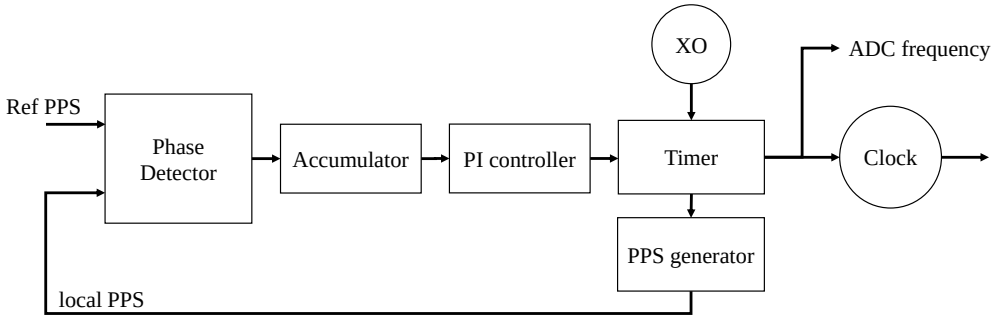

FIGURE 5.10: Architecture of the SC implemented on the PRU of the BBB. (from [192] with permissions)

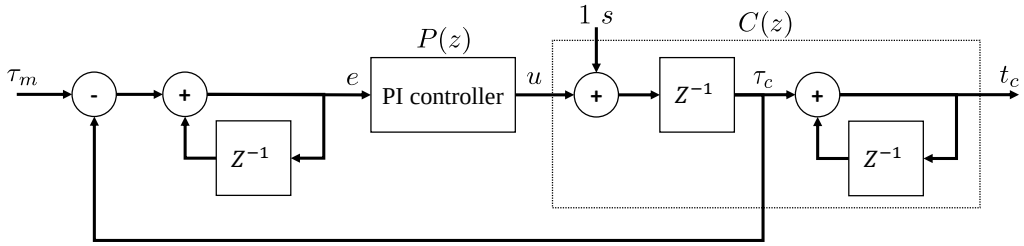

FIGURE 5.11: Model of the servo clock as implemented on the BBB. (from [192] with permissions)

In fact, since

$$\tau_m(k) = t_m(k) - t_m(k-1) + \nu(k) \tag{5.7}$$

$$\tau_c(k) = t_c(k) - t_c(k-1) \tag{5.8}$$

the error can be expressed equivalently as:

$$e(k) = t_m(k) - t_c(k) + \sum_{i=0}^{k} \nu(i). \tag{5.9}$$

This expression can be rearranged recursively as:

$$e(k) = e(k-1) + \tau_m(k) - \tau_c(k). \tag{5.10}$$

To correctly take care of the jitter η, the analysis is performed using the resolution of the servo clock as $1/f_{XO}$ with $f_{XO} = 200\,\text{MHz}$ (which is the clock frequency of the PRU where the SC is implemented). For this analysis, the sampling frequency of the ADC is set to $f_{OUT} = 8\,\text{kHz}$. This choice results from the previous considerations on the processing capability of the BBB.
Actually, this may change for the PMU working on 60 Hz power systems, while, for instance, in the OpenPMU the sampling rates were set to 12.8 kHz and 15.36 kHz due to the need of collecting 256 sample per nominal power line cycle in 50 Hz and 60 Hz, respectively.

PI controller design

The number of ticks for each period of the sampling signal is $n_t = f_{XO}/f_{OUT} = 25000$ ticks. In practice, the actual number of ticks is different because f_{XO} is affected by offset and frequency fluctuations (as customary for quartz oscillators). The dynamic of the output frequency f_c of the SC is:

$$f_c(k+1) = f_{OUT}(1+\alpha) + b\eta(k) + bu(k) \tag{5.11}$$

where $b = 1/n_t$, α is the relative frequency offset of the XO, $\eta(k)$ is the jitter fo the SC accumulated in 1 s and $u(k)$ is the controller output, as shown in Figure 5.11. It is clear that f_c is derived from the control action, dividing it by the number of ticks n_t, and it is affected by both η and ν (actually included in the term $u(k)$). The control is realized as:

$$u(k+1) = u(k) + K_P(e(k+1) - e(k)) + K_I e(k+1). \tag{5.12}$$

Of course, $e(\cdot)$ depends on τ_m and τ_c, because:

$$\tau_m(k) = n_t f_{OUT} + \nu(k)$$
$$\tau_c(k) = n_t f_c(k)$$

where, like before, jitter $\nu(k)$ is accumulated over 1 s.

It is now possible to define a state space realization of the system, introducing the vector $q(k) = [e(k), f_c(k), u(k)]$ of the state variables of the closed-loop system. In this way it is possible to write:

$$q(k+1) = Aq(k) + G\tau_{m_q}(k) + C\eta(k) + Ff_0, \tag{5.13}$$

where

$$A = \begin{bmatrix} 1 & -n_t & 0 \\ bK_I & -(K_P+K_I) & b \\ K_I & -n_t(K_P+K_I) & 1 \end{bmatrix}, \quad G = \begin{bmatrix} 1 \\ b(K_P+K_I) \\ K_P+K_I \end{bmatrix},$$

$$C = \begin{bmatrix} 0 \\ b \\ 0 \end{bmatrix} \quad \text{and} \quad F = \begin{bmatrix} 0 \\ (1+\alpha) \\ 0 \end{bmatrix}.$$

Then, assuming that $\nu(k) \sim \mathcal{N}(0, \sigma_\nu^2)$ and $\eta(k) \sim \mathcal{N}(0, \sigma_\eta^2)$, the covariance matrix of $q(k+1)$ is:

$$Q(k+1) = AQ(k)A^T + GG^T\sigma_\nu^2 + CC^T\sigma_\eta^2. \tag{5.14}$$

Note that this equation holds only if processes $\nu(k)$ and $\eta(k)$ are white. This assumption is actually strong for the case analyzed, as the phase and frequency noises affecting clocks usually are not only white (further details are reported, for reference, in the Appendix C). However, to a first approximation, over short periods, jitter affecting digital clock signals is mainly determined by white noise [194].

If the values of the PI parameters make the system stable (equation (5.5) and (5.6)), the covariance matrix (5.14) reaches a steady-state equilibrium. This means that after a sufficiently large number of iterations $\bar{k}$, $Q(k+1) = Q(k)$, $\forall k > \bar{k}$. Noting that the variance of the time synchronization fluctuations is the element (1,1) of $Q(k)$, it follows from (5.14) that when the steady state is reached:

$$\sigma_e^2 = \mathbb{E}\{(e(k) - \mathbb{E}\{e(k)\})^2\} = \frac{2(\sigma_\nu^2 + \sigma_\eta^2)}{K_P(4 - K_I - 2K_P)}. \tag{5.15}$$

Similarly, the variance of the clock rate fluctuations in steady-state conditions is:

$$\sigma_{f_c}^2 = b^2 \frac{\sigma_\eta^2(2K_I + 4K_P) + \sigma_\nu^2(2K_I + 2K_P^2 + K_IK_P)}{K_P(4 - K_I - 2K_P)} \tag{5.16}$$

The three-dimensional plots of (5.15) and (5.16) as a function of K_P and K_I are depicted in Figures 5.12-(a) and 5.12-(b), respectively . It is clear that to minimize the

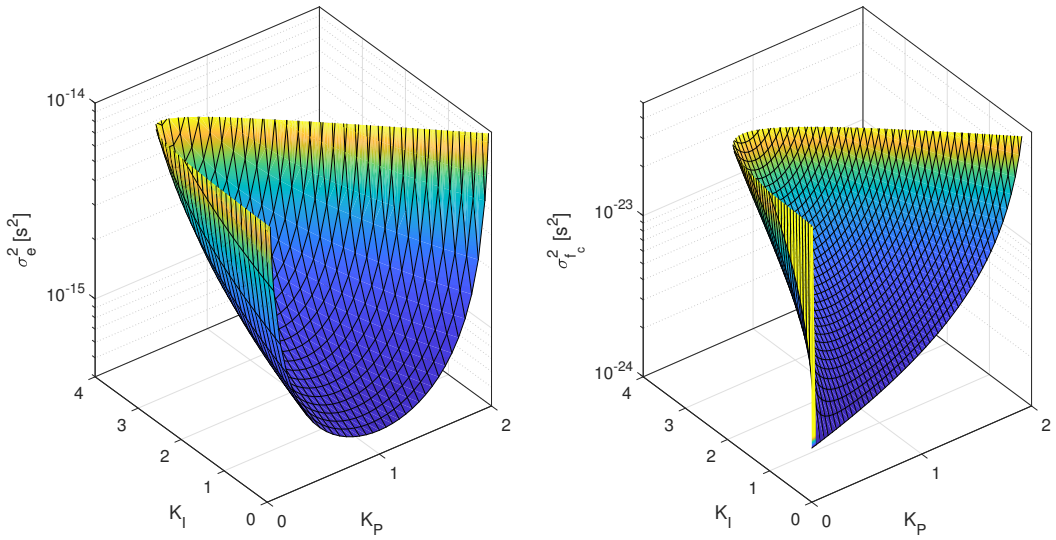

FIGURE 5.12: Surface plot of the variances given by equations (5.15) on the left, and (5.16) on the right, as function of the parameters K_P and K_I.

time synchronization uncertainties, the optimal values are $K_P = 1$ and K_I as small as possible, yet greater than zero due to the stability constraint of equations (5.6). On the other hand, to minimize the syntonization uncertainty, K_P should be smaller than 1. However, the requirement of minimizing syntonization uncertainty is less urgent because the main purpose of the SC is indeed time synchronization. It worth emphasizing that the trends of the surface plots are independent of the variances of ν and η.

5.3.3 Experimental results

To check the consistency between the SC model and the actual BBB implementation and to assess the performance of the latter, some laboratory tests have been performed. All the tests rely on a Meinberg M600-PTP master clock as reference. The rated performance of the master clock, equipped with the internal standard quality Oven Controlled Crystal Oscillator (OCXO), are reported also in Table 5.2 [195]. Using the specified phase noise it was estimated that the standard deviation of the period of the PPS signal used as reference is about 30 ns. However, this is about one order of magnitude smaller over short intervals (up to few hours), as the effect of the white phase noise is the most significant contribution. This is an important assumption, as the optimization previously made relies on a model with white noise only. The PPS period offset between the input reference and the SC signal were

measured through a digital storage oscilloscope (DSO) Agilent DSO7032A disciplined by the Master clock.

In free running conditions (i.e. open-loop) the average frequency offset of the PPS signal generated by the SC is about -82 ppm with respect to the master clock reference. The standard deviation of the period fluctuations in open-loop conditions ranges from 25 ns over 2-hour observation interval, till about 120 ns over two days. This big difference further highlights how the low-frequency power-law noise contributions (Flicker PM, White FM, Flicker FM and random walk) tend to prevail over the white phase noise in the long term.

TABLE 5.2: Performance of the Meinberg M600 equipped with standard quality OCXO [195].

Short term stability (τ=1 sec)	5×10^{-12}
accuracy of PPS	$< \pm$ 50 ns
phase noise	1 Hz < -85 dBc/Hz 10 Hz < -115 dBc/Hz 100 Hz < -130 dBc/Hz 1 kHz < -140 dBc/Hz
accuracy GPS-sync 1 day average	$\pm\, 1 \times 10^{-12}$

SC model validation

The validity of the theoretical analysis, which led to equations (5.15) and (5.16), was confirmed by several experimental results. In particular, the values of σ_e in steady-state conditions were experimentally estimated on the BBB SC implementation using some pairs of K_P and K_I values within the stability region of the SC. Running the SC for 1-hour interval, after the transient expires, the jitter of the SC with respect to the reference was measured. The standard deviations values of such time fluctuations (corresponding to some slices of the surfaces of Figure 5.12(a) for $K_I = \{0.05,\ 0.1,\ 0.5,\ 1\}$ and for K_P ranging from 0.1 and 1.6) are shown in figure 5.13.

The experimental curves are generally consistent with the theoretical results and clearly confirm the position of the minimum of σ_e when $K_P = 1$ and $K_I = \varepsilon > 0$. However, for $K_I < 0.05$ the jitter reduction becomes negligible. Actually this effect is not imputable to hardware limits, as also in simulation the jitter obtained with

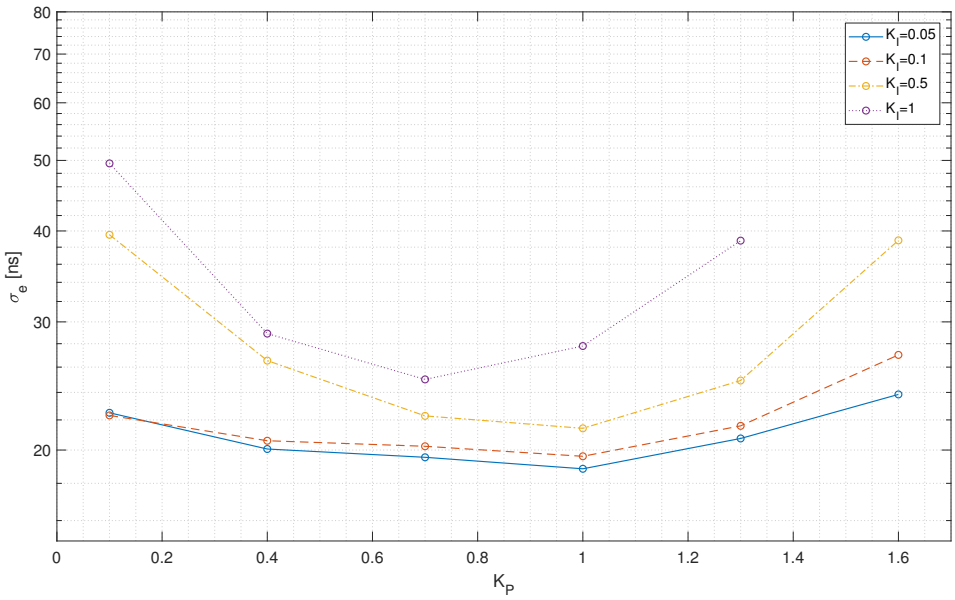

FIGURE 5.13: Experimental values of standard deviation of the synchronization errors for different values of the controller parameters K_P and K_I.

$K_P = 1$ and $K_I < 0.1$ seems to converge to $\sigma_e \approx 20\,\text{ns}$. However, choosing values of K_I excessively small is not advisable because of the higher convergence times of the controller, resulting in a longer transient, if some anomalous events occur.

SC performances

After validating the correct behavior of the controller design criteria, some experiments on the implementation were performed to assess the stability of the servo clock.

The long term stability of the SC is determined using the Allan deviation (actually the square root of (C.5)) of the generated PPS signal over about two days, with no dead-time between measurements. The experiment was repeated for different values of K_P and K_I. The controllers chosen to perform this analysis are:

1. A dead-beat controller (i.e. $K_P = K_I = 1$) that is chosen for its fast response, albeit the jitter reduction with this controller is not the best;
2. A proportional-only controller with unit gain (i.e. $K_P = 1$ and $K_I = 0$);
3. Finally, a quasi-optimal controller with $K_P = 1$ and $K_I = 0.05$ for the reasons explained above.

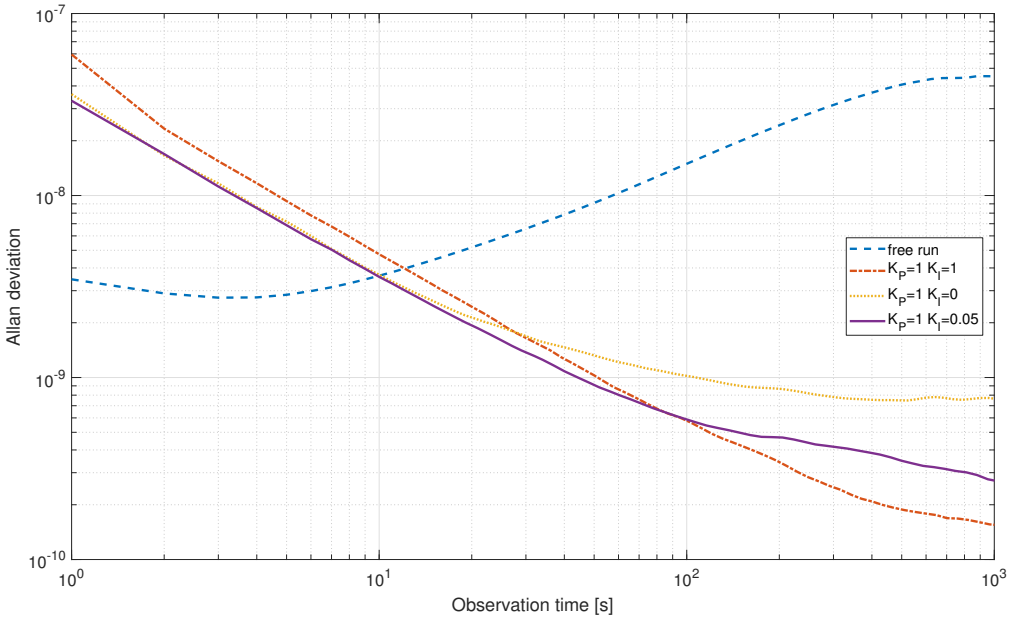

FIGURE 5.14: Allan deviation plots obtained from the PPS signals for different control laws as in the legend. For comparison, also the Allan deviation of the free-running clock is shown.

The resulting Allan deviation curves are shown in Figure 5.14. For reference, also the Allan deviation curve in free running conditions is shown.

The open-loop short-term Allan deviation of the SC (i.e. over 1 s) is approximately 3.4×10^{-9} and then degrades over longer periods, as customary for low-quality oscillators. Of course, with a control loop, the drift due to the frequency offset is compensated and reduced to less than 0.1 ppm. However, a slightly worse open-loop short-term stability is visible, in particular for the dead-beat controller, which is the controller with the fastest transient response. The purely proportional controller, on the other hand, performs slightly worse at the right side of the plot, probably because of the reduced filtering effect with respect to the other controllers. The controller with $K_P = 1$ and $K_I = 0.05$ exhibits a good trade-off between long-term stability and short-term noise reduction.

Finally, Figure 5.15 shows the histograms of the PPS period fluctuations for all of the three controllers considered. The jitter measured in the case of dead-beat controller is almost double of the jitter of the PI with $K_P = 1$ and $K_I = 0.05$. In the case of the unity-gain controller instead, such a difference, although present, is not clearly visible in the short term, in accordance with the results of Figure 5.14.

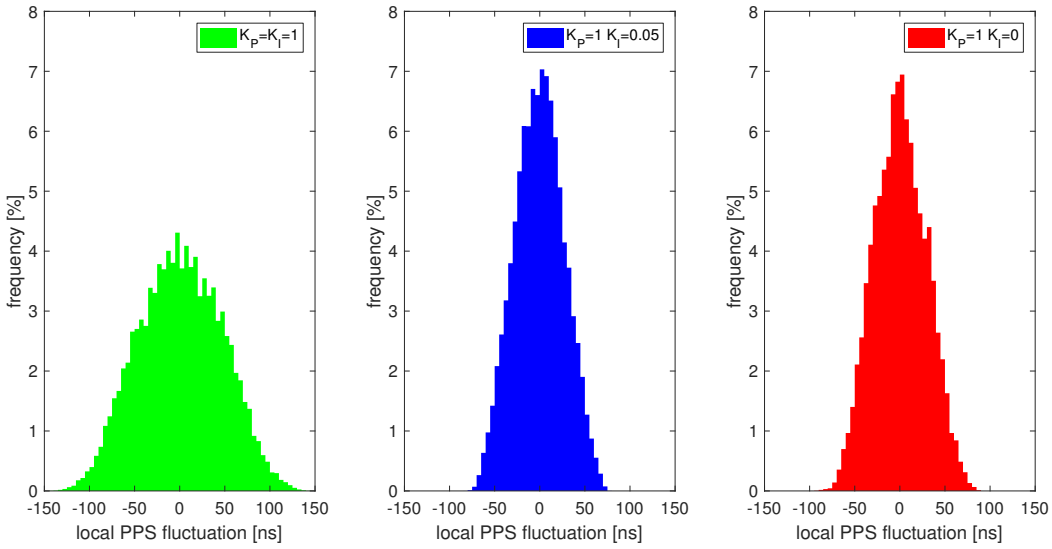

(a) (b) (c)

FIGURE 5.15: Histograms of the PPS period fluctuations generated by the SC, using different controllers, i.e. in (a) the the dead-beat, in (b) the quasi-optimal controller with $K_P = 1$ and $K_I = 0.05$ and in (c) the unity-gain controller. All the plot are normalized on the percent probability.

CHAPTER 6

Conclusion

The work presented in this dissertation is focused on the implementation of an affordable Phasor Measurement Unit prototype to enable an extensive PMU deployment in distribution systems. The need for this instrument is driven by the requirements of Active Distribution Networks (ADNs), enabling a smarter integration of distributed energy resources in a smart grid. In this respect, many problems related to data management and communication in the smart grid can be partially tackled taking advantage of the Internet of Things (IoT) paradigm.

The first chapter, is an overview of some achievements in IoT implemented devices, including some state-of-the-art solutions for reducing power consumptions of networked embedded systems. Among these, the wake-up radio technology is discussed and presented by means of a couple of design examples, including an application for improving efficiency of power line communication modems for smart street lighting.

Then, approaching the main topic of PMU implementation, some different aspects concerning the main implementation issues have been analyzed.
First, a testbed conceived to evaluate and compare the algorithms estimation uncertainties is presented. The components of this testbed have been characterized in order to measure the RMS value of the overall noise floor affecting synchrophasor, frequency, and ROCOF estimation. To this purpose, a suitable noise propagation model has been validated.
The methodology presented is general, and it can be applied even if different hardware is used. In fact, the components that affect PMU measurement uncertainties are always *(i)* voltage transducers, *(ii)* data acquisition module, and *(iii)* synchronization module.

Multiple experiments and simulations show that by using broadband transducer introducing low nonlinear distortion, the mismatch between simulation and measurement results in different testing conditions is very small on average, i.e. 0.012 % for TVE, 0.6 mHz for FE and 0.07 Hz/s for RFE, respectively. Such results confirm the validity of the proposed model. However, the comparison between measurement and simulation-based results in ideal (i.e. noiseless) conditions suggests that the accuracy limits of the whole testbed for synchrophasor, frequency, and ROCOF measurements are roughly twice as large, i.e. TVE $\approx$ 0.02 %, FE $\approx$ 1.5 mHz and RFE $\approx$ 0.2 Hz/s.
This work also highlights the major difficulties in producing a PMU with high performance, able to meet the accuracy requirements of an ADN. Since ADNs generally demand a high number of measurement points, reducing the cost of measurement devices is essential for ADN evolution. To this aim, a low-cost embedded platform was chosen to build a PMU. The synchrophasor estimation algorithm is obviously the most computationally intensive task for a PMU, which, in addition, has to deliver data in real-time at 50 to 60 fps. The platform chosen for prototyping is a Beaglebone Black (BBB), which has been also adopted in the OpenPMU project as well. This SBC, in fact, it is cheap and well suits the needs to acquire and process data in real-time. In fact, the problem of the limited computational capability of its processor is addressed with the development of a tailored lightweight estimation algorithm. The proposed algorithm results from the tailored combination and optimization of two state-of-the-art algorithms, i.e. an IpDFT along with a preliminary bandpass filter and a real-valued TFT. The IpDFT is used only to estimate the fundamental static off-nominal frequency deviation, which in turn is used to tune the coefficients of the TFT matrix. The TFT stage, which instead uses unfiltered data, is implemented using a flexible number of harmonic terms which decrease with the observation interval length. The algorithm, implemented on the Beaglebone Black board, is able to return estimates at reporting rates compliant with the mandatory requirements of the IEEE Standard C37.118.1-2011 when the sampling frequency is 8 kHz. The experimental data obtained using the PMU testbed described in Chapter 3 show good compliance with most of the P class and M class requirements specified in the IEEE Standard C37.118.1-2011 and the Amendment C37.118.1a-2014, although different transducers can unpredictably affect measurement results. Phase estimation accuracy is smaller than 1 mrad in most testing conditions, which is very important for ADN monitoring.

One of the key advantages of the BBB is the presence of two coprocessors called Programmable Real-time Units (PRUs) which transfer data from the ADC to the processing buffer in real-time. To this aim, a Servo Clock (SC) was implemented

using one PRU of the BBB with the purpose of disciplining the data acquisition stage of the PMU and to timestamp measurement results, once the PRU timer is properly initialized to the UTC and driven by an input reference pulse-per-second (PPS) signal. This PPS signal could be provided by a common master clock shared among multiple PMUs within the same substation. Various experimental results shown consistency with the theoretical model of the SC and highlight its correct operations. The SC is based on a PI controller optimized in order to minimize the standard deviation of the short-term time synchronization error in steady-state conditions. The SC has been developed in the context of the OpenPMU project, as it was used to generate the sampling signal of the ADC for PMU data acquisition and communication.

The resulting instrument is then a good candidate for implementing a PMU for monitoring the future distribution grid, enabling a smarter integration of distributed energy resources in a smart grid.
In this respect, the IoT paradigm helps to tackle some problems of the future grid. For instance, future IoT devices are expected to integrate machine learning algorithms, for more sophisticated diagnostic operations. Where before there was only a sensing device, nowadays there is the possibility to perform a preprocessing step and many operations, demanding to the cloud only to store data and to further perform analysis on the resulting *"big data"*.
This approach will be successfully embraced in Industrial IoT applications as well, that will become smarter, thanks to the access to high performance and distributed processing platforms. In the smart grid domain, this revolution can be declined in different ways. Smarter energy meters (which are already widely deployed) are other well-known examples. Thanks to cheaper and high-performance platforms, a low-cost embedded PMU implementation meeting distribution systems requirements is possible as well.

APPENDIX A

Sine fit algorithm

With the aim of testing the performance of digitizers and signal generators, some parameters are usually calculated, most commonly:

1. **NAD**, noise and distortion
2. **SINAD**, signal to noise and distortion ratio
3. **THD**, total harmonic distortion
4. **ENOB**, effective number of bits
5. **DC offset**
6. **SNR**, signal to noise ratio.

The sine fit (SF) method can be used to calculate many of these parameters, analyzing the residuals and the output parameters. The sine-fit algorithm described in the following is basically equal to the one proposed by the IEEE Standard 1057-2017 [129].

Let a pure sinewave be acquired by a digitizer, producing a set of M points organized in the vector x with a sample rate f_s. The digitized signal can be approximated by:

$$\tilde{x}(n) = \alpha \cos(2\pi f t_n) + \beta \sin(2\pi f t_n) + \gamma \tag{A.1}$$

where t_n represents the time at which the n-th sample is acquired.
The four parameters to be calculated through the fit algorithm are α, β, γ and f. The SF algorithm aims at iteratively find an approximate solution that, at the iteration i-th, minimizes the sum of the squared differences:

$$\sum_{n=1}^{M} \left[x(n) - \alpha_i \cos(2\pi f_i t_n) - \beta_i \sin(2\pi f_i t_n) - \gamma_i\right]^2 \tag{A.2}$$

In the case of three-parameters SF, the frequency of the signal f is already given and does not take part to the fitting algorithm. Otherwise, for the four-parameters SF, the first guess f_0 has to be initially estimated. A DFT, or its interpolated variant, can be effectively used to this aim. Then the Standard suggests the use of a first pre-fit with the three-parameters algorithm for the first guess of the parameters α_0, β_0 and γ_0.

Then, at each iteration i, the following matrix is calculated:

$$D_i = \begin{bmatrix} \cos(2\pi f_i t_1) & \sin(2\pi f_i t_1) & 1 & -\alpha_{i-1} t_1 \sin(2\pi f_i t_1) + \beta_{i-1} t_1 \cos(2\pi f_i t_1) \\ \cos(2\pi f_i t_2) & \sin(2\pi f_i t_2) & 1 & -\alpha_{i-1} t_2 \sin(2\pi f_i t_2) + \beta_{i-1} t_1 \cos(2\pi f_i t_2) \\ \vdots & \vdots & \vdots & \vdots \\ \cos(2\pi f_i t_M) & \sin(2\pi f_i t_M) & 1 & -\alpha_{i-1} t_M \sin(2\pi f_i t_M) + \beta_{i-1} t_1 \cos(2\pi f_i t_M) \end{bmatrix}.$$

Organizing the parameters in the column vector

$$s_i = \begin{bmatrix} \alpha_i \\ \beta_i \\ \gamma_i \\ \Delta f_i \end{bmatrix}$$

the least square (LS) solution can be expressed as:

$$\hat{s}_i = \left(D_i^T D_i\right)^{-1} \left(D_i^T x\right)$$

and the frequency is updated as

$$f_i = f_{i-1} + \Delta f_{i-1} \quad (\text{with } \Delta f_0 = 0).$$

The calculation of the D matrix and the LS solution are computed iteratively until a proper convergence is achieved, e.g. expression (A.2) is small enough.

Eventually, the signal can be expressed as:

$$\begin{aligned}\tilde{x}(n) &= \sqrt{\alpha_i^2 + \beta_i^2} \cdot \cos\left(2\pi f_i t_n + \arctan(-\beta_i/\alpha_i)\right) + \gamma_i \\ &= A \cdot \cos\left(2\pi f t_n + \varphi\right) + \gamma\end{aligned}$$

with A, φ, f and γ being the amplitude, phase, frequency and DC offset estimations of the sinewave, respectively. The residuals are:

$$\varepsilon(n) = x(n) - \tilde{x}(n)$$

Using the residuals ε, the noise and distortion (NAD) and, in turn, the signal to noise and distortion (SINAD) are defined as:

$$NAD = \sqrt{\frac{1}{M}\sum_{n=1}^{M}\left[\varepsilon(n)\right]^2} \tag{A.3}$$

$$SINAD = \frac{A_{rms}}{NAD} \tag{A.4}$$

where A_{rms} is the RMS of the signal, equal to the peak amplitude of the fitted sinewave divided by $\sqrt{2}$.

The RMS of noise η and the respective signal to noise ratio (SNR) are finally given by:

$$\eta = \sqrt{NAD^2 - A_{rms}^2 THD^2} \tag{A.5}$$

$$SNR = \frac{A_{rms}}{\eta} \tag{A.6}$$

APPENDIX B

Window functions

Recalling equation (4.3), the windowed DFT can be written as:

$$X_w(\lambda) = \sum_{n=-\frac{N-1}{2}}^{\frac{N-1}{2}} w[n]\, x[n]\, e^{-j2\pi\frac{\lambda n}{N}}, \quad \lambda = 0, \ldots, N-1.$$

To enhance the spectral accuracy of a DFT estimator is common to window the input data with a proper window function [196], [197]. Many types of windows are already known and discussed in literature, but in many cases, cosine-class windows are used. The general expression for a cosine-class window is:

$$w[n] = \sum_{k=0}^{K-1} a_k \cdot \cos\left(\frac{2\pi k}{N} n\right), \quad n = -\frac{N-1}{2}, \ldots, \frac{N-1}{2} \tag{B.1}$$

where a_k are the parameters that define the shape of the window and K is the number of terms of the window. It is worth defining also the DFT of the window, i.e.:

$$W(k) = \frac{1}{N} \sum_{n=-\frac{N-1}{2}}^{\frac{N-1}{2}} w[n]\, e^{-j2\pi\frac{kn}{N}} \tag{B.2}$$

The rectangular window is simply the 1-term window with $a_0 = 1$. Other common cosine-class windows (usually taking the name from the scientist who proposed it) are listed in the following Table B.1.

The difference between them can be seen in Figure B.1 where the frequency response is plotted. Note the difference between them. Some useful parameters to compare windows are the -3 dB bandwidth of the main lobe and the maximum

TABLE B.1: Common cosine windows and relative parameters

Type of window	terms (K)	parameters a_k
Rectangular	1	$a_0 = 1$
Hamming	2	$a_0 = 0.5,\ a_1 = 0.5$
Hann	2	$a_0 = 0.54,\ a_1 = 0.46$
Blackman	3	$a_0 = 0.42,\ a_1 = 0.5,\ a_2 = 0.08$
Nuttal	4	$a_0 = 0.355\, a_1 = 0.487,\ a_2 = 0.144,\ a_3 = 0.01$
Maximally flat	5	$a_0 = 1\, a_1 = 1.93,\ a_2 = 1.29,\ a_3 = 0.388,\ a_4 = 0.032$

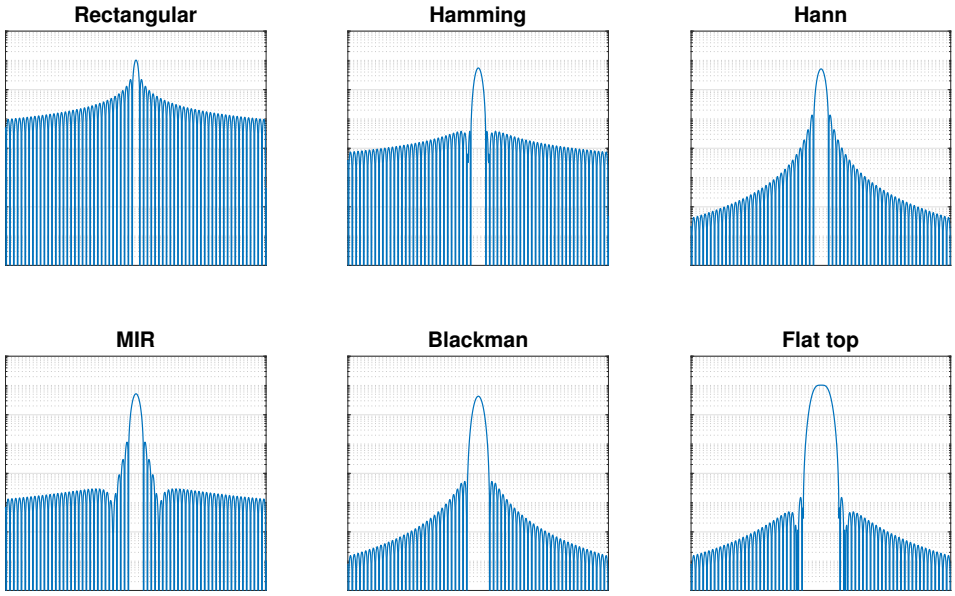

FIGURE B.1: Frequency response (DFT) of some windows described in Table B.1

relative magnitude of the spectral side lobes with respect of the main one. Other parameters that carachterize windows are the *Normalized Peak Signal Gain*, the *Normalized Noise Power Gain* and the *Equivalent Noise Bandwidth* [159].

Other windows, based on different functions than cosine, can be developed. For instance, the Maximum Image Rejection (MIR) window in [137] was used for its properties to implement algorithms of this thesis. The MIR window sequence over C cycles is given by:

$$w[n] = \frac{4C^2}{8C^2 - 1} + \frac{4C^2 - 1}{8C^2 - 1} \cos\left(\frac{2\pi}{N} n\right) . \tag{B.3}$$

It is a two-terms window, that tends to approximately cancel the image component of a spectral peak located at frequency bin C. Other higher-order windows can be better in terms of side lobe decay but, having a large main lobe, the spectral leakage

can negatively influence the phasor estimation, unless a suitably large number of cycles is observed.

APPENDIX C

Frequency stability analysis

In order to further understand the measurements on the SC, some basic notions on clock stability and measurement are given in the following. The component that provides a time reference to every electronic device is an oscillator, usually crystal oscillator (XO). The stability of the frequency generated by such an oscillator is usually affected by a number of phenomena and all of them can be measured in various ways. The one-sided power spectral density (PSD) function of the random phase fluctuation $\varphi(t)$ is denoted as $S_\varphi(f)$. Sometimes oscillators manufacturers use the two-sided PSD $\mathcal{L}(f)$ which is defined as:

$$\mathcal{L}(f) = \frac{1}{2} S_\varphi(f)$$

and is given in dBc/Hz, therefore $\mathcal{L}(f)$ is 3 dB smaller than $S_\varphi(f)$. The unit dBc/Hz stands for *"decibel below the carrier in a 1 Hz bandwidth"* [198], but its definition is quite old and obsolete.

Similarly, it is possible to use frequency $\nu(t)$ instead of phase. Since fractional frequency fluctuation is given by:

$$y(t) = \frac{\dot{\varphi}(t)}{\omega_0} = \frac{(\nu(t) - \nu_0)}{\nu_0} \tag{C.1}$$

where ω_0 is the carrier nominal angular frequency; the associated PSD can be written as:

$$S_y(f) = \frac{f^2}{\nu_0^2} S_\varphi(f). \tag{C.2}$$

The classic model describing the phase noise PSD is the so called power-law model:

$$S_\varphi(f) = \sum_{i=-4}^{0} \beta_i f^i$$

which, using $S_y(f)$, can be written as:

$$S_y(f) = \sum_{i=-2}^{2} \alpha_i f^i$$

where coefficients β and α are related to one another as shown in Table C.1 [133].

In the time domain, the instrument commonly used to measure period or frequency of periodic signals is the universal counter. It measures a frequency $\hat{v}_k(\tau)$ over an interval of duration τ. Then the measure is usually converted into a relative frequency deviation y using (C.1). In this way, given N samples of $\hat{y}(\tau)$ the variance is:

$$\sigma_y^2 = \frac{1}{N-1} \sum_{k=1}^{N} [\hat{y}_k - \langle \hat{y} \rangle_N]^2 \tag{C.3}$$

Unfortunately, when applied to a periodic signal from an oscillator, (C.3) converges only for white phase noise, flicker phase noise and white frequency noise, while for flicker frequency or random walk the variance depends on N and τ. Moreover it is affected by a bias growing with the measurement interval length. The Allan variance (AVAR) has been developed to overcome these problems. It is defined as one half of the the average of the squares of the differences between successive readings $\hat{y}$. The definition of the Allan variance is also given by [199]:

TABLE C.1: Power-law parameters of S_φ and S_y with respective noise processes.

Noise process	$S_\varphi(f)$	$S_y(f)$
White PM	β_0	$\alpha_2 f^2$
Flicker PM	$\beta_{-1} f^{-1}$	$\alpha_1 f^2$
White FM	$\beta_{-2} f^{-2}$	α_0
Flicker FM	$\beta_{-3} f^{-3}$	$\alpha_{-1} f^{-1}$
Random walk FM	$\beta_{-4} f^{-4}$	$\alpha_{-2} f^{-2}$
linear frequency drift		

$$\sigma_y^2(\tau) = \mathbb{E}\left\{\frac{1}{2}\left[\hat{y}_{k+1} - \hat{y}_k\right]^2\right\} \tag{C.4}$$

It is assumed that there is no dead time between measurements, i.e. the samples $\hat{y}_k$ are contiguous in time. In the practice the statistical expectation estimator is the arithmetic average (with the assumption of ergodic process), thus the AVAR results from:

$$\hat{\sigma}_y^2(\tau) = \frac{1}{2(M-1)} \sum_{k=1}^{M-1} (\hat{y}_{k+1} - \hat{y}_k)^2 \tag{C.5}$$

The Allan variance is used for evaluating the stability of oscillators and clocks. However, sometimes the phase or frequency noise are preferably reported in the frequency domain.
It is possible to compute Allan variance from PSDs by using the following expression [133]:

$$\sigma_y^2(\tau) = \int_0^\infty S_y(f) \cdot 2\frac{\sin^4(\pi\tau f)}{(\pi\tau f)^2}\, \mathrm{d}f.$$

Several other statistical tools can be used to characterize the fluctuations of a frequency source, for instance by using the Modified Allan variance (MVAR) it is possible to discriminate between white and flicker phase noise [200].

Bibliography

[1] *A European strategy for smart, sustainable and inclusive growth*. [Online]. Available: http://ec.europa.eu/eu2020/pdf/COMPLET%20EN%20BARROSO%20%20%20007%20-%20Europe%202020%20-%20EN%20version.pdf.

[2] *Europe 2030 Energy Strategy*. [Online]. Available: https://ec.europa.eu/energy/en/topics/energy-strategy-and-energy-union/2030-energy-strategy.

[3] S. P. Mohanty, U. Choppali, and E. Kougianos, "Everything you wanted to know about smart cities: The internet of things is the backbone", *IEEE Consumer Electronics Magazine*, vol. 5, no. 3, pp. 60–70, 2016. DOI: 10.1109/mce.2016.2556879.

[4] H. Lund, P. A. Østergaard, D. Connolly, and B. V. Mathiesen, "Smart energy and smart energy systems", *Energy*, vol. 137, pp. 556–565, 2017. DOI: 10.1016/j.energy.2017.05.123.

[5] G. Andreottola, A. Bogomolov, A. Borghetti, D. Brunelli, A. Conti, C. D. Tonno, D. Macii, P. Merkus, C. A. Nucci, G. Panarelli, D. Ragazzi, G. Trombino, and H. V. Zonneveld, "Energy systems for smart cities - white papers from the ieee smart cities inaugural workshop, december 2014 in trento, italy.", en, 2014. DOI: 10.13140/rg.2.1.4732.6168.

[6] F. Causone, A. Sangalli, L. Pagliano, and S. Carlucci, "An exergy analysis for milano smart city", *Energy Procedia*, vol. 111, pp. 867–876, 2017. DOI: 10.1016/j.egypro.2017.03.249.

[7] L. Mehigan, J. Deane, B. Gallachóir, and V. Bertsch, "A review of the role of distributed generation (DG) in future electricity systems", *Energy*, vol. 163, pp. 822–836, 2018. DOI: 10.1016/j.energy.2018.08.022.

[8] J. Pan, R. Jain, S. Paul, T. Vu, A. Saifullah, and M. Sha, "An internet of things framework for smart energy in buildings: Designs, prototype, and experiments", *IEEE Internet of Things Journal*, vol. 2, no. 6, pp. 527–537, 2015. DOI: 10.1109/jiot.2015.2413397.

[9] A. Zanella, N. Bui, A. Castellani, L. Vangelista, and M. Zorzi, "Internet of things for smart cities", *IEEE Internet of Things Journal*, vol. 1, no. 1, pp. 22–32, 2014, ISSN: 2327-4662. DOI: 10.1109/JIOT.2014.2306328.

[10] W. Ejaz, M. Naeem, A. Shahid, A. Anpalagan, and M. Jo, "Efficient energy management for the internet of things in smart cities", *IEEE Communications Magazine*, vol. 55, no. 1, pp. 84–91, 2017, ISSN: 0163-6804. DOI: 10.1109/MCOM.2017.1600218CM.

[11] R. Want, B. N. Schilit, and S. Jenson, "Enabling the internet of things", *Computer*, vol. 48, no. 1, pp. 28–35, 2015, ISSN: 0018-9162. DOI: 10.1109/MC.2015.12.

[12] M. A. Razzaque, M. Milojevic-Jevric, A. Palade, and S. Clarke, "Middleware for internet of things: A survey", *IEEE Internet of Things Journal*, vol. 3, no. 1, pp. 70–95, 2016, ISSN: 2327-4662. DOI: 10.1109/JIOT.2015.2498900.

[13] L. Casals, B. Mir, R. Vidal, and C. Gomez, "Modeling the energy performance of lorawan", *Sensors*, vol. 17, no. 10, 2017, ISSN: 1424-8220. DOI: 10.3390/s17102364.

[14] K. Mekki, E. Bajic, F. Chaxel, and F. Meyer, "A comparative study of lpwan technologies for large-scale iot deployment", *ICT Express*, 2018, ISSN: 2405-9595. DOI: https://doi.org/10.1016/j.icte.2017.12.005.

[15] F. Adelantado, X. Vilajosana, P. Tuset-Peiro, B. Martinez, J. Melia-Segui, and T. Watteyne, "Understanding the limits of lorawan", *IEEE Communications Magazine*, vol. 55, no. 9, pp. 34–40, 2017, ISSN: 0163-6804. DOI: 10.1109/MCOM.2017.1600613.

[16] U. Raza, P. Kulkarni, and M. Sooriyabandara, "Low power wide area networks: An overview", *IEEE Communications Surveys Tutorials*, vol. 19, no. 2, pp. 855–873, 2017, ISSN: 1553-877X. DOI: 10.1109/COMST.2017.2652320.

[17] D. Balsamo, A. S. Weddell, G. V. Merrett, B. M. Al-Hashimi, D. Brunelli, and L. Benini, "Hibernus: Sustaining computation during intermittent supply for energy-harvesting systems", *IEEE Embedded Systems Letters*, vol. 7, no. 1, pp. 15–18, 2015, ISSN: 1943-0663. DOI: 10.1109/LES.2014.2371494.

[18] X. Sun and N. Ansari, "Edgeiot: Mobile edge computing for the internet of things", *IEEE Communications Magazine*, vol. 54, no. 12, pp. 22–29, 2016, ISSN: 0163-6804. DOI: 10.1109/MCOM.2016.1600492CM.

[19] J. Lin, W. Yu, N. Zhang, X. Yang, H. Zhang, and W. Zhao, "A survey on internet of things: Architecture, enabling technologies, security and privacy, and applications", *IEEE Internet of Things Journal*, vol. 4, no. 5, pp. 1125–1142, 2017, ISSN: 2327-4662. DOI: 10.1109/JIOT.2017.2683200.

[20] *WHO releases country estimates on air pollution exposure and health impact*. [Online]. Available: http://www.who.int/mediacentre/news/releases/2016/air-pollution-estimates/en/.

[21] M. Deepa, M. Rajalakshmi, and R. Nedunchezhian, "Impact of air pollution on respiratory diseases: Correlation and classification by multivariate data analysis", *Data-Enabled Discovery and Applications*, vol. 1, no. 1, 2017. DOI: 10.1007/s41688-017-0004-z.

[22] M. Bacco, F. Delmastro, E. Ferro, and A. Gotta, "Environmental monitoring for smart cities", *IEEE Sensors Journal*, vol. 17, no. 23, pp. 7767–7774, 2017. DOI: 10.1109/jsen.2017.2722819.

[23] K. Hu, V. Sivaraman, B. G. Luxan, and A. Rahman, "Design and evaluation of a metropolitan air pollution sensing system", *IEEE Sensors Journal*, vol. 16, no. 5, pp. 1448–1459, 2016. DOI: 10.1109/jsen.2015.2499308.

[24] L.-J. Chen, Y.-H. Ho, H.-C. Lee, H.-C. Wu, H.-M. Liu, H.-H. Hsieh, Y.-T. Huang, and S.-C. C. Lung, "An open framework for participatory PM2.5

monitoring in smart cities", *IEEE Access*, vol. 5, pp. 14 441–14 454, 2017. DOI: 10.1109/access.2017.2723919.

[25] X. Li, E. Iervolino, F. Santagata, J. Wei, C. A. Yuan, P. Sarro, and G. Zhang, "Miniaturized particulate matter sensor for portable air quality monitoring devices", in *IEEE SENSORS 2014 Proceedings*, IEEE, 2014. DOI: 10.1109/icsens.2014.6985464.

[26] W. c. Hao, Z. Nie, J. l. Liu, M. h. Liu, and S. t. He, "Advances in a developed surface acoustic wave based particulate matter 2.5 monitor", in *2016 Symposium on Piezoelectricity, Acoustic Waves, and Device Applications (SPAWDA)*, 2016, pp. 227–229.

[27] J. Zhao, M. Liu, L. Liang, W. Wang, and J. Xie, "Airborne particulate matter classification and concentration detection based on 3d printed virtual impactor and quartz crystal microbalance sensor", *Sensors and Actuators A: Physical*, vol. 238, pp. 379 –388, 2016.

[28] *PPD42NS Dust Sensor Datasheet*. [Online]. Available: http://www.mouser.com/ds/2/744/Seeed_101020012-838657.pdf.

[29] *E2V MiCS-5121 CO/VOCs gas sensor Datasheet*. [Online]. Available: http://www.e2v.com/shared/content/resources/File/sensors_datasheets/Metal_Oxide/mics-5121.pdf.

[30] Y. Wang, J. Li, H. Jing, Q. Zhang, J. Jiang, and P. Biswas, "Laboratory evaluation and calibration of three low-cost particle sensors for particulate matter measurement", *Aerosol Science and Technology*, vol. 49, no. 11, pp. 1063–1077, 2015.

[31] M. Rossi and D. Brunelli, "Autonomous gas detection and mapping with unmanned aerial vehicles", *IEEE Transactions on Instrumentation and Measurement*, vol. 65, no. 4, pp. 765–775, 2016, ISSN: 0018-9456. DOI: 10.1109/TIM.2015.2506319.

[32] M. Rossi and P. Tosato, "Energy neutral design of an IoT system for pollution monitoring", in *2017 IEEE Workshop on Environmental, Energy, and Structural Monitoring Systems (EESMS)*, cited By 3, IEEE, 2017, ISBN: 9781538628164. DOI: 10.1109/EESMS.2017.8052691.

[33] R. Piyare, A. L. Murphy, C. Kiraly, P. Tosato, and D. Brunelli, "Ultra low power wake-up radios: A hardware and networking survey", *IEEE Communications Surveys Tutorials*, vol. 19, no. 4, pp. 2117–2157, 2017, ISSN: 1553-877X. DOI: 10.1109/COMST.2017.2728092.

[34] M. Magno, V. Jelicic, B. Srbinovski, V. Bilas, E. Popovici, and L. Benini, "Design, Implementation, and Performance Evaluation of a Flexible Low-Latency Nanowatt Wake-Up Radio Receiver", *IEEE Transactions on Industrial Informatics*, vol. 12, no. 2, pp. 633–644, 2016, ISSN: 1551-3203. DOI: 10.1109/TII.2016.2524982.

[35] P. Le-Huy and S. Roy, "Low-Power Wake-Up Radio for Wireless Sensor Networks", *Mobile Networks and Applications*, vol. 15, no. 2, pp. 226–236, 2010.

[36] N. E. Roberts and D. D. Wentzloff, "A 98 nW Wake-up Radio for Wireless Body Area Networks", in *Radio Frequency Integrated Circuits Symposium (RFIC), IEEE*, 2012, pp. 373–376. DOI: 10.1109/RFIC.2012.6242302.

[37] *Tmote Sky: Ultra low power IEEE 802.15. 4 compliant wireless sensor module*, Moteiv Corporation, San Francisco, USA.

[38] R. Piyare, A. L. Murphy, P. Tosato, and D. Brunelli, "Plug into a plant: Using a plant microbial fuel cell and a wake-up radio for an energy neutral sensing system", in *2017 IEEE 42nd Conference on Local Computer Networks Workshops (LCN Workshops)*, IEEE, 2017. DOI: 10.1109/lcn.workshops.2017.60.

[39] F. Khaled, O. Ondel, and B. Allard, "Microbial fuel cells as power supply of a low-power temperature sensor", *Journal of Power Sources*, vol. 306, pp. 354–360, 2016.

[40] Y. R. Thomas, M. Picot, A. Carer, O. Berder, O. Sentieys, and F. Barriere, "A single sediment-microbial fuel cell powering a wireless telecommunication system", *Journal of Power Sources*, vol. 241, pp. 703–708, 2013.

[41] C. Donovan, A. Dewan, H. Peng, D. Heo, and H. Beyenal, "Power management system for a 2.5W remote sensor powered by a sediment microbial fuel cell", *Journal of Power Sources*, vol. 196, no. 3, pp. 1171–1177, 2011.

[42] D. Brunelli, P. Tosato, and M. Rossi, "Flora Health Wireless Monitoring with Plant-Microbial Fuel Cel", *Procedia Engineering*, vol. 168, pp. 1646–1650, 2016.

[43] D. Huan, W. Yi-Cheng, F. Zhang, Z.-C. Huang, C. Zheng, X. Hui-Juan, and Z. Feng, "Factors affecting the performance of single-chamber soil microbial fuel cells for power generation", *Pedosphere*, vol. 24, no. 3, pp. 330–338, 2014. DOI: 10.1016/S1002-0160(14)60019-9.

[44] M. Rossi, A. Iannaci, P. Tosato, and D. Brunelli, "Let the microbes power your sensing display", in *2017 IEEE SENSORS*, 2017, pp. 1–3. DOI: 10.1109/ICSENS.2017.8234406.

[45] A. Dewan, H. Beyenal, and Z. Lewandowski, "Intermittent energy harvesting improves the performance of microbial fuel cells", *Environmental science & technology*, vol. 43, no. 12, pp. 4600–4605, 2009.

[46] T. Polonelli, T. Le Huy, L. Lizzi, F. Ferrero, and M. Magno, "A wake-up receiver with ad-hoc antenna co-design for wearable applications", in *Sensors Applications Symposium (SAS), IEEE*, IEEE, 2016, pp. 1–6.

[47] D. Brunelli, M. Rossi, and P. Tosato, "A radio-triggered wireless sensor platform powered by soil bacteria", *Proceedings*, vol. 1, no. 4, p. 568, 2017. DOI: 10.3390/proceedings1040568.

[48] M. Castro, A. J. Jara, and A. F. G. Skarmeta, "Smart lighting solutions for smart cities", in *Proceedings of the 2013 27th International Conference on Advanced Information Networking and Applications Workshops*, ser. WAINA '13, Washington, DC, USA: IEEE Computer Society, 2013, pp. 1374–1379, ISBN: 978-0-7695-4952-1. DOI: 10.1109/WAINA.2013.254.

[49] *International Energy Agency - Tracking Clean Energy Progress - Lighting*. [Online]. Available: https://www.iea.org/tcep/buildings/lighting/.

[50] Y. M. Yusoff, R. Rosli, M. U. Karnaluddin, and M. Samad, "Towards smart street lighting system in malaysia", in *2013 IEEE Symposium on Wireless Technology Applications (ISWTA)*, 2013, pp. 301–305. DOI: 10.1109/ISWTA.2013.6688792.

[51] J. Higuera, W. Hertog, M. Perálvarez, J. Polo, and J. Carreras, "Smart lighting system iso/iec/ieee 21451 compatible", *IEEE Sensors Journal*, vol. 15, no. 5, pp. 2595–2602, 2015, ISSN: 1530-437X. DOI: 10.1109/JSEN.2015.2390262.

[52] L. Martirano, "A smart lighting control to save energy", in *Proceedings of the 6th IEEE International Conference on Intelligent Data Acquisition and Advanced Computing Systems*, vol. 1, 2011, pp. 132–138. DOI: 10.1109/IDAACS.2011.6072726.

[53] P. Kiedrowski, "Toward more efficient and more secure last mile smart metering and smart lighting communication systems with the use of PLC/RF hybrid technology", *International Journal of Distributed Sensor Networks*, vol. 2015, pp. 1–9, 2015. DOI: 10.1155/2015/675926.

[54] *CENELEC EN 50065-1, signalling on low-voltage electrical installations in the frequency range 3 khz to 148.5 khz*, 2008. [Online]. Available: http://www.cenelec.eu.

[55] A. A. Amarsingh, H. a. Latchman, and D. Yang, "Narrowband power line communications: Enabling the smart grid", *IEEE Potentials*, vol. 33, no. 1, pp. 16–21, 2014, ISSN: 02786648. DOI: 10.1109/MPOT.2013.2249691.

[56] V. C. Gungor, D. Sahin, T. Kocak, S. Ergut, C. Buccella, C. Cecati, and G. P. Hancke, "Smart grid technologies: Communication technologies and standards", *IEEE Transactions on Industrial Informatics*, vol. 7, no. 4, pp. 529–539, 2011, ISSN: 1551-3203. DOI: 10.1109/TII.2011.2166794.

[57] S. Galli, A. Scaglione, and Z. Wang, "For the grid and through the grid: The role of power line communications in the smart grid", *Proceedings of the IEEE*, vol. 99, no. 6, pp. 998–1027, 2011, ISSN: 00189219. DOI: 10.1109/JPROC.2011.2109670. arXiv: 1010.1973.

[58] D. D. Giustina, P. Ferrari, A. Flammini, S. Rinaldi, and E. Sisinni, "Automation of distribution grids with iec 61850: A first approach using broadband power line communication", *IEEE Transactions on Instrumentation and Measurement*, vol. 62, no. 9, pp. 2372–2383, 2013, ISSN: 0018-9456. DOI: 10.1109/TIM.2013.2270922.

[59] G. Artale, A. Cataliotti, V. Cosentino, D. D. Cara, R. Fiorelli, S. Guaiana, N. Panzavecchia, and G. Tinè, "A new PLC-based smart metering architecture for medium/low voltage grids: Feasibility and experimental characterization", *Measurement*, vol. 129, pp. 479–488, 2018. DOI: 10.1016/j.measurement.2018.07.070.

[60] A. Zaballos, A. Vallejo, M. Majoral, and J. Selga, "Survey and performance comparison of AMR over PLC standards", *IEEE Transactions on Power Delivery*, vol. 24, no. 2, pp. 604–613, 2009. DOI: 10.1109/tpwrd.2008.2002845.

[61] B. Adebisi, A. Khalid, Y. Tsado, and B. Honary, "Narrowband PLC Channel Modelling For Smart Grid Applications", pp. 67–72, 2014.

[62] W. Zhu, X. Zhu, E. Lim, and Y. Huang, "State-of-art power line communications channel modelling", *Procedia Computer Science*, vol. 17, pp. 563–570, 2013, ISSN: 18770509. DOI: 10.1016/j.procs.2013.05.072.

[63] K. Razazian and J. Yazdani, "CENELEC and powerline communication specification in realization of smart grid technology", *IEEE PES Innovative Smart*

Grid Technologies Conference Europe, 2011, ISSN: 2165-4816. DOI: 10.1109/ISGTEurope.2011.6162685.

[64] I. H. Cavdar and E. Karadeniz, "Measurements of Impedance and Attenuation at CENELEC Bands for Power Line Communications Systems", *Sensors*, vol. 8, no. 12, pp. 8027–8036, 2008, ISSN: 1424-8220. DOI: 10.3390/s8128027.

[65] *ITU-T G.9904 : Narrowband orthogonal frequency division multiplexing power line communication transceivers for PRIME networks*. [Online]. Available: https://www.itu.int/rec/T-REC-G.9904/en.

[66] *ITU-T G.9903 : Narrowband orthogonal frequency division multiplexing power line communication transceivers for G3-PLC networks*. [Online]. Available: https://www.itu.int/rec/T-REC-G.9903-201708-I/en.

[67] P. Mlynek, M. Koutny, J. Misurec, and Z. Kolka, "Measurements and evaluation of PLC modem with G3 and PRIME standards for Street Lighting Control", *IEEE ISPLC 2014 - 18th IEEE International Symposium on Power Line Communications and Its Applications*, pp. 238–243, 2014. DOI: 10.1109/ISPLC.2014.6812318.

[68] L. Müller and J. W. Kimball, "Dual-input high gain dc-dc converter based on the cockcroft-walton multiplier", in *2014 IEEE Energy Conversion Congress and Exposition (ECCE)*, 2014, pp. 5360–5367. DOI: 10.1109/ECCE.2014.6954136.

[69] I. C. Kobougias and E. C. Tatakis, "Optimal design of a half-wave Cockcroft-Walton voltage multiplier with minimum total capacitance", *IEEE Transactions on Power Electronics*, vol. 25, no. 9, pp. 2460–2468, 2010, ISSN: 08858993. DOI: 10.1109/TPEL.2010.2049380.

[70] M. C. Riccardo Fiorelli, *ST7580 power line communication system-on-chip design guide*. [Online]. Available: http://www.st.com/st-web-ui/static/active/en/resource/technical/document/application{_}note/DM00050178.pdf.

[71] A. Sittoni, D. Brunelli, D. Macii, P. Tosato, and D. Petri, "Street lighting in smart cities: A simulation tool for the design of systems based on narrowband PLC", in *2015 IEEE First International Smart Cities Conference (ISC2)*, IEEE, 2015. DOI: 10.1109/isc2.2015.7366195.

[72] S. M. Amin and B. Wollenberg, "Toward a smart grid: Power delivery for the 21st century", *IEEE Power and Energy Magazine*, vol. 3, no. 5, pp. 34–41, 2005. DOI: 10.1109/mpae.2005.1507024.

[73] *EPRI electric power research institute*. [Online]. Available: http://smartgrid.epri.com/.

[74] W. Sattinger and G. Giannuzzi, "Monitoring continental europe: An overview of WAM systems used in italy and switzerland", *IEEE Power and Energy Magazine*, vol. 13, no. 5, pp. 41–48, 2015.

[75] *NIST framework and roadmap for smart grid interoperability standards*. [Online]. Available: https://www.nist.gov/sites/default/files/documents/2018/06/06/webinar_slides.pdf.

[76] L. Peretto, "The role of measurements in the smart grid era", *IEEE Instrumentation Measurement Magazine*, vol. 13, no. 3, pp. 22–25, 2010.

[77] F. Ponci, S. Sulis, M. Pau, A. Angioni, and P. Pegoraro, "Chapter 7 - state estimation and pmus", in *Phasor Measurement Units and Wide Area Monitoring Systems*, A. Monti, C. Muscas, and F. Ponci, Eds., Academic Press, 2016, pp. 123 –176, ISBN: 978-0-12-804569-5. DOI: https://doi.org/10.1016/B978-0-12-804569-5.00007-0.

[78] A. Abur and A. G. Expósito, *Power System State Estimation: Theory and Implementation (Power Engineering (Willis))*. CRC Press, 2004, ISBN: 9780824755706.

[79] L. Hu, Z. Wang, X. Liu, A. V. Vasilakos, and F. E. Alsaadi, "Recent advances on state estimation for power grids with unconventional measurements", *IET Control Theory & Applications*, vol. 11, no. 18, pp. 3221–3232, 2017. DOI: 10.1049/iet-cta.2017.0629.

[80] K. Dehghanpour, Z. Wang, J. Wang, Y. Yuan, and F. Bu, "A survey on state estimation techniques and challenges in smart distribution systems", Aug. 31, 2018. DOI: 10.1109/TSG.2018.2870600. arXiv: http://arxiv.org/abs/1809.00057v2 [cs.SY].

[81] M. Haghifam, M. Haghifam, and B. S. Chabok, "State estimation in electric distribution networks in presence of distributed generation using the pmus", in *CIRED 2012 Workshop: Integration of Renewables into the Distribution Grid*, 2012, pp. 1–4. DOI: 10.1049/cp.2012.0754.

[82] P. A. Pegoraro, J. Tang, J. Liu, F. Ponci, A. Monti, and C. Muscas, "Pmu and smart metering deployment for state estimation in active distribution grids", in *2012 IEEE International Energy Conference and Exhibition (ENERGYCON)*, 2012, pp. 873–878. DOI: 10.1109/EnergyCon.2012.6348274.

[83] J. Liu, J. Tang, F. Ponci, A. Monti, C. Muscas, and P. A. Pegoraro, "Trade-offs in PMU deployment for state estimation in active distribution grids", *IEEE Transactions on Smart Grid*, vol. 3, no. 2, pp. 915–924, 2012.

[84] M. H. F. Wen, J. Xu, and V. O. K. Li, "Optimal multistage PMU placement for wide-area monitoring", *IEEE Transactions on Power Systems*, vol. 28, no. 4, pp. 4134–4143, 2013.

[85] K. G. Khajeh, E. Bashar, A. M. Rad, and G. B. Gharehpetian, "Integrated model considering effects of zero injection buses and conventional measurements on optimal PMU placement", *IEEE Transactions on Smart Grid*, vol. 8, no. 2, pp. 1006–1013, 2017.

[86] D. Carta, A. Benigni, and C. Muscas, "Model order reduction for PMU-based state estimation in distribution grids", *IEEE Systems Journal*, vol. 12, no. 3, pp. 2711–2720, 2018. DOI: 10.1109/jsyst.2017.2697309.

[87] G. Barchi, D. Fontanelli, D. Macii, and D. Petri, "On the Accuracy of Phasor Angle Measurements in Power Networks", *IEEE Transactions on Instrumentation and Measurement*, vol. 64, no. 5, pp. 1129–1139, 2015, ISSN: 0018-9456. DOI: 10.1109/TIM.2014.2363752.

[88] P. Romano and M. Paolone, "Enhanced interpolated-DFT for synchrophasor estimation in FPGAs: Theory, implementation, and validation of a PMU prototype", *IEEE Transactions on Instrumentation and Measurement*, vol. 63, no. 12, pp. 2824–2836, 2014. DOI: 10.1109/tim.2014.2321463.

[89] P. A. Pegoraro, A. Meloni, L. Atzori, P. Castello, and S. Sulis, "PMU-Based Distribution System State Estimation with Adaptive Accuracy Exploiting

Local Decision Metrics and IoT Paradigm", *IEEE Transactions on Instrumentation and Measurement*, vol. 66, no. 4, pp. 704–714, 2017, ISSN: 0018-9456. DOI: 10.1109/TIM.2017.2657938.

[90] M. Paolone, A. Borghetti, and C. A. Nucci, "A synchrophasor estimation algorithm for the monitoring of active distribution networks in steady state and transient conditions", *Proceedings of the 17th Power Systems Computation Conference (PSCC 2011)*, pp. 1–8, 2011.

[91] A. von Meier, E. Stewart, A. McEachern, M. Andersen, and L. Mehrmanesh, "Precision micro-synchrophasors for distribution systems: A summary of applications", *IEEE Transactions on Smart Grid*, vol. 8, no. 6, pp. 2926–2936, 2017, ISSN: 1949-3053. DOI: 10.1109/TSG.2017.2720543.

[92] X. Chen, K. J. Tseng, and G. Amaratunga, "State estimation for distribution systems using micro-synchrophasors", in *2015 IEEE PES Asia-Pacific Power and Energy Engineering Conference (APPEEC)*, 2015, pp. 1–5. DOI: 10.1109/APPEEC.2015.7381051.

[93] A. L. Liao, E. M. Stewart, and E. C. Kara, "Micro-synchrophasor data for diagnosis of transmission and distribution level events", in *2016 IEEE/PES Transmission and Distribution Conference and Exposition (T D)*, 2016, pp. 1–5. DOI: 10.1109/TDC.2016.7519975.

[94] A. G. Phadke, J. S. Thorp, and K. J. Karimi, "State estimation with phasor measurements", *IEEE Transactions on Power Systems*, vol. 1, no. 1, pp. 233–238, 1986.

[95] D. Macii, D. Fontanelli, and D. Petri, "Performance of phasor measurement units for power quality event detection in urban distribution grids", in *2016 IEEE International Smart Cities Conference (ISC2)*, 2016, pp. 1–7. DOI: 10.1109/ISC2.2016.7580845.

[96] A. Dumitrescu, R. Roman, and M. Albu, "Synchronized measurements and power quality assesment", in *2015 IEEE Eindhoven PowerTech*, 2015, pp. 1–6. DOI: 10.1109/PTC.2015.7232815.

[97] A. Moschitta, P. Carbone, and C. Muscas, "Performance comparison of advanced techniques for voltage dip detection", *IEEE Transactions on Instrumentation and Measurement*, vol. 61, no. 5, pp. 1494–1502, 2012.

[98] A. Borghetti, C. A. Nucci, M. Paolone, G. Ciappi, and A. Solari, "Synchronized phasors monitoring during the islanding maneuver of an active distribution network", *IEEE Transactions on Smart Grid*, vol. 2, no. 1, pp. 82–91, 2011, ISSN: 1949-3053. DOI: 10.1109/TSG.2010.2094213.

[99] D. M. Laverty, R. J. Best, and D. J. Morrow, "Loss-of-mains protection system by application of phasor measurement unit technology with experimentally assessed threshold settings", *IET Generation, Transmission Distribution*, vol. 9, no. 2, pp. 146–153, 2015, ISSN: 1751-8687. DOI: 10.1049/iet-gtd.2014.0106.

[100] P. Wall, P. Dattaray, Z. Jin, P. Mohapatra, J. Yu, D. Wilson, K. Hay, S. Clark, M. Osborne, P. M. Ashton, and V. Terzija, "Deployment and demonstration of wide area monitoring system in power system of great britain", *Journal of Modern Power Systems and Clean Energy*, vol. 4, no. 3, pp. 506–518, 2016. DOI: 10.1007/s40565-016-0218-3.

[101] US Department of Energy and Office of Electricity Delivery and Energy Reliability, "Factors Affecting PMU Installation Costs", Tech. Rep., 2014. [Online]. Available: https://www.smartgrid.gov/files/PMU-cost-study-final-10162014.pdf.

[102] *PMU cost and benefit study*. [Online]. Available: http://caper-usa.com/wp-content/uploads/2017/08/Session-IV-PMU-Cost-Benefits-Studies-DLelic_8-8-17.pdf.

[103] *IEEE standard for synchrophasor measurements for power systems*, 2011. DOI: 10.1109/ieeestd.2011.6111219.

[104] *IEEE standard for synchrophasor data transfer for power systems*, Dec. 2011. DOI: 10.1109/IEEESTD.2011.6111222.

[105] *IEEE standard for synchrophasor measurements for power systems – amendment 1: Modification of selected performance requirements*, Apr. 2014. DOI: 10.1109/IEEESTD.2014.6804630.

[106] K. E. Martin, "Synchrophasor measurements under the ieee standard c37.118.1-2011 with amendment c37.118.1a", *IEEE Transactions on Power Delivery*, vol. 30, no. 3, pp. 1514–1522, 2015, ISSN: 0885-8977. DOI: 10.1109/TPWRD.2015.2403591.

[107] *IEEE/IEC draft international standard - measuring relays and protection equipment - part 118-1: Synchrophasor for power system - measurements*, Jan. 2018.

[108] A. Monti, A. Roscoe, and A. Sadu, "Chapter 6 - international standards for pmu and tests for compliance", in *Phasor Measurement Units and Wide Area Monitoring Systems*, A. Monti, C. Muscas, and F. Ponci, Eds., Academic Press, 2016, pp. 87 –121, ISBN: 978-0-12-804569-5. DOI: https://doi.org/10.1016/B978-0-12-804569-5.00006-9.

[109] *Voltage Characteristics of Electricity Supplied by Public Electricity Networks*, 2010.

[110] *IEEE guide for synchronization, calibration, testing, and installation of phasor measurement units (pmus) for power system protection and control*, 2013. DOI: 10.1109/IEEESTD.2013.6475134.

[111] A. Goldstein, *Lessons learned from the NIST assessment of PMUs*, 2014.

[112] J. Braun, C. Mester, and M. André, "Requirements for an advanced pmu calibrator", in *2016 Conference on Precision Electromagnetic Measurements (CPEM 2016)*, 2016, pp. 1–2. DOI: 10.1109/CPEM.2016.7540656.

[113] G. Frigo, D. Colangelo, A. Derviškadić, M. Pignati, C. Narduzzi, and M. Paolone, "Definition of accurate reference synchrophasors for static and dynamic characterization of pmus", *IEEE Transactions on Instrumentation and Measurement*, vol. 66, no. 9, pp. 2233–2246, 2017, ISSN: 0018-9456. DOI: 10.1109/TIM.2017.2698709.

[114] C. Qian and M. Kezunovic, "Synchrophasor reference algorithm for pmu calibration system", in *2016 IEEE/PES Transmission and Distribution Conference and Exposition (T D)*, 2016, pp. 1–5. DOI: 10.1109/TDC.2016.7520024.

[115] R. M. Moraes, Y. Hu, G. Stenbakken, K. Martin, J. E. R. Alves, A. G. Phadke, H. A. R. Volskis, and V. Centeno, "Pmu interoperability, steady-state and dynamic performance tests", *IEEE Transactions on Smart Grid*, vol. 3, no. 4, pp. 1660–1669, 2012, ISSN: 1949-3053. DOI: 10.1109/TSG.2012.2208482.

[116] F. L. Grando, G. W. Denardin, and M. Moreto, "Test platform for analysis and development of phasor measurement units (pmu)", in *2016 12th IEEE International Conference on Industry Applications (INDUSCON)*, 2016, pp. 1–6. DOI: 10.1109/INDUSCON.2016.7874571.

[117] P. Castello, C. Muscas, P. A. Pegoraro, S. Sulis, and S. Toscani, "Experimental characterization of dynamic methods for synchrophasor measurements", in *2014 IEEE International Workshop on Applied Measurements for Power Systems Proceedings (AMPS)*, 2014, pp. 1–6. DOI: 10.1109/AMPS.2014.6947709.

[118] R. Meyur, G. N. Stenbakken, and V. Centeno, "A labview based test system to characterize phasor measurement units", in *2017 North American Power Symposium (NAPS)*, 2017, pp. 1–6. DOI: 10.1109/NAPS.2017.8107185.

[119] D. Georgakopoulos and S. Quigg, "Precision measurement system for the calibration of phasor measurement units", *IEEE Transactions on Instrumentation and Measurement*, vol. 66, no. 6, pp. 1441–1445, 2017, ISSN: 0018-9456. DOI: 10.1109/TIM.2017.2653518.

[120] D. Colangelo, L. Zanni, M. Pignati, P. Romano, M. Paolone, J. Braun, and L. Bernier, "Architecture and characterization of a calibrator for pmus operating in power distribution systems", in *2015 IEEE Eindhoven PowerTech*, 2015, pp. 1–6. DOI: 10.1109/PTC.2015.7232792.

[121] Y. Tang, G. N. Stenbakken, and A. Goldstein, "Calibration of phasor measurement unit at nist", *IEEE Transactions on Instrumentation and Measurement*, vol. 62, no. 6, pp. 1417–1422, 2013, ISSN: 0018-9456. DOI: 10.1109/TIM.2013.2240951.

[122] J. Braun and C. Mester, "Reference grade calibrator for the testing of the dynamic behavior of phasor measurement units", in *2012 Conference on Precision electromagnetic Measurements*, 2012, pp. 410–411. DOI: 10.1109/CPEM.2012.6250977.

[123] V. Krishna, K. Dekhane, and G. Sanchez, *The Virginia Tech PMU and PDC Test System*. [Online]. Available: https://www.naspi.org/sites/default/files/2016-09/vt_krishna_pmu_pdc_test_system_20120229.pdf.

[124] M. Luiso, D. Macii, P. Tosato, D. Brunelli, D. Gallo, and C. Landi, "A Low-Voltage Measurement Testbed for Metrological Characterization of Algorithms for Phasor Measurement Units", *IEEE Transactions on Instrumentation and Measurement*, pp. 1–14, 2018, ISSN: 0018-9456. DOI: 10.1109/TIM.2018.2852940.

[125] *Ieee standard for a precision clock synchronization protocol for networked measurement and control systems - redline*, 2008.

[126] T. C. Telecommunications and T. group, *Irig serial time code formats*, 1998.

[127] *Ieee standard profile for use of ieee 1588 precision time protocol in power system applications*, 2017. DOI: 10.1109/IEEESTD.2017.7953616.

[128] *Uncertainty of measurement – Part 3: Guide to the expression of uncertainty in measurement (GUM)*, 2008.

[129] *IEEE Approved Draft Standard for Digitizing Waveform Recorders*, 2017.

[130] E. Nunzi, P. Carbone, and D. Petri, "A procedure for highly reproducible measurements of adc spectral parameters", *IEEE Transactions on Instrumentation and Measurement*, vol. 52, no. 4, pp. 1279–1283, 2003, ISSN: 0018-9456. DOI: 10.1109/TIM.2003.816817.

[131] G. Crotti, D. Gallo, D. Giordano, C. Landi, and M. Luiso, "Non-conventional instrument current transformer test set for industrial applications", in *2014 IEEE International Workshop on Applied Measurements for Power Systems Proceedings (AMPS)*, 2014, pp. 1–5. DOI: 10.1109/AMPS.2014.6947699.

[132] ——, "Industrial comparator for smart grid sensor calibration", *IEEE Sensors Journal*, vol. 17, no. 23, pp. 7784–7793, 2017, ISSN: 1530-437X. DOI: 10.1109/JSEN.2017.2724299.

[133] E. Rubiola, *Phase Noise and Frequency Stability in Oscillators*. Cambridge University Press, 2008. DOI: 10.1017/cbo9780511812798.

[134] D. Petri, D. Fontanelli, and D. Macii, "A Frequency-Domain Algorithm for Dynamic Synchrophasor and Frequency Estimation", *IEEE Transactions on Instrumentation and Measurement*, vol. 63, no. 10, pp. 2330–2340, 2014, ISSN: 0018-9456. DOI: 10.1109/TIM.2014.2308996.

[135] D. Belega and D. Petri, "Accuracy Analysis of the Multicycle Synchrophasor Estimator Provided by the Interpolated DFT Algorithm", *IEEE Transactions on Instrumentation and Measurement*, vol. 62, no. 5, pp. 942–953, 2013, ISSN: 0018-9456. DOI: 10.1109/TIM.2012.2236777.

[136] J. A. de la O Serna and M. A. Platas-Garza, "Maximally flat differentiators through WLS Taylor decomposition", *Digital Signal Processing*, vol. 21, no. 2, pp. 183 –194, 2011, ISSN: 1051-2004. DOI: 10.1016/j.dsp.2010.06.007.

[137] D. Macii, D. Petri, and A. Zorat, "Accuracy analysis and enhancement of DFT-based synchrophasor estimators in off-nominal conditions", *IEEE Transactions on Instrumentation and Measurement*, vol. 61, no. 10, pp. 2653–2664, Oct. 2012, ISSN: 0018-9456. DOI: 10.1109/TIM.2012.2199197.

[138] D. Macii, G. Barchi, and D. Petri, "Design criteria of digital filters for synchrophasor estimation", in *Proc. IEEE International Instrumentation and Measurement Technology Conference (I2MTC)*, Minneapolis, MN, USA, 2013, pp. 1579–1584.

[139] A. Roscoe, I. Abdulhadi, and G. Burt, "P and M class phasor measurement unit algorithms using adaptive cascaded filters", *IEEE Transactions on Power Delivery*, vol. 28, no. 3, pp. 1447–1459, 2013.

[140] A. J. Roscoe, B. Dickerson, and K. E. Martin, "Filter design masks for C37.118.1a-compliant frequency-tracking and fixed-filter M-Class phasor measurement units", *IEEE Transactions on Instrumentation and Measurement*, vol. 64, no. 8, pp. 2096–2107, 2015.

[141] M. A. P. a. J. Platas-Garza and J. A. de la O Serna, "Dynamic phasor and frequency estimates through maximally flat differentiators", *IEEE Transactions on Instrumentation and Measurement*, vol. 59, no. 7, pp. 1803–1811, 2010, ISSN: 0018-9456. DOI: 10.1109/TIM.2009.2030921.

[142] P. Castello, J. Liu, C. Muscas, P. A. Pegoraro, F. Ponci, and A. Monti, "A fast and accurate pmu algorithm for p+m class measurement of synchrophasor and frequency", *IEEE Transactions on Instrumentation and Measurement*,

vol. 63, no. 12, pp. 2837–2845, 2014, ISSN: 0018-9456. DOI: 10.1109/TIM.2014.2323137.

[143] W. Premerlani, B. Kasztenny, and M. Adamiak, "Development and implementation of a synchrophasor estimator capable of measurements under dynamic conditions", *IEEE Transactions on Power Delivery*, vol. 23, no. 1, pp. 109–123, 2008, ISSN: 0885-8977. DOI: 10.1109/TPWRD.2007.910982.

[144] M. A. Platas-Garza and J. A. de la O Serna, "Dynamic Harmonic Analysis Through Taylor–Fourier Transform", *IEEE Transactions on Instrumentation and Measurement*, vol. 60, no. 3, pp. 804–813, 2011, ISSN: 0018-9456. DOI: 10.1109/TIM.2010.2064690.

[145] M. D. Kušljevìc and J. J. Tomìc, "Multiple-resonator-based power system Taylor-Fourier harmonic analysis", *IEEE Transactions on Instrumentation and Measurement*, vol. 64, no. 2, pp. 554–563, 2015, ISSN: 0018-9456. DOI: 10.1109/TIM.2014.2345591.

[146] M. Bertocco, G. Frigo, G. Giorgi, and C. Narduzzi, "Frequency tracking for efficient phasor measurement based on a CSTFM model", in *Proc. IEEE International Workshop on Applied Measurements for Power Systems (AMPS)*, Aachen, Germany, 2015, pp. 84–89.

[147] M. Bertocco, G. Frigo, C. Narduzzi, and F. Tramarin, "Resolution enhancement by compressive sensing in power quality and phasor measurement", *IEEE Transactions on Instrumentation and Measurement*, vol. 63, no. 10, pp. 2358–2367, 2014. DOI: 10.1109/tim.2014.2321465.

[148] G. Andria, M. Savino, and A. Trotta, "Windows and interpolation algorithms to improve electrical measurement accuracy", *IEEE Transactions on Instrumentation and Measurement*, vol. 38, no. 4, pp. 856–863, 1989, ISSN: 0018-9456. DOI: 10.1109/19.31004.

[149] A. Derviškadić, P. Romano, and M. Paolone, "Iterative-interpolated dft for synchrophasor estimation: A single algorithm for p- and m-class compliant pmus", *IEEE Transactions on Instrumentation and Measurement*, vol. 67, no. 3, pp. 547–558, 2018, ISSN: 0018-9456. DOI: 10.1109/TIM.2017.2779378.

[150] R. Ferrero, P. A. Pegoraro, and S. Toscani, "Dynamic Fundamental and Harmonic Synchrophasor Estimation by Extended Kalman Filter", in *Proc. IEEE International Workshop on Applied Measurements for Power Systems (AMPS)*, Aachen, Germany, 2016, pp. 1–6.

[151] J. Liu, F. Ni, J. Tang, F. Ponci, and A. Monti, "A Modified Taylor-Kalman Filter for Instantaneous Dynamic Phasor Estimation", in *2012 3rd IEEE PES Innovative Smart Grid Technologies Europe (ISGT Europe)*, Berlin, Germany, 2012, pp. 1–7.

[152] J. A. de la O Serna and J. Rodriguez-Maldonado, "Instantaneous oscillating phasor estimates with Taylor^K-Kalman filters", *IEEE Transactions on Power Systems*, vol. 26, no. 4, pp. 2336–2344, 2011.

[153] J. Ren and M. Kezunovic, "Real-time power system frequency and phasors estimation using recursive wavelet transform", *IEEE Transactions on Power Delivery*, vol. 26, no. 3, pp. 1392–1402, 2011, ISSN: 0885-8977. DOI: 10.1109/TPWRD.2011.2135385.

[154] D. Belega and D. Petri, "Accuracy of synchrophasor measurements provided by the sine-fit algorithms", in *2012 IEEE International Energy Conference and Exhibition (ENERGYCON)*, 2012, pp. 921–926. DOI: 10.1109/EnergyCon.2012.6348283.

[155] R. V. Rocha, D. V. Coury, and R. M. Monaro, "Recursive and non-recursive algorithms for power system real time phasor estimations", *Electric Power Systems Research*, vol. 143, pp. 802 –812, 2017, ISSN: 0378-7796. DOI: https://doi.org/10.1016/j.epsr.2016.08.034.

[156] D. Macii, D. Petri, and A. Zorat, "Accuracy of dft-based synchrophasor estimators at off-nominal frequencies", in *2011 IEEE International Workshop on Applied Measurements for Power Systems (AMPS)*, 2011, pp. 19–24. DOI: 10.1109/AMPS.2011.6090349.

[157] C. Offelli and D. Petri, "Interpolation techniques for real-time multifrequency waveform analysis", *IEEE Transactions on Instrumentation and Measurement*, vol. 39, no. 1, pp. 106–111, 1990, ISSN: 0018-9456. DOI: 10.1109/19.50426.

[158] C. Liguori, A. Paolillo, and A. Pignotti, "An intelligent fft analyzer with harmonic interference effect correction and uncertainty evaluation", *IEEE Transactions on Instrumentation and Measurement*, vol. 53, no. 4, pp. 1125–1131, 2004, ISSN: 0018-9456. DOI: 10.1109/TIM.2004.831473.

[159] D. Belega and D. Dallet, "Multifrequency signal analysis by interpolated dft method with maximum sidelobe decay windows", *Measurement*, vol. 42, no. 3, pp. 420 –426, 2009, ISSN: 0263-2241. DOI: https://doi.org/10.1016/j.measurement.2008.08.006.

[160] D. Belega, D. Macii, and D. Petri, "Fast synchrophasor estimation by means of frequency-domain and time-domain algorithms", *IEEE Transactions on Instrumentation and Measurement*, vol. 63, no. 2, pp. 388–401, 2014, ISSN: 0018-9456. DOI: 10.1109/TIM.2013.2279000.

[161] J. A. de la O Serna, "Dynamic phasor estimates for power system oscillations", *IEEE Transactions on Instrumentation and Measurement*, vol. 56, no. 5, pp. 1648–1657, Oct. 2007, ISSN: 0018-9456. DOI: 10.1109/TIM.2007.904546.

[162] G. Barchi, D. Macii, and D. Petri, "Synchrophasor Estimators Accuracy: A Comparative Analysis", *IEEE Transactions on Instrumentation and Measurement*, vol. 62, no. 5, pp. 963–973, 2013, ISSN: 0018-9456. DOI: 10.1109/TIM.2012.2236776.

[163] P. Tosato, D. Macii, and D. Brunelli, "Implementation of phasor measurement units on low-cost embedded platforms: A feasibility study", in *2017 IEEE International Instrumentation and Measurement Technology Conference (I2MTC)*, 2017, pp. 1–6. DOI: 10.1109/I2MTC.2017.7969687.

[164] D. Belega and D. Petri, "A real-valued Taylor Weighted Least Squares synchrophasor estimator", in *2014 IEEE International Workshop on Applied Measurements for Power Systems Proceedings (AMPS)*, 2014, pp. 1–6. DOI: 10.1109/AMPS.2014.6947704.

[165] A. von Meier, D. Culler, A. McEachern, and R. Arghandeh, "Micro-synchrophasors for distribution systems", in *ISGT 2014*, 2014, pp. 1–5. DOI: 10.1109/ISGT.2014.6816509.

[166] B. Pinte, M. Quinlan, and K. Reinhard, "Low voltage micro-phasor measurement unit (μpmu)", in *2015 IEEE Power and Energy Conference at Illinois (PECI)*, 2015, pp. 1–4. DOI: 10.1109/PECI.2015.7064888.

[167] P. Romano, M. Paolone, T. Chau, B. Jeppesen, and E. Ahmed, "A high-performance, low-cost PMU prototype for distribution networks based on FPGA", in *2017 IEEE Manchester PowerTech*, IEEE, 2017. DOI: 10.1109/ptc.2017.7981025.

[168] J. A. Culliss, "A 3rd generation frequency disturbance recorder: A secure, low cost synchophasor measurement device.", PhD thesis, University of Tennessee, 2015.

[169] D. M. Laverty, R. J. Best, P. Brogan, I. A. Khatib, L. Vanfretti, and D. J. Morrow, "The OpenPMU platform for open-source phasor measurements", *IEEE Transactions on Instrumentation and Measurement*, vol. 62, no. 4, pp. 701–709, 2013. DOI: 10.1109/tim.2013.2240920.

[170] X. Zhao, D. M. Laverty, A. McKernan, D. J. Morrow, K. McLaughlin, and S. Sezer, "GPS-disciplined analog-to-digital converter for phasor measurement applications", *IEEE Transactions on Instrumentation and Measurement*, vol. 66, no. 9, pp. 2349–2357, Sep. 2017, ISSN: 0018-9456. DOI: 10.1109/TIM.2017.2700158.

[171] A. Angioni, G. Lipari, M. Pau, F. Ponci, and A. Monti, "A low cost PMU to monitor distribution grids", in *2017 IEEE International Workshop on Applied Measurements for Power Systems (AMPS)*, IEEE, 2017. DOI: 10.1109/amps.2017.8078337.

[172] A. Mingotti, L. Peretto, R. Tinarelli, A. Angioni, A. Monti, and F. Ponci, "Calibration of synchronized measurement system: From the instrument transformer to the PMU", in *2018 IEEE 9th International Workshop on Applied Measurements for Power Systems (AMPS)*, IEEE, 2018. DOI: 10.1109/amps.2018.8494887.

[173] A. Carta, N. Locci, C. Muscas, and S. Sulis, "A flexible GPS-based system for synchronized phasor measurement in electric distribution networks", *IEEE Transactions on Instrumentation and Measurement*, vol. 57, no. 11, pp. 2450–2456, 2008. DOI: 10.1109/tim.2008.924930.

[174] A. Carta, N. Locci, and C. Muscas, "A PMU for the measurement of synchronized harmonic phasors in three-phase distribution networks", *IEEE Transactions on Instrumentation and Measurement*, vol. 58, no. 10, pp. 3723–3730, 2009. DOI: 10.1109/tim.2009.2019319.

[175] P. Castello, P. Ferrari, A. Flammini, C. Muscas, and S. Rinaldi, "A new IED with PMU functionalities for electrical substations", *IEEE Transactions on Instrumentation and Measurement*, vol. 62, no. 12, pp. 3209–3217, 2013. DOI: 10.1109/tim.2013.2270921.

[176] P. Romano, M. Paolone, J. Arnold, and R. Piacentini, "An interpolated-DFT synchrophasor estimation algorithm and its implementation in an FPGA-based PMU prototype", in *2013 IEEE Power & Energy Society General Meeting*, IEEE, 2013. DOI: 10.1109/pesmg.2013.6672906.

[177] M. Pignati, M. Popovic, S. Barreto, R. Cherkaoui, G. D. Flores, J.-Y. L. Boudec, M. Mohiuddin, M. Paolone, P. Romano, S. Sarri, T. Tesfay, D.-C. Tomozei,

and L. Zanni, "Real-time state estimation of the EPFL-campus medium-voltage grid by using PMUs", in *2015 IEEE Power & Energy Society Innovative Smart Grid Technologies Conference (ISGT)*, IEEE, 2015. DOI: 10.1109/isgt.2015.7131877.

[178] P. A. Pegoraro, A. Meloni, L. Atzori, P. Castello, and S. Sulis, "Adaptive pmu-based distribution system state estimation exploiting the cloud-based iot paradigm", in *2016 IEEE International Instrumentation and Measurement Technology Conference Proceedings*, 2016, pp. 1–6. DOI: 10.1109/I2MTC.2016.7520461.

[179] S. Kon and T. Yamada, "Frequency characterizations of voltage and current transducers for evaluation of phasor measurement units", in *2013 IEEE 10th International Conference on Power Electronics and Drive Systems (PEDS)*, 2013, pp. 989–991. DOI: 10.1109/PEDS.2013.6527163.

[180] G. Crotti, D. Gallo, D. Giordano, C. Landi, and M. Luiso, "A characterized method for the real-time compensation of power system measurement transducers", *IEEE Transactions on Instrumentation and Measurement*, vol. 64, no. 6, pp. 1398–1404, 2015, ISSN: 0018-9456. DOI: 10.1109/TIM.2015.2398971.

[181] L. Peretto, R. Tinarelli, and K. Yiğit, "Uncertainty evaluation in measurement equipments for power systems", in *2016 IEEE International Workshop on Applied Measurements for Power Systems (AMPS)*, 2016, pp. 1–5. DOI: 10.1109/AMPS.2016.7602855.

[182] L. Peretto and R. Tinarelli, "Chapter 4 - sensors for pmus", in *Phasor Measurement Units and Wide Area Monitoring Systems*, A. Monti, C. Muscas, and F. Ponci, Eds., Academic Press, 2016, pp. 53 –62, ISBN: 978-0-12-804569-5. DOI: https://doi.org/10.1016/B978-0-12-804569-5.00004-5.

[183] A. Alanwar, F. M. Anwar, Y. F. Zhang, J. Pearson, J. Hespanha, and M. B. Srivastava, "Cyclops: PRU programming framework for precise timing applications", in *IEEE International Symposium on Precision Clock Synchronization for Measurement, Control, and Communication, ISPCS*, 2017, ISBN: 9781509057177. DOI: 10.1109/ISPCS.2017.8056744.

[184] P. Tosato, D. Macii, M. Luiso, D. Brunelli, D. Gallo, and C. Landi, "A Tuned Lightweight Estimation Algorithm for Low-Cost Phasor Measurement Units", *IEEE Transactions on Instrumentation and Measurement*, vol. 67, no. 5, pp. 1047–1057, 2018, ISSN: 0018-9456. DOI: 10.1109/TIM.2017.2775458.

[185] D. Macii, D. Fontanelli, G. Barchi, and D. Petri, "Impact of Acquisition Wideband Noise on Synchrophasor Measurements: A Design Perspective", *IEEE Transactions on Instrumentation and Measurement*, vol. 65, no. 10, pp. 2244–2253, 2016, ISSN: 0018-9456. DOI: 10.1109/TIM.2016.2594023.

[186] J. C. Eidson, "Case studies in instrumentation systems", in *Measurement, Control, and Communication Using IEEE 1588*, Springer, Jan. 1, 2006, ISBN: 978-1-84628-250-8. DOI: 10.1007/1-84628-251-9_8.

[187] ——, "An overview of clock synchronization using ieee 1588", in *Measurement, Control, and Communication Using IEEE 1588*, Springer, Jan. 1, 2006, ISBN: 978-1-84628-250-8. DOI: 10.1007/1-84628-251-9{_}3.

[188] R. Exel and F. Ring, "Improved clock synchronization accuracy through optimized servo parametrization", in *IEEE International Symposium on Precision*

Clock Synchronization for Measurement, Control, and Communication, ISPCS, 2013, pp. 65–70, ISBN: 9781479902415. DOI: 10.1109/ISPCS.2013.6644765.

[189] X. Chen, D. Li, S. Wang, H. Tang, and C. Liu, "Frequency-Tracking Clock Servo for Time Synchronization in Networked Motion Control Systems", *IEEE Access*, vol. 5, pp. 11 606–11 614, 2017, ISSN: 21693536. DOI: 10.1109/ACCESS.2017.2715878.

[190] *AD9548 datasheet*. [Online]. Available: https://www.analog.com/media/en/technical-documentation/data-sheets/ad9548.pdf.

[191] M. H. F. Wen, R. Arghandeh, A. von Meier, K. Poolla, and V. O. K. Li, "Phase identification in distribution networks with micro-synchrophasors", in *Proc. IEEE Power Energy Society General Meeting*, Denver, CO, USA, 2015, pp. 1–5.

[192] P. Tosato, D. Macii, D. Fontanelli, D. Brunelli, and D. Laverty, "A software-based low-jitter servo clock for inexpensive phasor measurement units", in *2018 IEEE International Symposium on Precision Clock Synchronization for Measurement, Control, and Communication (ISPCS)*, IEEE, 2018. DOI: 10.1109/ispcs.2018.8543082.

[193] J. Eidson, *Measurement, Control, and Communication Using IEEE 1588*. Springer-Verlag, 2006. DOI: 10.1007/1-84628-251-9.

[194] C. E. Calosso and E. Rubiola, "Phase noise and jitter in digital electronics", Dec. 31, 2016. arXiv: http://arxiv.org/abs/1701.00094v1.

[195] *Lantime m600/ptp: Ptpv2 / ieee 1588-2008 grandmaster clock and ntp time server with integrated gps or gps/glonass radio clock*. [Online]. Available: https://www.meinbergglobal.com/english/archive/lantime-m600-gps-ptpv2.htm.

[196] C. Offelli and D. Petri, "The influence of windowing on the accuracy of multifrequency signal parameter estimation", *IEEE Transactions on Instrumentation and Measurement*, vol. 41, no. 2, pp. 256–261, 1992, ISSN: 0018-9456. DOI: 10.1109/19.137357.

[197] F. J. Harris, "On the use of windows for harmonic analysis with the discrete fourier transform", *Proceedings of the IEEE*, vol. 66, no. 1, pp. 51–83, 1978, ISSN: 0018-9219. DOI: 10.1109/PROC.1978.10837.

[198] *IEEE Standard Definitions of Physical Quantities for Fundamental Frequency and Time Metrology–Random Instabilities*, 2009. DOI: 10.1109/IEEESTD.2009.6581834.

[199] D. W. Allan, "Statistics of atomic frequency standards", *Proceedings of the IEEE*, vol. 54, no. 2, pp. 221–230, 1966, ISSN: 0018-9219. DOI: 10.1109/PROC.1966.4634.

[200] D. W. Allan and J. A. Barnes, "A modified "allan variance" with increased oscillator characterization ability", in *Thirty Fifth Annual Frequency Control Symposium*, 1981, pp. 470–475. DOI: 10.1109/FREQ.1981.200514.

About the author

PIETRO TOSATO

ORCID: 0000-0003-1830-3088
Scopus: 57035328900

Journal papers

2017 1. ***Ultra low power wake-up radios: A hardware and networking survey***
R. Piyare, AL. Murphy, C. Kiraly, P. Tosato, D. Brunelli
IEEE Communications Surveys & Tutorials
DOI: 10.1109/COMST.2017.2728092

2018 2. ***A Tuned Lightweight Estimation Algorithm for Low-Cost Phasor Measurement Units***
P. Tosato, D. Macii, M. Luiso, D. Brunelli, D. Gallo, C. Landi
IEEE Transactions on Instrumentation and Measurement
DOI: 10.1109/TIM.2017.2775458

2018 3. ***A Low-Voltage Measurement Testbed for Metrological Characterization of Algorithms for Phasor Measurement Units***
M. Luiso, D. Macii, P. Tosato, D. Brunelli, D. Gallo, C. Landi
IEEE Transactions on Instrumentation and Measurement
DOI: 10.1109/TIM.2018.2852940

Articles presented at international conferences

4. ***Design and implementation of zero power wake-up for PLC modems in smart street lighting systems*** *2015*
   D. Brunelli, P. Tosato, R. Fiorelli
   Proceedings of IEEE International Conference on Emerging Technologies & Factory Automation
   DOI: 10.1109/ETFA.2015.7301444

5. ***Implementation of phasor measurement units on low-cost embedded platforms: A feasibility study*** *2017*
   P. Tosato, D. Macii, D. Brunelli
   Proceedings - 2017 IEEE International Instrumentation and Measurement Technology Conference
   DOI: 10.1109/I2MTC.2017.7969687

6. ***Energy Neutral Design of an IoT System for Pollution Monitoring*** *2017*
   M. Rossi, P. Tosato
   Proceedings of IEEE Workshop on Environmental, Energy, and Structural Monitoring Systems
   DOI: 10.1109/EESMS.2017.8052691

7. ***Zero-energy wake up for power line communications in smart cities*** *2016*
   P. Golchin, P. Tosato, D. Brunelli
   Proceedings of IEEE 2nd International Smart Cities Conference
   DOI: 10.1109/ISC2.2016.7580843

8. ***Let the microbes power your sensing display*** *2017*
   M. Rossi, A. Iannaci, P. Tosato, D. Brunelli
   Proceedings of IEEE Sensors 2017
   DOI: 10.1109/ICSENS.2017.8234406

9. ***A Thermoelectric Powered System for Skiing Performance Monitoring*** *2017*
   M. Nardello, P. Tosato, M. Rossi, D. Brunelli
   Lecture Notes in Electrical Engineering
   DOI: 10.1007/978-3-319-93082-4_18

10. ***An optimized wind energy harvester for remote pollution monitoring*** *2017*
    L. Pasquato, N. Bonotto, P. Tosato, D. Brunelli
    Proceedings of IEEE Workshop on Environmental, Energy, and Structural Monitoring Systems
    DOI: 10.1109/EESMS.2017.8052693

11. ***A Software-based Low-Jitter Servo Clock for Inexpensive Phasor Measurement Units*** *2018*
    P. Tosato, D. Macii, D. Fontanelli, D. Laverty, D. Brunelli
    Proceedings of IEEE International Symposium on Precision Clock Synchronization for Measurement, Control, and Communication
    DOI: 10.1109/ISPCS.2018.8543082

Other coauthored conference articles

2015 12. ***Street lighting in smart cities: A simulation tool for the design of systems based on narrowband PLC***
A. Sittoni, D. Brunelli, D. Macii, P. Tosato, D. Petri
Proceedings of IEEE 1st International Smart Cities Conference
DOI: 10.1109/ISC2.2015.7366195

2016 13. ***Flora health wireless monitoring with plant-microbial fuel cell***
D. Brunelli, P. Tosato, M. Rossi
Procedia Engineering
DOI: 10.1016/j.proeng.2016.11.481

2016 14. ***Microbial fuel cell as a biosensor and a power source for flora health monitoring***
D. Brunelli, P. Tosato, M. Rossi
Proceedings of IEEE Sensors
DOI: 10.1109/ICSENS.2016.7808831

2017 15. ***Long range wireless sensing powered by plant-microbial fuel cell***
M. Rossi, P. Tosato, L Gemma, L. Torquati, C. Catania, S. Camalò, D. Brunelli
Proceedings of Design, Automation & Test in Europe Conference & Exhibition
DOI: 10.23919/DATE.2017.7927258

2017 16. ***A testbed for the experimental characterization of estimation algorithms for phasor measurement units***
D. Gallo, C. Landi, M. Luiso, P. Tosato, D. Macii, D. Brunelli
Proceedings of IEEE International Workshop on Applied Measurements for Power Systems
DOI: 10.1109/AMPS.2017.8078341

2017 17. ***Plug into a Plant: Using a Plant Microbial Fuel Cell and a Wake-Up Radio for an Energy Neutral Sensing System***
R. Piyare, AL. Murphy, P. Tosato, D. Brunelli
Proceedings of IEEE Conference on Local Computer Networks Workshops, LCN Workshops
DOI: 10.1109/LCN.Workshops.2017.60

2016 18. ***Design optimization of zero power wake-up receiver in Power line communication***
P. Golchin, P. Tosato, D. Brunelli
Proceedings of International Symposium on Power Electronics, Electrical Drives, Automation and Motion
DOI: 10.1109/SPEEDAM.2016.7526028

2016 19. ***A radio-triggered wireless sensor platform powered by soil bacteria***
D. Brunelli, M. Rossi, P. Tosato
MDPI Proceedings of Eurosensors 2017
DOI: 10.3390/proceedings1040568

2017 20. ***Power Controlling, Monitoring and Routing Center Enabled by a DC-Transformer***
SAM Younus, M. Nardello, P. Tosato, D. Brunelli

MDPI Energies
DOI: 10.3390/en10030403

21. ***Wake up for Power Line Communication in Street Lighting Networks*** *2016*
P. Golchin, P. Tosato, D. Brunelli
Lecture Notes in Electrical Engineering
DOI: 10.1007/978-3-319-55071-8_12

22. ***Flora Monitoring with a Plant-Microbial Fuel Cell*** *2016*
D. Brunelli, P. Tosato, M. Rossi
Lecture Notes in Electrical Engineering
DOI: 10.1007/978-3-319-55071-8_6